# Study of Surface Plasmon Polariton Interaction with 2D Discontinuities: Reflection and Transmission

by

**Suat Barış İplikçioğlu**

A Dissertation Submitted to the
Graduate School of Sciences and Engineering
in Partial Fulfillment of the Requirements for
the Degree of

Master of Science

in

Electrical and Electronics Engineering

KOÇ ÜNİVERSİTESİ

February 18, 2022

**Study of Surface Plasmon Polariton Interaction with 2D Discontinuities: Reflection and Transmission**

Koç University

Graduate School of Sciences and Engineering

This is to certify that I have examined this copy of a master's thesis by

**Suat Barış İplikçioğlu**

and have found that it is complete and satisfactory in all respects,
and that any and all revisions required by the final
examining committee have been made.

Committee Members:

_____

Prof. M. İrşadi Aksun (Advisor)

_____

Assoc. Prof. Kaan Güven

_____

Assoc. Prof. Lale Alatan

Date: _____

# ABSTRACT

**Study of Surface Plasmon Polariton Interaction with 2D Discontinuities: Reflection and Transmission**
**Suat Barış İplikçioğlu**
**Master of Science in Electrical and Electronics Engineering**
**February 18, 2022**

Surface plasmon polaritons (SPPs) have been studied extensively in the past decades by virtue of their implications in nanotechnology, communications and life sciences. Their ability to localize light beyond the limit of diffraction has given rise to different types of nano-optical devices, such as plasmonic waveguides and nano-antennas. In the analysis and design of discontinuities that may inevitably persist on such structures, complex computational tools such as full-scale electromagnetic solvers are mostly used. In order to provide a simpler design route, approximate yet efficient models, akin to the ones developed for microwave circuits in the 20th century, are needed.

In this work, SPP behavior at canonical 2D discontinuities have been characterized by approximate and semi-analytical models, from which the reflection and transmission coefficients were derived. The first part of this thesis focuses on two possible simplified terminations of a 2D metallic half-space: i) dielectric and ii) metallic half-plane discontinuities. Following a review of electromagnetic theory behind plasmonics, SPP reflection coefficients from these terminations were derived through effective medium and mode-matching techniques. The validity and limits of these models were comparatively assessed through results obtained from finite-difference time-domain (FDTD) simulations in conjunction with the mode expansion method. The characteristic behavior of these terminations was associated with those of their counterparts in microwave transmission lines. The second part of this thesis involves the analysis of more complex geometries, including step and gap discontinuities, via approximate models and numerical results. The reflection and transmission coefficients of these discontinuities were contextualized within a microwave network formalism, which yielded intuitive results on the resonant behavior of SPPs at discontinuities with small dimensions.

# ÖZETÇE


**Yüzey Plazmon Polaritonlarının İki Boyutlu Süreksizliklerle Etkileşiminin İncelenmesi: Yansıma ve İletim**

**Suat Barış İplikçioğlu**

**Elektrik ve Elektronik Mühendisliği, Yüksek Lisans**

**18 Şubat 2022**

Yüzey plazmon polaritonları (SPP'ler), nanoteknoloji, iletişim ve yaşam bilimlerindeki olası uygulamaları nedeniyle son yıllarda kapsamlı bir şekilde incelenmiştir. Bu yüzey dalgalarının ışığı kırınım sınırının altına odaklayabilme özellikleri, plazmonik dalga kılavuzları ve nano-antenler gibi yeni nesil optik aygıtların üretilmesine olanak sağlamaktadır. Buna karşın, bu yapılarda bulunabilecek süreksizliklerin analizinde çoğunlukla tam ölçekli elektromanyetik çözümleyiciler kullanılmaktadır. Daha basit bir tasarım rotası sağlamak için, 20. yüzyılda mikrodalga devreleri için geliştirilenlere benzeyen, yaklaşık ancak verimli süreksizlik modellerine ihtiyaç duyulmaktadır.

Bu çalışmada, temel iki boyutlu süreksizliklerdeki SPP davranışı yaklaşık ve yarı analitik modeller aracılığı ile yansıma ve iletim katsayıları üzerinden incelenmiştir. Bu tezin ilk kısmı, iki boyutlu bir metalik yarı uzayın i) yalıtkan ve ii) metalik yarı düzlem süreksizlikler olarak iki olası basitleştirilmiş sonlandırması üzerine odaklanmaktadır: Plazmonik biliminin temelindeki elektromanyetik teorinin gözden geçirilmesinin ardından, bu sonlandırmalardaki SPP yansıma katsayıları, etkili ortam ve mod eşleştirme teknikleri ile türetilmiştir. Bu modellerin geçerliliği ve sınırları, mod açılımı yöntemi ile birlikte zamanda sonlu farklar (FDTD) simülasyonlarından elde edilen sonuçlarla karşılaştırmalı olarak değerlendirilmiştir. Ayrıca ilgili süreksizliklerin karakteristik özellikleri, mikrodalga iletim hatlarındaki benzerleriyle ilişkilendirilmiştir. Bu tezin ikinci kısmı, basamak ve aralık tipi süreksizlikler dahil olmak üzere daha karmaşık geometrilerin yaklaşık modeller ve simülasyon verileri ile analizini içmektedir. Bu süreksizliklerin yansıma ve iletim katsayıları, bir mikrodalga ağ biçiminde ile bağlamsallaştırılmıştır. Bu bağlamsallaştırma ile küçük boyutlu süreksizliklerde SPP'lerin rezonansı hakkında detaylı sonuçlar elde edilmiştir.

# ACKNOWLEDGMENTS

I would like to sincerely thank to my advisor, Prof. M. İrşadi Aksun, for providing me with guidance, invaluable support and useful comments. His wisdom and knowledge has shaped me profoundly as a researcher. I would also like to additionally thank him for introducing me to the vast realms of nano-optics and computational electromagnetics as an undergraduate student.

I would like to thank Assoc. Prof. Kaan Güven and Assoc. Prof. Lale Alatan for taking part in my thesis committee, as well as for their indispensable comments and suggestions. I would also like to offer my thanks to Serhat Tetikol, PhD, for his help during my masters research.

I would like to thank to my friends, Aylin Erdoğan, Emre Küçük, Onat Arısoy, Syed Sultan Shah Bukhari, Suat Kurt and Tuğba Naz Ayyıldız, for their support and all the great time spent together.

I would not be where I am here right now without the endless love and support of my dear parents, Nurten and Celal. I would like to express my gratitude to them for always believing in and encouraging me.

Finally, I would like to express my love and gratitude to my beloved fiancée İrem for her unconditional love and support. I am immensely grateful to have you in my life.

# TABLE OF CONTENTS

# LIST OF FIGURES

# ABBREVIATIONS

| | |
|---|---|
| DDA | Discrete-Dipole Approximation |
| EM | Electromagnetics |
| EME | Eigenmode Expansion |
| FDTD | Finite-Difference Time-Domain |
| GPOF | Generalized Pencil-of-Function |
| GRC | Generalized Reflection Coefficient |
| IMI | Insulator-Metal-Insulator |
| LRSPP | Long-Range Surface Plasmon Polariton |
| LSP | Localized Surface Plasmon |
| MIM | Metal-Insulator-Metal |
| MNP | Metallic Nanoparticle |
| PML | Perfectly Matched Layer |
| QCW | Quasi-Cylindrical Wave |
| SIBC | Surface Impedance Boundary Condition |
| SPP | Surface Plasmon Polariton |
| SRSPP | Short-Range Surface Plasmon Polariton |

# Chapter 1

# INTRODUCTION

Ever since the discovery of radio waves, efficient design of structures that manipulate and guide electromagnetic waves have been of the utmost importance to electrical engineers and applied physicists. Their collective efforts led to technological innovations that touch upon a wide-band of high-frequency spectrum, including antennas, waveguides, integrated circuits and sensors. In the realm of nano-optics, such endeavours led to the engineering of interfacial excitations on metals, materials which were onced shunned away from most photonic applications due to their absorptive properties. One of the oft-studied types of such excitations, *surface plasmon polaritons* (SPPs), offer exotic physical properties that are hard or even impossible to achieve by conventional means. Propagating in between metallo-dielectric interfaces, these guided waves shine out by their ability to localize light in dimensions smaller than the classical diffraction limit.

While there is a burgeoning interest in plasmonics as a separate field of study in the last two decades, the basic phenomena behind it is not a new discovery. The theoretical descriptions of similar surface modes date back to J. Zenneck's and A. Sommerfeld's independent studies on radiation over conducting half-spaces during the 1900s, which attracted considerable attention and controversy within the electromagnetics community ever since their introduction [1]. Nevertheless, the experimental observation of surface plasmons predate these discourses, having taken place as early as in 1902 by the means of intensity anomalies in metallic diffraction gratings [2]: unbeknownst to its discoverer, R.W. Wood, these anomalies pertained to a novel type of surface mode that was not unlike those studied by Zenneck and Sommerfeld [3]. Early experimental work on SPPs was performed by R. H. Ritchie [4, 5]

and E. N. Economou [6], among many others [7, 8]. With the advent of improved fabrication techniques, the applications of surface plasmons flourished: the name *plasmonics* as a distinct research field was introduced in 2001 by H. Atwater's research group in Caltech [9]. The field went through rapid developments ever since due to its implications in communications, biomedical engineering and energy sectors [10, 11, 12]: some of the notable developments in plasmonics include the physical realization of Pendry's sub-diffraction limited superlens [13], commercialization of novel types of biosensors [10] and introduction of plasmonic lasing [14].

As in the case for any guided waves in optics, the structures that are studied in plasmonics generally involve discontinuities, either as a critical design choice or as an inevitable byproduct of the fabrication process. Modeling these poses a particular challenge due to complexity of the problems involved, which generally have no analytical solutions. While the considerable improvements in the nanophotonic simulation tools in the last decades relatively eased the computation of SPP interactions [15], plasmonics is yet to go through the full-scale maturation that the *microwave theory and techniques* went through in the 20th-century. A large portion of the early formative years of microwave field theory was spent on the collective efforts of many trailblazing sciencists of the era, including the likes of N. Marcuvitz, J. Schwinger and S. A. Schelkunoff, to analyze and simplify the discontinuities that were encountered in RF waveguide design: the accumulated wealth of information on such models, i.e. the lumped-circuit model and microwave network theory, is considered as one of the crowning achievements of this field [16]. Nowadays, the responses and fundamental parameters of a vast number commonly-used discontinuities in microwaves, such as microstrip bends and steps, are well-established as simple closed-form formulas [17].

While the aforementioned models have been applied in the analysis of plasmonic nanostructures in the past [18, 19, 20, 21], many of these works largely depend on full-wave simulations for parameter extraction. Thus, semi-analytical and approximate characterization of canonical discontinuities on metallo-dielectric interfaces, such as the ones provided on Fig. 1.1, remains an open area of study. Albeit being very idealized forms of the actual discontinuities on metallic films, these strictly geo-

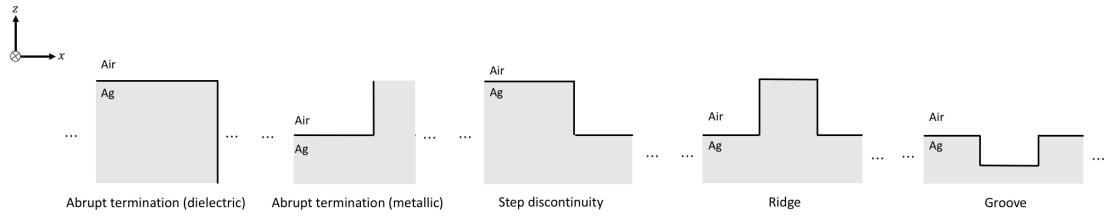


Figure 1.1: Various different types of metallo-dielectric discontinuities studied in this thesis

metrical and two-dimensional structures can offer insight into the characterization of their much complex counterparts. This thesis will focus on the analysis of reflection and transmission phenomena at these elements, which will be grouped into full-on terminations, step discontinuities and gaps.

To form a sufficient background prior to the discussion of salient plasmonic phenomena of interest, Chapter 2 will cover the fundamental electromagnetic theory behind plasmonics, as well as the relevant optical properties of metals that enable such phenomena. In order to provide a complete picture of metal optics, surface excitations on metallic nanoparticles, namely the localized surface plasmons (LSP) will also be covered. Chapter 3 will focus on the efficient and approximate routines to model the plasmonic interactions at the simplest canonical discontinuities, the surface terminations. The same chapter will also introduce the core full-wave analysis procedure of this study, the finite-difference time-domain (FDTD) method, that is to be used to assess the validity of the studied models throughout this thesis. As an extension of the work on its preceding chapter, Chapter 4 will offer numerical study on more complex step- and groove-like structures. The final remarks and a discussion on future work at Chapter 5 will conclude this thesis.

# Chapter 2

# THEORY OF PLASMONICS

Plasmonics studies the interaction of light with electron density oscillations at the metallic interfaces. Salient features of plasmonic excitations, namely the subwavelength light confinement and field enhancement, are enabled by the distinct optical properties of the metals. In metallic structures, light and plasmon coupling manifests itself either as surface plasmon polaritons (SPPs) at planar dielectric-metal interfaces or localized surface plasmons (LSPs) at metal nano-structures; the former represents the guided subwavelength surface modes and the latter pertains to the radiative or absorptive coupling in nanoparticles [22].

Since most applications of plasmonic interactions have mainly exploited the nature of plasmonic waves at the interfaces (generally referred to as SPPs) of planar structures composed of metal and dielectric layers, the theory of such waves needs to be based on electromagnetic analysis of layered structures. Therefore, the overview of SPPs would not be complete without a discussion of classical electrodynamics in stratified media. In this chapter, the fundamentals of plasmonics will be built on the very basics of electromagnetism, that is, the Maxwell's equations, in conjunction with optical properties of metals which are the integral parts of any configuration that could support plasmons (SPPs or any other SP resonances). Two cardinal plasmonic interactions are, in general, of main interest, namely surface plasmon polaritons (SPPs) and localized surface plasmons (LSPs), from which the former will lay basis for the forthcoming analyses throughout this thesis.

## *2.1 Electromagnetics in layered media*

### *2.1.1 Vectorial wave equation*

Modal analysis is a prerequisite for analyzing any electromagnetic structure, including but not limited to plasmonic waveguides. Within the limits of the classical theory, such properties can be deduced from Maxwell's equations, the pillars of electromagnetics and optics. These equations are given below in differential form with the $e^{-i\omega t}$ time dependence, which will be assumed throughout this thesis:

$$\nabla \cdot \mathbf{B} = 0 \tag{2.1a}$$

$$\nabla \times \mathbf{E} - i\omega\mathbf{B} = 0 \tag{2.1b}$$

$$\nabla \cdot \mathbf{D} = \rho \tag{2.1c}$$

$$\nabla \times \mathbf{H} + i\omega\mathbf{D} = \mathbf{J} \tag{2.1d}$$

where $\mathbf{E}$ and $\mathbf{H}$ refer to the electric and magnetic fields, and $\mathbf{D}$ and $\mathbf{B}$ are the respective flux densities for these fields, to which they are related with the constitutive relations by the dielectric permittivity ($\varepsilon_r\varepsilon_0$) and magnetic permeability ($\mu_r\mu_0$). The source terms $\mathbf{J}$ and $\rho$ represent the free current density and charge distribution in the system respectively; the term $\omega$ is the angular frequency of operation. Coupling of the curl equations in 2.1 (equations 2.1b and 2.1d) in a homogenous medium yields the generalized vector Helmholtz equations, which describe the wave nature of the electromagnetic fields:

$$\begin{aligned} \nabla \times \nabla \times \mathbf{E} - \frac{\omega^2}{c^2}\mu_r\varepsilon_r\mathbf{E} - i\omega\mu\mathbf{J} = 0 \\ \nabla \times \nabla \times \mathbf{H} - \frac{\omega^2}{c^2}\mu_r\varepsilon_r\mathbf{H} - \nabla \times \mathbf{J} = 0 \end{aligned} \tag{2.2}$$

where $c$ is the speed of light in vacuum and is defined by the vacuum permittivities and permeabilities ($c = 1/\sqrt{\varepsilon_0\mu_0}$).

A typical illustration of planarly layered media is given in Fig 2.1, where the structure is inhomogenous along $z$-direction and translationally invariant along $y$-axis. While each layer is assumed to be isotropic, the formulation can be expanded to anisotropic materials as well. This scheme will set the basis for the forthcoming analyses of plasmonic waveguides.

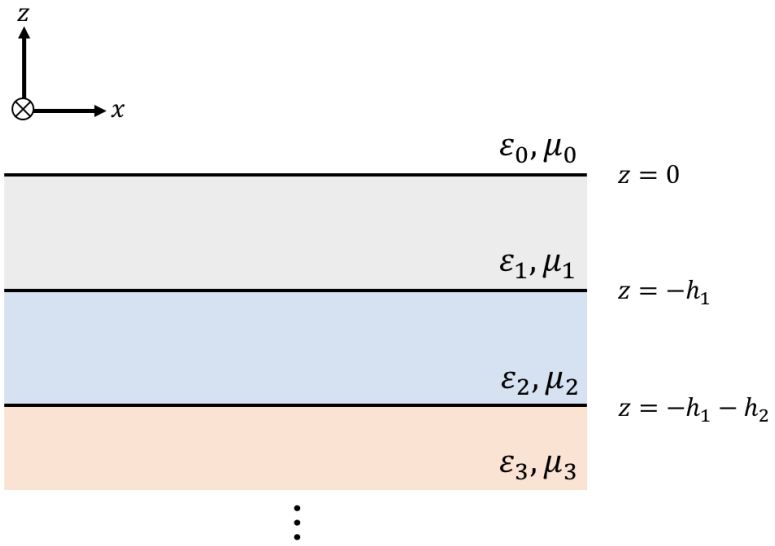


Figure 2.1: A typical example of planarly layered structures, where the layers are stacked along $z$-direction while they are infinite in $x-y$ plane. Thickness and electric and magnetic properties of the medium in Layer-$i$ are represented by $h_i$, $\varepsilon_i$ and $\mu_i$, respectively.

Translational invariance of the planarly layered structures, as sown in Fig. 2.1, in two dimensions enables us to decouple certain components of the field distribution, leading to two independent solutions; transverse electric (TE) and transverse magnetic (TM) waves, which feature the field components $(E_y, H_x, H_z)$ and $(E_x, E_z, H_y)$, respectively. The term "transverse" originates from the fact that either **E** or **H** has only field components tranverse to a plane of incidence, defined by the vectors of propagation and stratification axis.

As for any partial differential equation, modal analysis of an arbitrary structure necessitates the consideration of source-free circumstances. Before going any further, let us note that since SPPs are TM waves, in most examples and derivations we intend to use TM waves to lay the ground work for the SPPs for the future discussions. Having said that, as a starting example, the corresponding vector Helmholtz equation for the magnetic field in a stratified medium can be written from Maxwell's equations (2.1) as [17]:

$$\varepsilon_r(z)\nabla \times \frac{1}{\varepsilon_r(z)}\nabla \times \mathbf{H} - \frac{\omega^2}{c^2}\mu_r(z)\varepsilon_r(z)\mathbf{H} = 0 \tag{2.3}$$

Due to the stratification along $z$, the relative permittivities and permeabilities are functions of $z$, and hence, Eq. (2.3) is slightly different from the vector Helmoltz equation for $\mathbf{H}$ that was given in (2.2). By using a few vector identities on Eq. (2.3), demonstrated below:

$$\varepsilon_r(z)\left[\frac{1}{\varepsilon_r(z)}\underbrace{(\nabla\times\nabla\times\mathbf{H})}_{\nabla(\nabla\cdot\mathbf{H})-\nabla^2\mathbf{H}}+\left(\nabla\frac{1}{\varepsilon_r(z)}\right)\times(\nabla\times\mathbf{H})\right]-\frac{\omega^2}{c^2}\mu_r(z)\varepsilon_r(z)\mathbf{H}=0 \quad (2.4)$$

and using Gauss's law for magnetism (2.1a) and expanding the magnetic field of TM waves with its sole transverse component ($\mathbf{H}^{TM}=\hat{y}H_y$), the vector wave equation for $\mathbf{H}$ boils down to a scalar wave equation that describes the complete characteristics of TM waves. Since the structure is assumed to be invariant in $y$-axis, $y$-derivatives can be omitted, leading to the following differential equation for $H_y$:

$$\begin{aligned}\left(\frac{d^2}{dx^2}+\frac{d^2}{dz^2}\right)H_y-\varepsilon_r(z)\left(\frac{d}{dz}\frac{1}{\varepsilon_r(z)}\right)\frac{dH_y}{dz}+\frac{\omega^2}{c^2}\mu_r(z)\varepsilon_r(z)H_y=0\\ \left(\frac{d^2}{dx^2}+\frac{d^2}{dz^2}\right)H_y-\frac{d^2H_y}{dz^2}-\varepsilon_r(z)\frac{d}{dz}\frac{1}{\varepsilon_r(z)}\frac{dH_y}{dz}+\frac{\omega^2}{c^2}\mu_r(z)\varepsilon_r(z)H_y=0\\ \frac{d^2}{dx^2}H_y-\varepsilon_r(z)\frac{d}{dz}\frac{1}{\varepsilon_r(z)}\frac{dH_y}{dz}+\frac{\omega^2}{c^2}\mu_r(z)\varepsilon_r(z)H_y=0\end{aligned} \quad (2.5)$$

Further simplification can be achieved by assuming that the solution we are looking for is a wave propagating along $x$-axis, that is, the solution is expected to be in the form of

$$H_y(x,z)=H_y(z)e^{\pm i\beta x} \quad (2.6)$$

where $\beta$ is the unknown *propagation constant*, which is unique for a particular guided mode solution of the system and is the same in all layers due to the phase matching condition. The most basic form of the scalar TM wave equation thus becomes:

$$\varepsilon_r(z)\frac{d}{dz}\frac{1}{\varepsilon_r(z)}\frac{dH_y}{dz}+\left(\frac{\omega^2}{c^2}\mu_r(z)\varepsilon_r(z)-\beta^2\right)H_y=0 \quad (2.7)$$

and, following the same steps results in the governing wave equation for TE modes in the same geometry (Fig. 2.1) as:

$$\mu_r(z)\frac{d}{dz}\frac{1}{\mu_r(z)}\frac{dE_y}{dz}+\left(\frac{\omega^2}{c^2}\mu_r(z)\varepsilon_r(z)-\beta^2\right)E_y=0 \quad (2.8)$$

Since each layer is homogenous by itself, scalar wave equations can be reduced further more. For example, in a layer $j$, the corresponding wave equations would be:

$$\begin{aligned} \frac{d^2H_y}{dz^2} + \left(\frac{\omega^2}{c^2}\mu_j\varepsilon_j - \beta^2\right) H_y = 0 \\ \frac{d^2E_y}{dz^2} + \left(\frac{\omega^2}{c^2}\mu_j\varepsilon_j - \beta^2\right) E_y = 0 \end{aligned} \tag{2.9}$$

for TM and TE wave equations, respectively. Now, it is a simple matter to state the solutions of these wave equations as

$$\begin{aligned} H_y &= H_0 e^{\pm i\beta x} e^{\pm ik_{zj}z} \\ E_y &= E_0 e^{\pm i\beta x} e^{\pm ik_{zj}z} \end{aligned} \tag{2.10}$$

where $E_0$ and $H_0$ are arbitrary complex coefficients, $k_{zj}$ is the wavevector along $z$-direction in the $j^{\text{th}}$ layer:

$$k_{zj} = \sqrt{\frac{\omega^2}{c^2}\mu_j\varepsilon_j - \beta^2} \tag{2.11}$$

and $\beta$ is the unknown propagation constant of the surface wave that we are looking for. Note that $k_{zj}$ in Eq. (2.11) is the result of substituting the solutions (2.10) into Eq. (2.9).

### *2.1.2 Fresnel and generalized reflection coefficients*

Once the solutions of the wave equation (TE or TM) are obtained, albeit in a single layer and with unknown coefficients and propagation constant $\beta$, they need to comply with the boundary conditions in order to provide more specific solution sets for the geometry at hand. That is, the electric and magnetic fields in adjacent layers should satisfy the *boundary conditions* at the interface, say between the bordering layers $j$ and $j+1$, as summarized below:

$$\hat{n} \times (\mathbf{E}_j - \mathbf{E}_{j+1}) = 0 \tag{2.12a}$$

$$\hat{n} \times (\mathbf{H}_j - \mathbf{H}_{j+1}) = J_s \tag{2.12b}$$

$$\hat{n} \cdot (\varepsilon_j\mathbf{E}_j - \varepsilon_{j+1}\mathbf{E}_{j+1}) = \rho_s \tag{2.12c}$$

$$\hat{n} \cdot (\mu_j\mathbf{H}_j - \mu_{j+1}\mathbf{H}_{j+1}) = 0 \tag{2.12d}$$

where $\hat{n}$ is the unit normal vector for the interface. Furthermore, $J_s$ and $\rho_s$ refer to the surface current and charge densities at this interface, respectively. These source terms are zero as the layers are assumed to be of lossy dielectric or metallic materials with volume current and volume charge densities. Applying these boundary conditions to the fields, Fresnel reflection and transmission coefficients can be obtained for an incident plane wave with TE or TM polarization. These coefficients dictate how an incident plane wave is reflected and refracted from a surface, which is illustrated for a TM-polarized incident wave $(H_y, E_x, E_z)$ at a surface between two dielectric materials with permittivities $\varepsilon_j$ and $\varepsilon_{j+1}$ in Fig. 2.2. Reflection and transmission, as pictured in Fig. 2.2, can be considered to happen at the interface, at least from a macroscopic view point, where a portion of the incoming wave is reflected back and the rest is transmitted through the surface. For microscopic picture, interested readers can be referred to Ewald-Oseen extinction theorem [23]. As such, Fresnel coefficients denote the magnitude and phase of these reflected and transmitted components with respect to the incident wave.

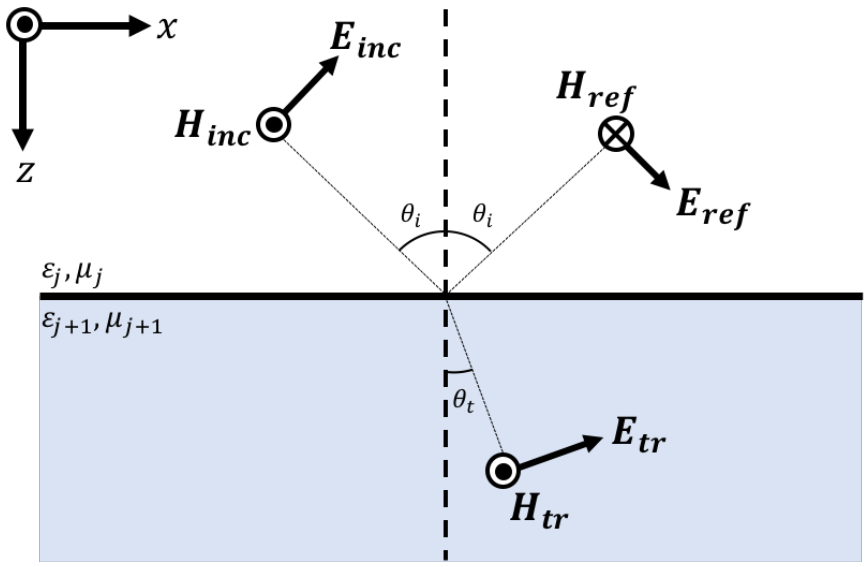


Figure 2.2: Reflection of a TM-polarized plane wave from a surface between two materials with different permittivities and permeabilities.

Although the derivations of Fresnel coefficients at a planar interface of two semi-infinite media are quite common in every em textbook, for the sake of completeness

and later referrals in the derivations of generalized coefficients in the case of multiple layers, these coefficients are derived below for the TM waves, using the information and parameters given in Fig. 2.2 ($\hat{n} = -z$). As shown in the figure, incident and reflected waves, and in turn, their field components are superimposed in layer-$j$ and there is only transmitted wave in layer-$(j+1)$. Therefore, the total magnetic fields can be written directly from this observation in both media and, since $\mathbf{H} = \hat{y}H_y$ has only the tangential component, applying the continuity of the tangential magnetic field at the interface ($z = 0$) results in

$$\begin{gathered} H_0 e^{i\beta x} e^{ik_{zj}z} - rH_0 e^{i\beta x} e^{-ik_{zj}z} = tH_0 e^{i\beta x} e^{ik_{z(j+1)}z} \text{ at } z = 0 \text{ and } \forall x \\ 1 - r = t \end{gathered} \tag{2.13}$$

where $r$ and $t$ denote Fresnel's reflection and transmission coefficients, respectively. In order to extract the unknown coefficients, we need two linearly independent equations, second of which we can derive by additionally enforcing the boundary condition for the electric fields (2.12a). Since we know the total magnetic fields in both media, the total electric fields can be obtained by using the Ampère-Maxwell law (2.1d). Then, implementing the boundary condition on the tangential components of the electric fields ($E_x$) at the interface (at $z = 0$ and $\forall x$) results in

$$\begin{aligned} \frac{k_{zj}}{\omega\varepsilon_j}\left[H_0 e^{i\beta x} e^{ik_{zj}z} + rH_0 e^{i\beta x} e^{-ik_{zj}z}\right] &= \frac{k_{z(j+1)}}{\omega\varepsilon_{j+1}} tH_0 e^{i\beta x} e^{ik_{z(j+1)}z} \\ \frac{k_{zj}}{\varepsilon_j}(1+r) &= \frac{k_{z(j+1)}}{\varepsilon_{j+1}} t \end{aligned}$$

Solving the equations (2.13) and (2.14) simultaneously, Fresnel reflection and transmission coefficients for a TM-polarized wave are obtained as follows:

$$r^{TM} = \frac{\varepsilon_{j+1}k_{zj} - \varepsilon_j k_{z(j+1)}}{\varepsilon_{j+1}k_{zj} + \varepsilon_j k_{z(j+1)}} \tag{2.14}$$

$$t^{TM} = \frac{2\varepsilon_{j+1}k_{zj}}{\varepsilon_{j+1}k_{zj} + \varepsilon_j k_{z(j+1)}} \tag{2.15}$$

For a TE-polarized incident plane wave (Fig. 2.3), the Fresnel coefficients can be derived through the transverse electric field, $\mathbf{E} = \hat{y}E_y$. Employing a similar routine as in the case for TM-polarized waves, the analogous reflection and transmission coefficients are thus obtained as

$$r^{TE} = \frac{\mu_{j+1}k_{zj} - \mu_j k_{z(j+1)}}{\mu_{j+1}k_{zj} + \mu_1 k_{z(j+1)}} \tag{2.16}$$

$$t^{TE} = \frac{2\mu_{j+1}k_{zj}}{\mu_{j+1}k_{zj} + \mu_j k_{z(j+1)}} \tag{2.17}$$

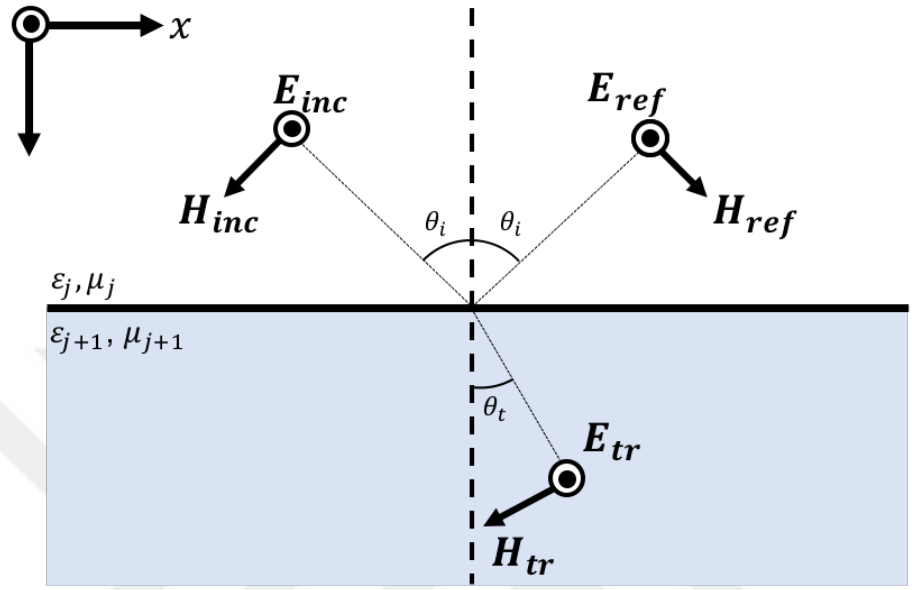


Figure 2.3: Reflection of a TE-polarized plane wave from a surface between two materials with different permittivities and permeabilities.

For the sake of clarity, it should be noted that Fresnel coefficients only account for a single interface between two semi-infinite media. However, for realistic structures, one needs to deal with multilayered geometries, for which the reflection and transmission coefficients need be generalized by taking multiple reflections and transmissions from other interfaces into account. For demonstration purposes, a three-layered configuration, which is also common for plasmonic media, has been used to derive the *generalized reflection coefficient* (GRC) for an incident plane wave propagating towards this structure, as shown in Fig. 2.4. Regardless of the polarization of incident wave, this expression, denoted by $\tilde{R}_{13}$, can be represented with an infinite sum of multiple reflections, a few of which have been shown in Fig. 2.4. The resulting series

evaluation of GRC is written as follows [24]:

$$\begin{aligned}\tilde{R}_{13} &= r_{12} + t_{12}t_{21}r_{23}e^{ik_{z2}2h} + t_{12}t_{21}r_{23}^2 r_{21}e^{ik_{z2}4h} + ... \\ &= r_{12} + t_{12}t_{21}r_{23}e^{ik_{z2}2h}\sum_{n=0}^{\infty}(r_{23}r_{21}e^{ik_{z2}2h})^n \\ &= r_{1,2} + \frac{t_{12}t_{21}r_{23}e^{ik_{z2}2h}}{1 - r_{21}r_{23}e^{ik_{z2}2h}} \\ &= \frac{r_{12} + r_{23}e^{ik_{z2}2h}}{1 + r_{12}r_{23}e^{ik_{z2}2h}}\end{aligned} \tag{2.18}$$

where $r_{ij}$'s and $t_{ij}$'s denote Fresnel reflection and transmission coefficients between the layers $i$ and $j$, respectively, and $t_{ij} = 1 - r_{ij}$ is used to obtain the last expression in (2.18).

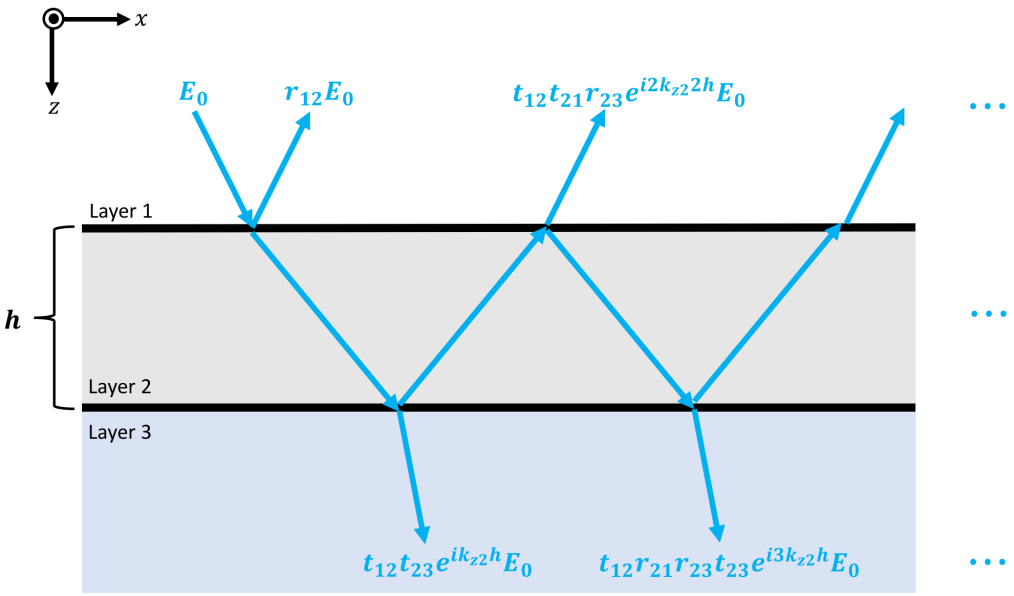


Figure 2.4: Illustration of multiple reflections and transmissions in a three-layered medium that give rise to generalized reflection and transmission of an arbitrarily polarized incident plane wave. Note that $h$ is the thickness of layer-2 where $k_{z2}$ is the wavevector along $z$. $r_{ij}$ and $t_{ij}$ represent the Fresnel coefficients for a plane wave propagating from layer-$i$ to layer-$j$.

For stacks with more than three layers, the same expression is used by changing the Fresnel reflection coefficient from layer 2 to layer 3, $r_{23}$, to the GRC $\tilde{R}_{23}$ in order to account for the multiple reflections coming from below layer 3. That is, the GRC $\tilde{R}_{12}$ is obtained recursively starting from the bottommost layer; this basically

corresponds to replacing each two adjacent layers by an effective medium. In optics literature, this procedure is referred to as Rouard's method and is often used in the analysis of thin-film stacks [25, 26]. Using the same series expansions, a transmission coefficient can also be obtained as:

$$t_{13} = \frac{t_{12}t_{23}e^{ik_{z2}h}}{1 - r_{21}r_{23}e^{ik_{z2}2h}} \tag{2.19}$$

## *2.2 Optical properties of metals*

Most salient characteristics of surface plasmons in visible to infrared frequencies are enabled by the optical properties of metals at these wavelengths; the crucial one is the negative permittivity. However, metals at microwave frequencies are usually modeled to be perfect conductors, as they have extremely high density of free electrons, rendering the material highly conductive, almost perfect conductor at these frequency ranges. Due to the frequency-dependent nature of dielectric functions, it is of utmost importance to understand and model these metals accurately enough to be able to exploit, modify or even tweak them in the applications of surface plasmons. Although the dielectric functions of metals have been well-studied and documented [27, 28], it is imperative to review a few of prevalent models that will be used for the subsequent simulations and computational analyses.

### *2.2.1 Drude model*

Dielectric and conductive properties of many metals can be modeled through Drude theory or its variants [22], which is one of the widely used model to describe the dielectric functions of metals. Proposed by Paul Drude in 1900 [29], the theory is classical by nature and attributes the optical and electrical properties of metals exclusively to the Newtonian motion of free electrons in their ionic lattices, which are collectively known as *free electron gas* or *plasma*. An inbound time-harmonic electromagnetic wave would polarize the plasma, which in turn would recoil due to the induced charge displacement; hence, the plasma oscillation, often quantized as a *plasmon* [30]. While the Drude model neglects the interaction between electrons and

lattice potentials [22], it incorporates the effects of collisions as a damping parameter [30].

The model starts with a single electron in an one-dimensional system and its behavior as a response to an electromagnetic force, known as the Lorentz force:

$$\mathbf{F} = q\mathbf{E} + q\mathbf{v} \times \mathbf{B} \tag{2.20}$$

Since the magnetic field in this context is relatively small as compared to the electric field, it can be neglected. Moreover, assuming that the electromagnetic force exerted on the electron is due to a plane wave with a harmonic dependence of $e^{-i\omega t}$, coupling the Lorentz equation to the Newtonian equation of motion results in a second-order inhomogenous differential equation that describes the displacement of the electron:

$$m_e \frac{d^2x}{dt^2} + m_e \nu \frac{dx}{dt} = -eE_0 e^{-i\omega t} \tag{2.21}$$

where $m_e$ refers to the mass of electron, $e$ is the unit charge and $\nu$ represents the damping term accounting for the collision effects. Due to the linearity of Eq. 2.21, the solution will have the same harmonic dependence as the electric field ($x = x_0 e^{-i\omega t}$), which would lead to the closed-form expression for the displacement $x$ as follows:

$$x = \frac{e}{m_e(\omega^2 + i\omega\nu)} E_0 e^{-i\omega t} \tag{2.22}$$

Once the displacement of a single electron is known, the polarization density $\mathbf{P}$ for a plasma of electrons with density $N_f$ can be written simply as a multiple of charge per unit volume and the displacement, that is, $\mathbf{P} = -eN_f\mathbf{x}$. Now, with the help of the constitutive relation for the displacement field ($\mathbf{D} = \varepsilon_m\varepsilon_0\mathbf{E} = \varepsilon_0\mathbf{E} + \mathbf{P}$), the expression for the dielectric function of metals is obtained as

$$\begin{aligned} \varepsilon_m(\omega) &= \varepsilon_\infty - \frac{\frac{N_f e^2}{m_e \varepsilon_0}}{\omega(\omega + i\nu)} \\ &= \varepsilon_\infty - \frac{\omega_p^2}{\omega(\omega + i\nu)} \end{aligned} \tag{2.23}$$

where $\omega_p$ refers to the *plasma frequency*, $\varepsilon_\infty$ is the relative background permittivity in the high-frequency limit, and $\nu$ appears as the *collision frequency* as intended in Eq. (2.21).

The imaginary part of the dielectric function by the Drude model also provides an expression for the effective AC conductivity $\sigma(\omega)$ of metals. Using Ohm's law ($\mathbf{J} = \sigma\mathbf{E}$) in Ampère-Maxwell equation (2.1d) gives us a clue how to relate conductivity to the imaginary part of the dielectric function. Thus, a simple manipulation of the dielectric function gives us its imaginary part, which would yield the conductivity of a Drude metal as follows:

$$\sigma(\omega) = \frac{\omega_p^2 \nu}{\omega^2 + \nu^2} \tag{2.24}$$

### *2.2.2 Limits and extensions of Drude model*

For noble metals such as gold and silver, the Drude model fails to capture the effects of interband transitions in the visible to ultraviolet frequencies [22]. This is demonstrated by the plot, given in Fig. 2.5, that compares the dielectric function by the Drude Model to the experimental data by Babar and Weaver in between 250 to 1200 nm wavelengths for silver [31]. Since these materials and this frequency band are of high interest in many plasmonic applications, extensions of the Drude model are often used for accuracy when necessary.

#### *Lorentz-Drude model*

In order to discuss the Lorentz-Drude (LD) model, it is necessary to introduce the Lorentz oscillator. This model incorporates the attraction of electrons to the ionic cores; as a result, the electron plasma is not completely free. Introducing an additional position term to Eq. (2.21) with a restoring force coefficient, $\kappa$, we can obtain the following harmonic oscillator equation [30]:

$$m_e \frac{d^2x}{dt^2} + m_e \nu \frac{dx}{dt} + m_e \kappa x = -eE_0 e^{-i\omega t} \tag{2.25}$$

When solved in a similar manner to the derivation of the Drude model, the Lorentzian extension yields the following expression with a natural frequency $\omega_0 = \sqrt{\kappa}$:

$$\varepsilon_m(\omega) = \varepsilon_\infty - \frac{\omega_p^2}{(\omega^2 - \omega_0^2) + i\omega\nu} \tag{2.26}$$

Nevertheless, this classical model alone does not paint the full picture. Since quantum effects of light-matter interaction translate to different absorption and interband

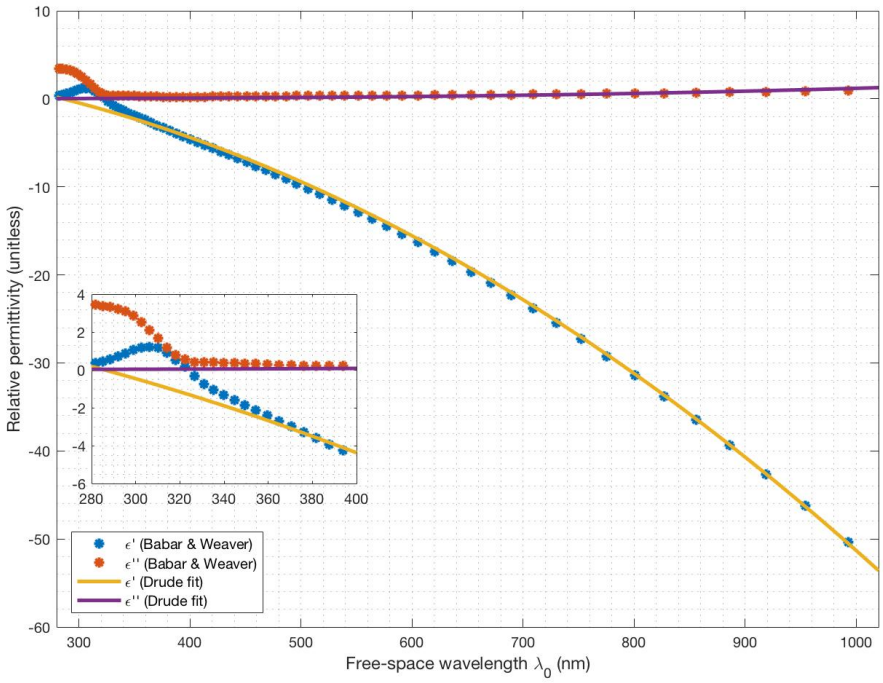


Figure 2.5: Dielectric function for silver compared: the Drude model vs experimental data. Significant deviation of the Drude model over the violet to ultraviolet band is attributed to interband transitions. The optimal Drude parameters, obtained by the simplex method, are $\varepsilon_\infty$ =4.5676, $\omega_p$ =1.4086e16 rad/s and $\nu$ =4.0307e+13 rad/s.

transition profiles at varying energies, the dielectric function should consist of multiple, compensating oscillators with different coefficients. This yields the explicit expression for the LD model as [32]:

$$\varepsilon_m(\omega) = \varepsilon_\infty - \frac{f_0\omega_p^2}{\omega(\omega + i\omega\nu_0)} + \sum_{j=1}^{N} \frac{f_j\omega_p^2}{(\omega^2 - \omega_j^2) + i\omega\nu_j} \tag{2.27}$$

The model features an offset Drude term with different $N$ oscillators; each oscillator term has its own strength coefficient ($f_j$), collision frequency ($\nu_j$) and natural frequency ($\omega_j$), denoted by the subscript $j$. These parameters can be obtained from the experimental data through optimization methods such as simulated annealing algorithm [32].

*Alternative models*

Alternative to the aforementioned dielectric function models are also used in various plasmonic applications; for the sake of completeness, these will be briefly mentioned. Critical-point model, proposed by Etchegoin et al. in 2006, introduces two extra interband transition terms to the ordinary Drude function [33]:

$$\varepsilon_m(\omega) = \varepsilon_\infty - \frac{\omega_p^2}{\omega(\omega + i\nu)} + G_1(\omega) + G_2(\omega) \tag{2.28}$$

Each transition term can are expanded as:

$$G_m(\omega) = A_m \Omega_m \left( \frac{e^{\phi_m}}{\Omega_m - \omega - i\Gamma_m} + \frac{e^{-\phi_m}}{\Omega_m + \omega + i\Gamma_m} \right) \tag{2.29}$$

where the parameters $\Omega_m$, $\Gamma_m$ and $\phi_m$ pertain to the energy, broadening and phase of the critical transitions, respectively. This model has been efficiently used in the FDTD simulations through recursive convolution [34].

Another approach to the dielectric function modeling, the BB model was proposed by F.L. Brendel and D. Bormann in 1992 [35]: it approximates the Lorentz-Drude dielectric function as a continuum of harmonic oscillators as described by a Gaussian distribution around the critical absorption points. As for the LD model, the optimal parameters for each function can be obtained numerically from the experimental data. Even though the model showcases a more proper absorption profile compared to the LD model [32], it reportedly does not satisfy the Kramers–Kronig relations according to a recent study [36].

## *2.3 Surface plasmon polaritons*

As guided modes of an open structure take on the form of *surface waves* [37], for metal-dielectric structures in the optical regime, these take on the form of surface plasmons polaritons (SPP). These modes originate from the coupling of electromagnetic waves with oscillations in free-electron gas density in metal at the interface of metal and dielectric. SPPs are tightly confined to these interfaces; as a result, these excitations can bypass the classical diffraction limit.

In this section, basic characteristics of SPPs in stratified media will be introduced, starting from their dispersion relations and field distributions.

### *2.3.1 Surface plasmon polaritons at a single interface*

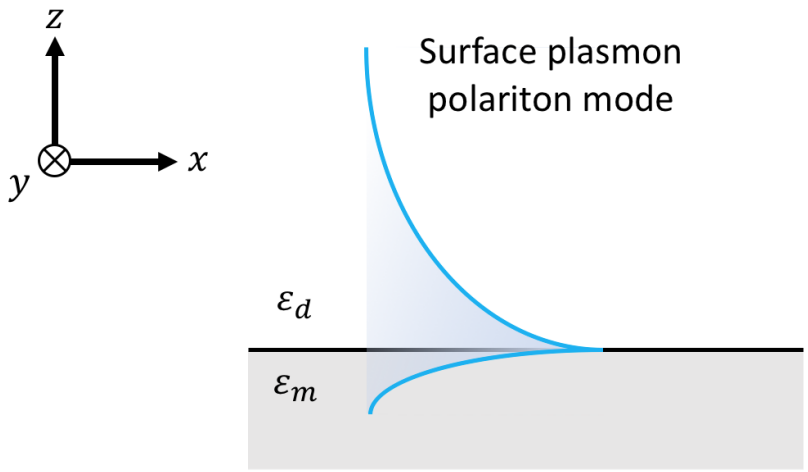


Figure 2.6: A typical SPP mode profile (blue line) at the cross-section of a dielectric layer ($\varepsilon_d$) and metallic layer ($\varepsilon_m$).

As for any guided mode, SPPs can be characterized by their propagation constants. For a surface mode in layered media, this constant can be extracted from the poles of the associated GRC. This is often known as *transverse resonance condition* [24]. For a single interface consisting of two semi-infinite media as in Fig. 2.6, the GRC reduces down to the ordinary Fresnel coefficients. Thus, the poles of the Fresnel reflection coefficient would yield the dispersion relation for the surface wave mode; for the TM case, this can be represented as:

$$\begin{aligned} \varepsilon_m k_{zd} &= -\varepsilon_d k_{zm} \\ \varepsilon_m \sqrt{\varepsilon_d \mu_d k_0^2 - \beta^2} &= -\varepsilon_d \sqrt{\varepsilon_m \mu_m k_0^2 - \beta^2} \end{aligned} \tag{2.30}$$

where $\varepsilon$ and $\mu$ with subscripts $d$ and $m$ denote the relative permittivities and permeabilities of the dielectric and metal layers, respectively. Equation (2.30) implies that, as could be shown easily, for the TM surface wave modes to exist, one of the permittivities should be negative, which is satisfied by the metal at optical frequencies as discussed earlier. The analogous equality for the TE surface wave modes, based on the corresponding Fresnel reflection coefficient (2.16), implies negative magnetic

permeability, which is not possible for materials that exist in nature [22], but can be artificially engineered as in the case of metamaterials. These "meta-plasmonic" modes are also known as *magnetic surface plasmons* [38]. Hence, it is safe to proceed with the assumption that only the TM guided modes are permitted for a single interface waveguide. Consequently, further algebraic manipulations of Eq. (2.30) yield:

$$\beta = k_0 \sqrt{\frac{\varepsilon_m^2 \varepsilon_d \mu_d - \varepsilon_d^2 \varepsilon_m \mu_m}{\varepsilon_m^2 - \varepsilon_d^2}} \tag{2.31}$$

As most materials that are used in plasmonics are non-magnetic ($\mu_d = \mu_m = 1$), the expression simplifies to a well-known SPP dispersion relation for a single interface:

$$\beta = k_0 \sqrt{\frac{\varepsilon_d \varepsilon_m}{\varepsilon_d + \varepsilon_m}} \tag{2.32}$$

The dispersion diagram for the SPPs at the interface between air ($\varepsilon_d = 1$) and silver are given in Fig. 2.7, where a Drude fit by Blaber et al. [39] is used to model the dielectric function of silver and the axes are normalized with respect to the plasma frequency, $\omega_p$.

One particular observation regarding the dispersion relation in Fig. 2.7 is that below a certain frequency, the real part of the propagation constant (blue line) exceeds the light line, which indicates sub-wavelength operation, albeit with an increasing loss (red line). At a particular frequency, denoted by $\omega_{\mathrm{SPP}}$ and shown in the figure by the green dashed line, the dispersion curve rapidly back-bends, roughly corresponding to $\omega_p/\sqrt{\varepsilon_\infty + \varepsilon_d}$ and characterized as the *surface plasmon resonance frequency* or *backbending frequency* [40]. Beyond this limit, a gap of quasi-bound modes forms and the dispersion curve is no longer able to penetrate beyond the light line [22]. In the low-frequency limit, the curve closely follows the light line, exciting surface modes that are known as Sommerfeld-Zenneck waves [41].

It is also possible to characterize SPP dispersion for complex frequencies and real wavevectors [41, 42], as provided in Fig. 2.8 for the same Drude parameters. In contrast to the previous plot, the dispersion relation is obtained inversely from the complex roots of Eq. (2.32). For the sake of visual simplicity, the negative imaginary parts of the complex frequencies are not plotted. In this particular case,

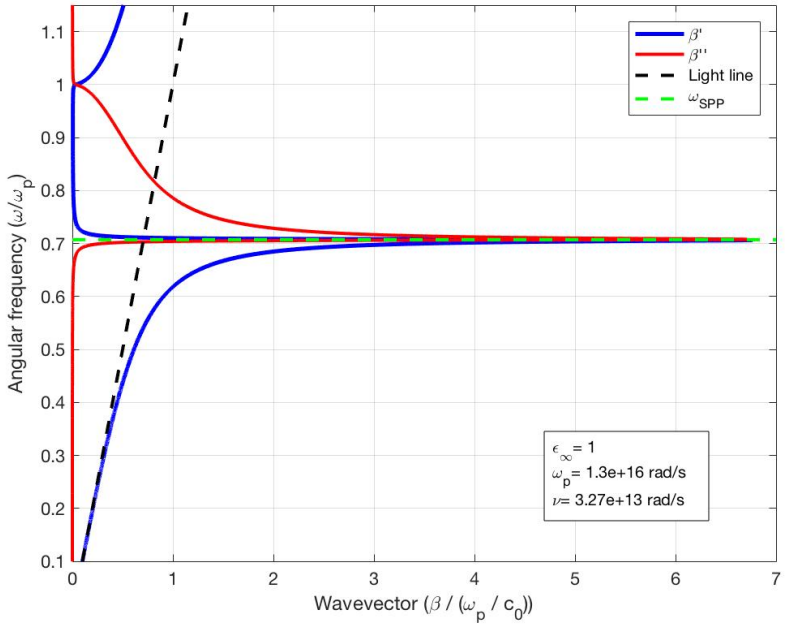


Figure 2.7: Dispersion relation of the SPPs at the interface between air and silver for real normalized frequencies $\omega/\omega_p$. The resonant SPP frequency is highlighted in green. Real and imaginary parts of the complex propagation constant ($\beta = \beta' + i\beta''$) are plotted with different colors, and relevant Drude parameters are provided in inset.

the dispersion curve does not backbend at the SPP resonance frequency; instead, it asymptotically increases to large wavevectors. In between the SPP resonance and bulk plasmon frequencies, a band gap forms. The discrepancy between these two results can be reconciled through viewing the curves as cross sections of a dispersion surface in the complex $\beta - \omega$ space [40]: the resulting complex dispersion surface is provided on Fig. 2.9 for an air-aluminium interface. The dispersion surface formulation, as well as the Drude permittivity parameters for aluminium, were adapted from [40].

One distinct implication of these dispersion relations pertains to the excitation of the cardinal SPP modes. Since these modes lie beyond the light line, they cannot be excited with free-space optical beams. As a result, more sophisticated phase-matching techniques are necessary to excite the SPP. These include near-field optical coupling, grating coupling and electron diffraction [22]. One of the most common

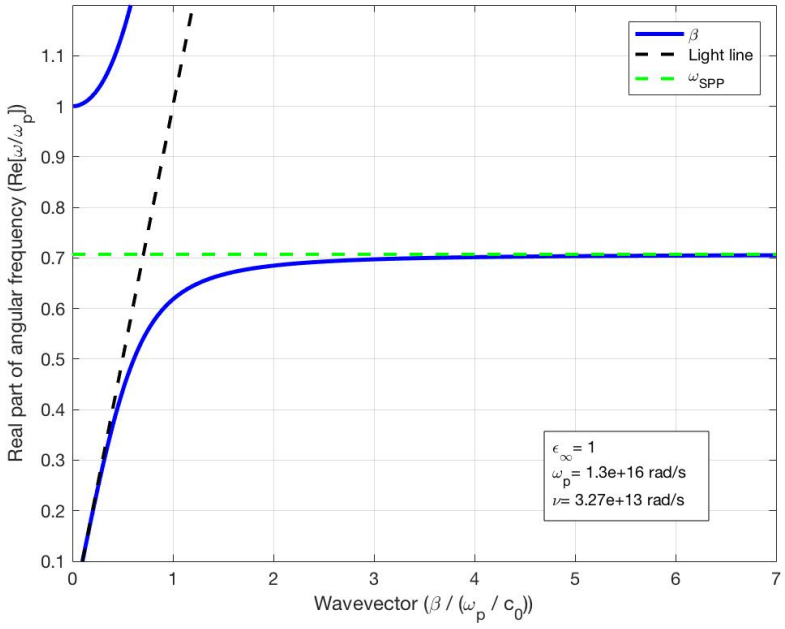


Figure 2.8: Dispersion relation of the SPPs at the interface between air and silver for real wavevectors. The resonant SPP frequency is highlighted in green. Relevant Drude parameters are provided in inset.

methods for the SPP excitation, prism coupling, will be briefly overviewed in Section 2.3.2 due to its multi-layered nature.

After the deduction of the appropriate propagation constant, the field expressions for the SPPs can be derived. Since TM modes are of main interest, the electric field components can be derived directly from the only magnetic field component $H_y$:

$$H_y(x,z) = \begin{cases} Ae^{-k_{z1}z}e^{i\beta x} & z \geq 0 \quad \text{(layer 1: Dielectric)} \\ Ae^{k_{z2}z}e^{i\beta x} & z \leq 0 \quad \text{(layer 2: Metal)} \end{cases} \tag{2.33}$$

where $A$ is the unknown coefficient and selected the same in both regions as the tangential magnetic fields at the interface ($z = 0$) must satisfy the boundary condition, that is, must be continuous (2.12b). The transverse wavevectors $k_{z1}$ and $k_{z2}$ obey the momentum conservation condition in their respective layers:

$$k_{zj} = \mp\sqrt{\beta^2 - \varepsilon_j k_0^2} \text{ for } j = 1, 2 \tag{2.34}$$

Since both layers are semi-infinite, the Sommerfeld radiation condition needs to be satisfied, by appropriately selecting the branch of the square root to ensure that the

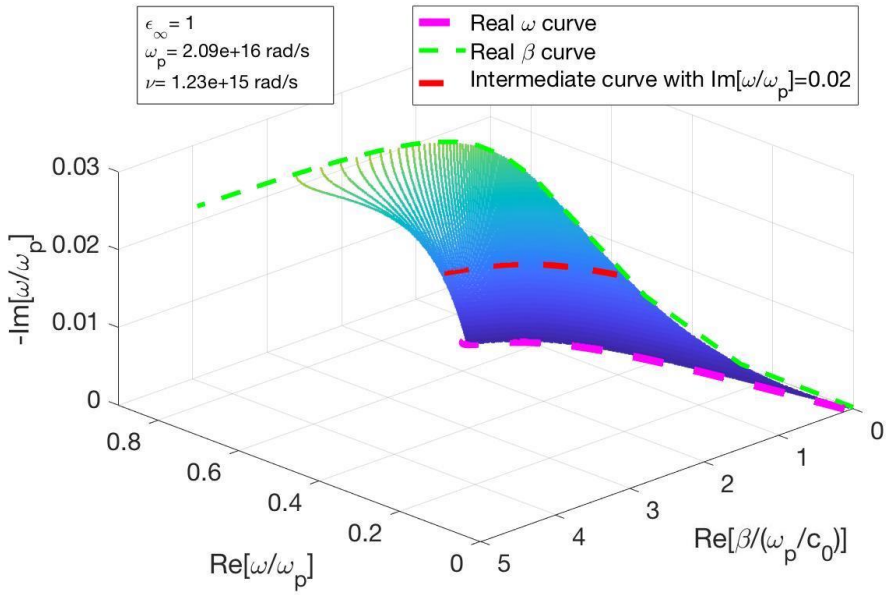


Figure 2.9: Dispersion surface of the SPPs at the interface between air and aluminum, whose Drude parameters were provided in the inlet. The pink and green curves correspond to real $\omega$-complex $\beta$ and complex $\omega$-real $\beta$ plots, respectively. The red curve signifies an intermediate temporal loss value.

fields decay into infinity [24]. Substituting Eq. (2.33) into the source-free Ampère-Maxwell law (2.1d), the electric field components can be obtained:

$$E_z(x,z) = \begin{cases} \dfrac{-\beta}{\omega\varepsilon_0\varepsilon_1} A e^{-k_{z1}z} e^{i\beta x} & z \geq 0 \quad \text{(layer 1)} \\ \dfrac{-\beta}{\omega\varepsilon_0\varepsilon_2} A e^{k_{z2}z} e^{i\beta x} & z \leq 0 \quad \text{(layer 2)} \end{cases} \tag{2.35}$$

$$E_x(x,z) = \begin{cases} \dfrac{-k_{z1}}{i\omega\varepsilon_0\varepsilon_1} A e^{-k_{z1}z} e^{i\beta x} & z \geq 0 \quad \text{(layer 1)} \\ \dfrac{k_{z2}}{i\omega\varepsilon_0\varepsilon_2} A e^{k_{z2}z} e^{i\beta x} & z \leq 0 \quad \text{(layer 2)} \end{cases} \tag{2.36}$$

Note that the SPP modes are not purely evanescent in $z$-direction (transverse to the propagation of the SPP modes) as $k_z$'s turn out to be complex, as the result of the complex nature of the SPP propagation constant $\beta$ and the material loss (2.34).

### *2.3.2 Multi-layered plasmonic waveguides*

Planar waveguides consisting of multiple layers are also able to support SPP modes. When the layers are sufficiently thin that SPPs at the adjacent interfaces interact,

they couple and form two independent *coupled modes*, referred to as symmetric and anti-symmetric modes [43].

There are basically two multilayer configurations that are commonly studied in the context of SPPs, which are namely metal-insulator-metal (MIM) and insulator-metal-insulator (IMI) waveguides. To understand the salient features of SPPs in these structures, their dispersion relations ($\omega - \beta$ relation) need to be derived and studied. As in the case of two semi-infinite media discussed in the previous sections, invoking the transverse resonance condition for these three-layer geometries provides the dispersion relation as:

$$1 + r_{21}^{TM} r_{23}^{TM} e^{ik_{z2}2h} = 0 \tag{2.37}$$

where $h$ and $k_{z2}$ refer to the thickness and transverse wavevector of the intermediate layer, as shown in Fig. 2.4. Note that this expression also yields the poles of the GRC (2.18). The propagation constants of the guided SPP modes in these three-layer geometries can be obtained from the solutions of Eq. (2.37) for $\beta$, which can only be done numerically.

*Metal-insulator-metal (MIM) waveguides*

If the insulator layer in a MIM configuration, as shown in Fig. 2.10, is thick enough that there is no or negligible interaction between the SPP modes at both MI and IM interfaces, the geometry becomes uninteresting as the whole structure can be treated as two separate metal-insulator waveguides, as it has been done in the previous section. However, if the insulating layer is sufficiently thin, then the fundamental modes of a MIM waveguide become coupled modes of the individual SPPs at both interfaces with different propagation constants. This is a result of the interaction of the fields in the dielectric layer, as demonstrated in Fig. 2.10. The spatial distribution profiles of the coupled modes can be obtained by simple application of the boundary conditions at each interface, with the implicit assumption of exponential dependence in each layer [22].

For a MIM waveguide with a free-space insulator of thickness $2a$ and centered at $z = 0$, Fig. 2.10, the only existing magnetic field component in the TM polarization,

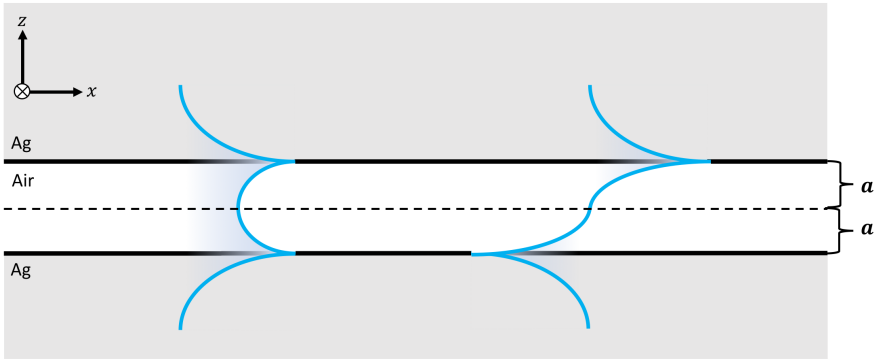


Figure 2.10: A symmetric MIM waveguide. Real part of the magnetic field profiles for the symmetric *(left)* and anti-symmetric *(right)* fundamental modes are also shown in blue.

$H_y$, can be written simply as follows:

$$H_y(x,z) = \begin{cases} Ae^{-k_{z1}z}e^{i\beta x} & z \geq a \quad \text{(layer 1)} \\ \left(Ce^{-k_{z2}z} + De^{k_{z2}z}\right)e^{i\beta x} & a \geq z \geq -a \quad \text{(layer 2)} \\ Be^{k_{z1}z}e^{i\beta x} & z \leq -a \quad \text{(layer 3)} \end{cases} \tag{2.38}$$

where $A$, $B$, $C$ and $D$ are unknown coefficients, and $\beta$ is the unknown wavevector for the SPPs supported by the geometry. Due to the translational invariance of the system (phase matching condition), all components share the same wavevector in $x$-direction, $\beta$. Also, as a result of the axial symmetry (semi-infinite layers are of the same material), the transverse wavevectors ($k_z$'s) at the semi-infinite layers should be the same. Once the magnetic field is known, at least its functional form, the electric field components in each layer can be obtained from the magnetic field through the Ampère–Maxwell law (2.1d) as

$$E_x(x,z) = \begin{cases} \dfrac{-k_{z1}}{i\omega\varepsilon_m\varepsilon_0}Ae^{-k_{z1}z}e^{i\beta x} & z \geq a \quad \text{(layer 1)} \\ \left(-k_{z2}Ce^{-k_{z2}z} + k_{z2}De^{k_{z2}z}\right)\dfrac{e^{i\beta x}}{i\omega\varepsilon_0} & a \geq z \geq -a \quad \text{(layer 2)} \\ \dfrac{k_{z1}}{i\omega\varepsilon_m\varepsilon_0}Be^{k_{z1}z}e^{i\beta x} & z \leq -a \quad \text{(layer 3)} \end{cases} \tag{2.39}$$

$$E_z(x,z) = \begin{cases} \dfrac{-\beta}{\omega\varepsilon_m\varepsilon_0} A e^{-k_{z1}z} e^{i\beta x} & z \geq a \quad \text{(layer 1)} \\ \left(Ce^{-k_{z2}z} + De^{k_{z2}z}\right) \dfrac{-\beta e^{i\beta x}}{\omega\varepsilon_0} & a \geq z \geq -a \quad \text{(layer 2)} \\ \dfrac{-\beta}{\omega\varepsilon_m\varepsilon_0} B e^{k_{z1}z} e^{i\beta x} & z \leq -a \quad \text{(layer 3)} \end{cases} \tag{2.40}$$

The application of boundary conditions for the tangential electric and magnetic fields at $z = a$ yields the following coupled equations:

$$\begin{aligned} Ae^{-k_{z1}a} &= Ce^{-k_{z2}a} + De^{k_{z2}a} \\ \frac{k_{z1}}{\varepsilon_m} Ae^{-k_{z1}a} &= k_{z2}Ce^{-k_{z2}a} - k_{z2}De^{k_{z2}a} \end{aligned} \tag{2.41}$$

Since we are looking for the natural modes of the geometry with no excitation, our intention is to find the dispersion relation that will help us get the propagation constant of the SPPs ($\beta$'s). Therefore, using the symmetry feature of the geometry, the fields in the dielectric region (insulator) can be written as a superposition of two oppositely traveling waves with the same amplitude, albeit possibly with different signs ($C = D$ or $C = -D$). Based on this argument, there are two possible solutions for such symmetric MIM configurations, which correspond to *symmetric* ($C = D$) and *anti-symmetric* ($C = -D$) magnetic field distributions with two distinct dispersion relations, respectively. Hence, solving Eqs. (2.41) simultaneously for these two conditions, the dispersion relations in the form of transcendental equations are obtained as follows [22]:

$$\begin{aligned} &k_{z1} + \varepsilon_m k_{kz2} tanh(-k_{z2}a) = 0 \quad \textit{(Symmetric)} \\ &k_{z1} + \varepsilon_m k_{kz2} coth(-k_{z2}a) = 0 \quad \textit{(Anti-symmetric)} \end{aligned} \tag{2.42}$$

It should be noted that anti-symmetric modes are often harder to excite, since their propagation constants are further away from the light line in the complex dispersion plane, and only exist in certain frequencies [44, 45]; as a result, symmetric modes are generally considered in the applications of MIM structures. Moreover, while MIM waveguides with thin insulating layer are able to support highly confined modes, particularly for shorter wavelengths, the propagation loss becomes higher with the increase of confinement as they are inversely proportional [44]. Similarly, as symmetric modes offer lower loss with lesser energy confinement, anti-symmetric

ones are associated with a higher degree of field enhancement near the interfaces while being relatively lossy [22, 46]. We should also note that, in addition to their fundamental modes, MIM waveguides are able to support higher-order TM modes as well [47].

*Insulator-metal-insulator waveguides*

Field distributions and dispersion relations of insulator-metal-insulator (IMI) waveguides are essentially in the same form as the MIM waveguides, albeit with different dispersive properties. Thus, the dispersion relations for symmetric and anti-symmetric modes can be respectively written as:

$$\begin{aligned} &\varepsilon_m k_{z1} + k_{z2} tanh(-k_{z2}a) = 0 \quad \textit{(Symmetric)} \\ &\varepsilon_m k_{z1} + k_{z2} coth(-k_{z2}a) = 0 \quad \textit{(Anti-symmetric)} \end{aligned} \tag{2.43}$$

Symmetric and anti-symmetric modes of an IMI waveguide are also referred to as *long-range* (LRSPP) and *short-range* (SRSPP) surface plasmon modes, whose magnetic field profiles are depicted in Fig. 2.11. Naming the long- and short-range in the SPPs in IMI waveguides are due to the propagation distances that these modes travel along the interface; that is, the propagation constants of SRPPs are located further away from the light line compared to the LRSPPs, resulting in a higher field confinement but a larger propagation loss [22].

Assuming the same transverse magnetic field dependency as in Eq. (2.38), the corresponding electric fields can be written as:

$$E_x(x,z) = \begin{cases} \dfrac{-k_{z1}}{i\omega\varepsilon_0} A e^{-k_{z1}z} e^{i\beta x} & z \geq a \quad \text{(layer 1)} \\ \left(-k_{z2} C e^{-k_{z2}z} + k_{z2} D e^{k_{z2}z}\right) \dfrac{e^{i\beta x}}{i\omega\varepsilon_m\varepsilon_0} & a \geq z \geq -a \quad \text{(layer 2)} \\ \dfrac{k_{z1}}{i\omega\varepsilon_0} B e^{k_{z1}z} e^{i\beta x} & z \leq -a \quad \text{(layer 3)} \end{cases} \tag{2.44}$$

$$E_z(x,z) = \begin{cases} \dfrac{-\beta}{\omega\varepsilon_0} A e^{-k_{z1}z} e^{i\beta x} & z \geq a \quad \text{(layer 1)} \\ \left(C e^{-k_{z2}z} + D e^{k_{z2}z}\right) \dfrac{-\beta e^{i\beta x}}{\omega\varepsilon_m\varepsilon_0} & a \geq z \geq -a \quad \text{(layer 2)} \\ \dfrac{-\beta}{\omega\varepsilon_0} B e^{k_{z1}z} e^{i\beta x} & z \leq -a \quad \text{(layer 3)} \end{cases} \tag{2.45}$$

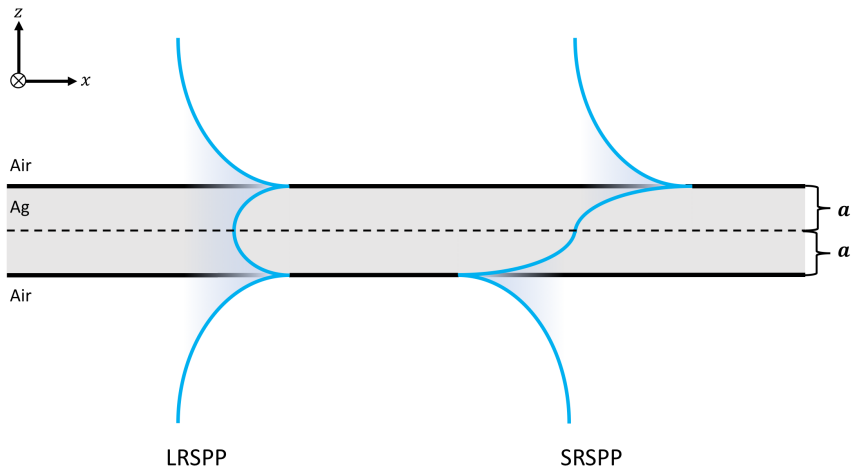


Figure 2.11: A symmetric IMI waveguide. Magnetic field profiles for the two fundamental modes, LRSPP *(left)* and SRSPP *(right)* are also shown in blue.

*Other types of multi-layered waveguides*

Certain types of asymmetric layered waveguides such as Otto and Kretschmann-Raether configurations, are able to support coupled SPPs. These two morphologies form the basis for prism coupling method of SPP excitation [22]. Even though the mechanism behind this method is often attributed to the attenuated total internal reflection phenomenon [22], this has been contested by the recent work [40, 48, 49], which indicate the phenomenon to be the complex response of the overall layered system.

The generalized reflection analysis can be extended to locate modes of multi-layered waveguides. One type of such waveguide, Tamm plasmon waveguide, consists of a metallic layer and an adjacent Bragg mirror or a photonic crystal. Unlike standard plasmonic waveguides, these can be excited with incoming plane waves as their dispersion curve lies within the light cone. The modes of such waveguides present themselves both in TE and TM polarizations [50, 51]. Analysis and properties of Tamm plasmonic structures are beyond the scope of this thesis.

## *2.4 Localized surface plasmons*

Another well-studied type of plasmonic excitation is known as localized surface plasmon (LSP). Observed in metallic nanoparticles (MNP) and nanostructures, LSPs are characterized by very strong field enhancements in the vicinity of the particle surface, which lay the basis for many distinct applications in biosensing and surface-enchanced Raman spectroscopy [52]. Unlike SPPs, these can be excited through plane waves [22].

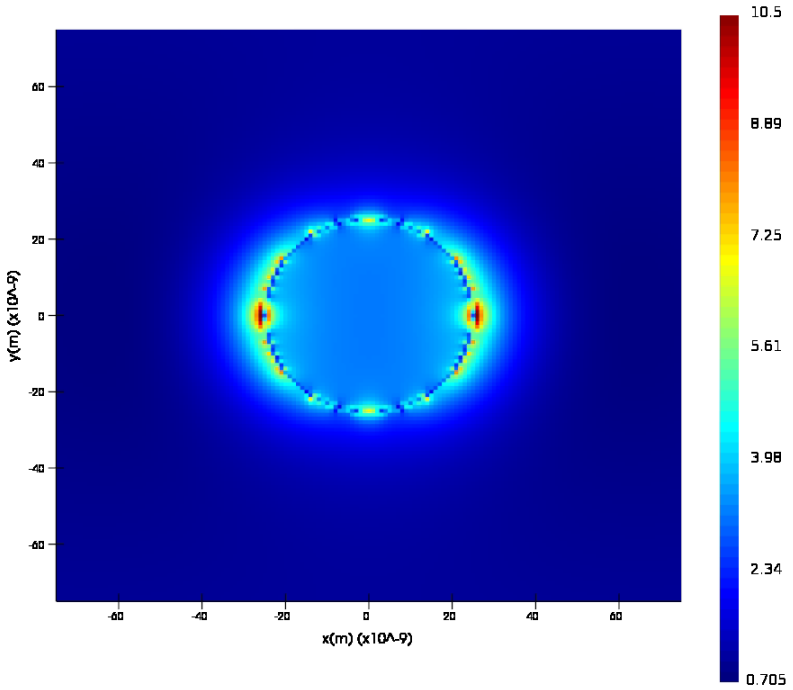


Figure 2.12: Magnitude of electric field ($|E|$) distribution of the LSP resonance around a MNP with a radius of 25 nm. The dielectric function is modeled by the Drude model with the following parameters: $\varepsilon_\infty = 1$, $\omega_p = 9.3891e15$ rad/sec and $\nu = 1.0635e15$ rad/sec. The MNP is excited by a $y$-polarized plane wave near the LSP resonance wavelength of 347 nm. The central cross section of the MNP is normal to the incident plane wave. Scattered fields are obtained through FDTD by the total-field/scattered-field formalism.

One of the most studied type of MNPs are spherical particles. As a result, LSP resonances can be throughly described by Mie theory, an analytical and complete theory of light scattering by spherical particles. Postulated in 1908 by Gustav Mie,

the theory describes the scattered fields as a superposition of different multipolar harmonics. For small particles, these excitations are primarily dipolar [22]. A numerical example of a dipole-like LSP resonance at a spherical MNP is provided in Fig. 2.12; the Drude particle with a 25 nm radius is excited at a 347 nm wavelength, which is close to the resonance condition.

### *2.4.1 Quasi-static approximation and nanoparticle polarizability*

While the Mie theory offers a complete solution to the scattering problem, a simpler and effective approach can be taken through the *quasi-static approximation* to understand the resonant properties of MNPs. This approximation is valid for particle dimensions that are much smaller than the wavelength of the incident light. In this case, oscillating electric field along the particle is effectively constant. From the ensuing electrostatic calculations, approximate dynamic response of the particle can be obtained by simply introducing a time-dependence to the resulting static term [22]. A test case involving a spherical MNP with a radius $a$ is given in Fig. 2.13. The dielectric constants of the sphere and the surrounding medium are represented by $\varepsilon_m$ and $\varepsilon_b$, respectively. The sphere is subjected to a static electric field $E_0$ along the $z$-axis, which can be related with the scalar electric potential $\Phi$ ($\mathbf{E} = -\nabla\Phi$).

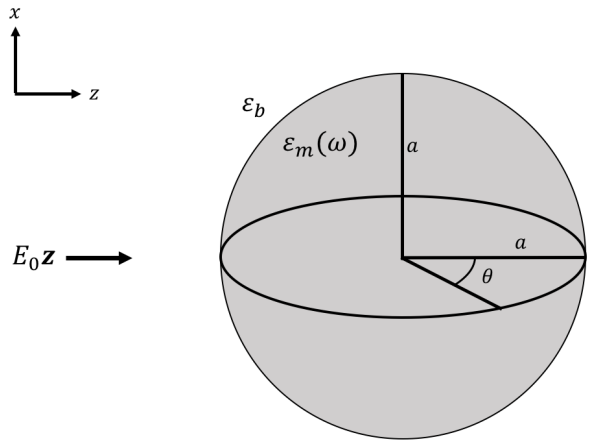


Figure 2.13: A spherical MNP of radius $a$ in an uniform electrostatic field along the z-axis. Azimuthal symmetry is assumed. $\varepsilon_b$ and $\varepsilon_m(\omega)$ denote the background and metal relative permittivities, with the latter being frequency-dependent.

Unlike the rigorous treatment of spherical MNPs via the Mie theory, the quasi-static approximation involves the solution of Laplace's equation ($\nabla^2\Phi = 0$) in spherical coordinates,

$$\frac{1}{r^2 sin\theta}\left[sin\theta\frac{\partial}{\partial r}(r^2\frac{\partial}{\partial r}) + \frac{\partial}{\partial\theta}(sin\theta\frac{\partial}{\partial\theta}) + \frac{1}{sin\theta}\frac{\partial^2}{\partial\phi^2}\right]\Phi(r,\theta,\phi) = 0 \tag{2.46}$$

which is relatively easier and more straightforward to solve for the electric potential [53]. Using the azimuthal symmetry of the geometry, Fig. 2.13, the $\phi$ variations in Laplace's equation can be discarded (at any fixed $r$ and $\theta$, there will be no $\phi$ variation of the potential), resulting in a general solution that is independent of $\phi$ and is written in terms of the orthogonal series of Legendre polynomials inside and outside of the sphere as follows [53]:

$$\Phi_{\text{in}} = \sum_{l=0}^{\infty} A_l r^l P_l(cos\theta) \quad r < a \quad (inside) \tag{2.47}$$

$$\Phi_{\text{out}} = \sum_{l=0}^{\infty} \left[B_l r^l + C_l r^{-l-1}\right] P_l(cos\theta) \quad r > a \quad (outside) \tag{2.48}$$

where $P_l(cos\theta)$ is the $l$th-order Legendre polynomial and $\theta$ is the polar angle. The associated coefficients $A_l$, $B_l$ and $C_l$ can be recovered from the appropriate boundary conditions at $r = a$; namely, continuity of the tangential electric field $E_\theta$ ($=\partial\Phi/\partial\theta$) and the normal component of the displacement vector $D_r$ ($=\varepsilon\partial\Phi/\partial r$). As a result, the potentials are obtained as [22, 53]:

$$\Phi_{\text{in}} = -\frac{3\varepsilon_b}{\varepsilon_m(\omega) + \varepsilon_b} E_0 r cos\theta \tag{2.49}$$

$$\begin{aligned}\Phi_{\text{out}} &= -E_0 r cos\theta + \frac{\varepsilon_m(\omega) - \varepsilon_b}{\varepsilon_m(\omega) + 2\varepsilon_b} E_0 \frac{a^3}{r^2} cos\theta \\ &= -E_0 r cos\theta + \frac{\mathbf{p}\cdot\mathbf{r}}{4\pi\varepsilon_0\varepsilon_b r^3}\end{aligned} \tag{2.50}$$

where $\mathbf{p}$ ($= \epsilon_0\epsilon_b\alpha\mathbf{E}$) is the induced dipole moment in the sphere by the external field and can be explicitly written as

$$\mathbf{p} = 4\pi\varepsilon_0\varepsilon_b a^3 \frac{\varepsilon_m(\omega) - \varepsilon_b}{\varepsilon_m(\omega) + 2\varepsilon_b}\mathbf{E}_0 \tag{2.51}$$

Based on this expression, the frequency-dependent polarizability $\alpha(\omega)$ of the spherical particle can be deduced as

$$\alpha(\omega) = 4\pi a^3 \frac{\varepsilon_m(\omega) - \varepsilon_b}{\varepsilon_m(\omega) + 2\varepsilon_b} \tag{2.52}$$

which is known as the *Clausius-Mossotti relation*. This relationship showcases the resonant behaviour of the polarizability, where the denominator becomes zero:

$$Re[\varepsilon_m(\omega)] = -2\varepsilon_b \tag{2.53}$$

This is known as the *Fröhlich condition*, and denotes the LSP resonances as well as the associated field enhancements. Note that, for Drude metals that have negligible damping and are suspended in vacuum ($\epsilon_\infty = \epsilon_b = 1$), the Fröhlich frequency roughly corresponds to $\omega_p/\sqrt{3}$, with $\omega_p$ being the plasma frequency [22].

Alternative polarizability descriptions for different particle dimensions and morphologies are also present in the optics literature. For a generalized spherical particle, lowest-order electric dipolar coefficient from the Mie solution can be used to denote the dipole polarizability [54], as long as the dipolar approximation holds. The polarizability can be thus written as:

$$\alpha = i\frac{3a^3}{2x^3}\frac{m\psi_1(mx)\psi_1'(x) - \psi_1(x)\psi_1'(mx)}{m\psi_1(mx)\xi_1'(x) - \xi_1(x)\psi_1'(mx)} \tag{2.54}$$

where $m$ and $x$ correspond to normalized refractive index of the sphere and the size parameter ($x = 2\pi a/\lambda_0$), respectively. The terms $\psi$ and $\xi$ correspond to Ricatti-Bessel functions. Similar polarizability descriptions have also been expanded for prolate and oblate spheroidal particles [55].

Dipolar nature of the excitation brings out the issue of radiation damping, which should be accounted for at the polarizability. The polarizability with the correction term can thus be written as [56]:

$$\alpha_r(\omega) = \left[\left(4\pi a^3\frac{\varepsilon_m(\omega) - \varepsilon_b}{\varepsilon_m(\omega) + 2\varepsilon_b}\right)^{-1} - i\frac{\omega^3}{6\pi\varepsilon_0 c^3}\right]^{-1} \tag{2.55}$$

The radiation damping effect can be further corrected by the introduction of an appropriate dyadic term [57].

### *2.4.2 Plasmonic nanochains*

While LSPs are inherently localized phenomena, they can give rise to certain guided wave modes if resonant intercoupling is present. The waveguides that consist of

intercoupled linear MNPs are known as plasmonic nanochains. Dominantly dipolar nature of LSPs is pivotal in modeling modal interactions in such structures, as the electromagnetic response of the arrays can be approximated as interdependent Hertzian dipoles [58, 56, 59]. This is often referred as *coupled dipole model* or *discrete-dipole approximation* (DDA), a widely used computational technique in light scattering calculations [60]. A scheme for a plasmonic nanochain and its DDA model is provided on Fig. 2.14.

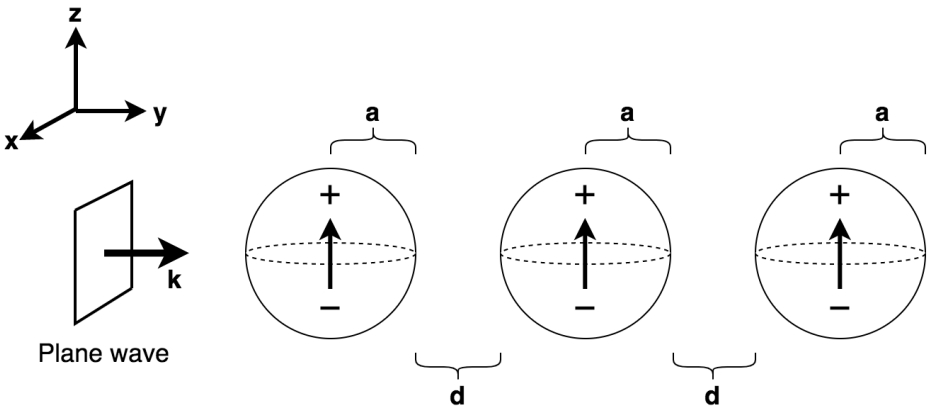


Figure 2.14: Discrete-dipole approximation of coupled plasmonic excitations in a linear array of three MNPs that are stacked on $y$-axis. MNPs are modeled as metallic nanospheres with a radius of $a$ and a separation of $d$. The source of excitation is a $z$-polarized plane wave that is moving along the $y$-direction, hence resulting in dipolar components with the same polarization.

Nevertheless, it should be noted that single dipole approximation of a MNP fails for closer nanochain spacings, as the higher-order Mie multipoles gain significant weight within near-field. One of the primary considerations is the size of the modeled MNPs, which should be considerably smaller than the incident wavelength [61]. Park and Stroud have also noted that the dipolar approximation sufficiently holds for $a \leq d/3$; $a$ and $d$ refer to the radius of the MNP and the center-to-center interparticle spacing, respectively [62].

Compared to the analysis in planar media, dispersion relation in nanochains requires a more stringent modal treatment, since these structures are able to support transverse and longitudinal polarizations with respect to the propagation direction.

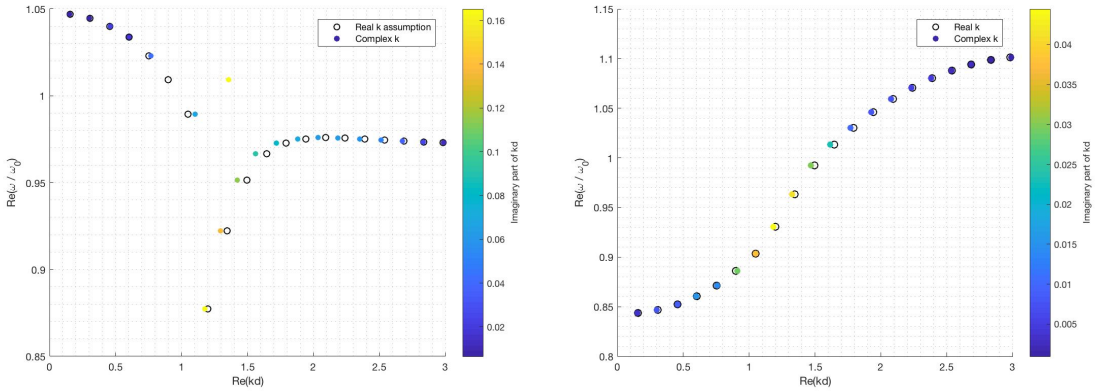


(a) Transverse excitation

(b) Longitudinal excitation

Figure 2.15: Complex dispersion relations for a plasmonic nanochain with 20 spherical nanoparticles for transverse *(left)* and longitudinal excitations *(right)*. The particles have a radius of $a = 25$ nm and an interparticle spacing of $a = 75$ nm. The Drude parameters are $\varepsilon_\infty = 1$, $\omega_p = 9.3891e15$ rad/sec and $\nu = 1.0635e15$ rad/sec. The colorbar shows the imaginary part of the complex wavenumber; the empty circles denote the purely real wavenumber limit for infinite nanochains.

In addition, modes of finite and infinite structures necessitate different analytical and numerical approaches [56]. The discussion on complex dispersion also persists for nanochains; while complex $\beta$ solutions raise divergence issues in infinite chains, these can be realized physically in a finite system [63]. Complex $\beta - \omega$ pairs for such a structure is provided on Figs. 2.15a and 2.15b to illustrate the peculiarities; system in question consists of 20 equally spaced Drude metals with a radius of 25 nm and an interparticle spacing of 75 nm. The relevant calculations based on Weber and Ford's analysis [56], as well as the details on DDA, are provided on Appendix A.

## *2.5 Conclusion and summary*

Plasmonics studies the interaction of electromagnetic waves and plasma oscillations at dielectric and metal interfaces. In this chapter, foundations of plasmonics is covered. Electromagnetics of layered media is constructed step-by-step from the Maxwell equations: two orthogonal solutions in stratified media, TE and TM waves,

are derived. The importance of TM solutions in plasmonics is highlighted. Reflection of such waves, as well as the optical properties of metals, are reviewed. SPPs, guided plasmon modes which exist at planarly layered media, are introduced for different cardinal structures. Another type of plasmonic interactions, LSPs in metal nanoparticles, are also briefly covered.

# Chapter 3

# SURFACE PLASMON POLARITON REFLECTION FROM ABRUPT TERMINATIONS

With the advent of miniaturization trend in electronics and photonics, plasmonic structures offer a breath of fresh air compared to their bulkier counterparts in more conventional guided-wave optics [11, 64, 46]. With the potential of plasmonics, there exist challenges to be resolved, such as, presence of variety of discontinuities like bends, terminations and perhaps defects (dents or protrusions) in these tightly-packed, integrated or discrete systems. In order to develop an efficient design process based on or using plasmonics, it is necessary to deduce how guided waves respond to such discontinuities that may be intentional or non-intentional parts of the system to be designed. In the 20th-century, similar problems for waveguides and transmission lines that are commonly used in microwave and antenna applications were extensively studied and modeled, in order for them to be utilized in microwave integrated circuit applications. Since different applications required different levels of accuracy, the models that were developed ranged from crude and approximate models to very accurate and computationally expensive ones. If plasmonics is expected to find many applications in integrated optics, it needs to go through a similar phase of development of models, for which this chapter tries to review the literature and, through numerical experimentations, to provide some basic intuitions on the reflection and transmission of SPPs at some canonical discontinuities such as "*open*" (semi-infinite metal-dielectric waveguide where the termination is free space), "*short*" (semi-infinite metal-dielectric waveguide where the termination is metallic), "*gap*" (metal-dielectric waveguide with finite length infinite depth groove or ridge) and some modifications of these.

Interaction of surface waves with abrupt discontinuities on waveguides is a rather

complex phenomenon, as it involves scattering and diffraction of a guided wave from an edge or wedge of a material. For a single interface SPP waveguide, two canonical discontinuities, as shown in Fig. 3.1, can be treated for the diffraction as a form of Sommerfeld half-plane problem [65], where, however, ensuing near-field interactions and non-negligible material losses essentially limit and complicate its analytical treatment. Moreover, junctions of such discontinuities are subject to tip LSP modes, which can be associated with a field singularities at the corners [66]. This phenomenon is not unique to metals in the optical regime and has been covered extensively in the past studies on electromagnetic interactions in various conducting bodies [67, 68].

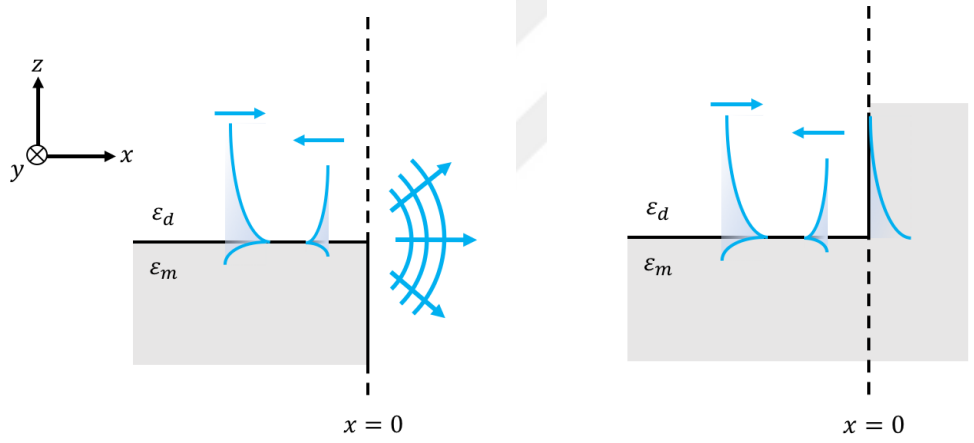


(a) "Open" waveguide termination (b) "Short" waveguide termination

Figure 3.1: Two canonical abrupt discontinuities for SPPs and the phenomenological pictures of diffraction and reflection from *(a)* "open" (dielectric) and *(b)* "short" (metallic) terminations. The vertically-excited SPP modes are not shown.

An exact solution to the wedge diffraction problem, as shown in Fig. 3.1(a) can be obtained from the Sommerfeld-Malyuzhinets theory, which is an extension of Sommerfeld's original solution with more appropriate boundary conditions for finitely conductive surfaces. While this approach has been adapted for SPP scattering from such discontinuities [65, 69], it mainly addresses the radiation from the wedge into the space around the wedge and provides little information on the reflec-

tion or transmission of the surface waves onto the forming surfaces and away from the wedge as surface waves. Another possible approach, originally developed for dielectric slab waveguides, yields convoluted Fredholm integral equations that can only be solved numerically [70, 71]. While these approaches provide some rigorous tools to use for the solution of the problem at hand, they are rather complex and difficult to adapt for different problems. Perhaps more importantly, they are difficult to interpret, build intuitions on and use in a broader sense by engineers in the design of integrated optics, unlike discontinuities in microwave integrated circuits.

In this chapter, reflection of SPPs from waveguide terminations will be characterized through heuristic and semi-analytical methods. The first section will introduce the methodology and full-wave analysis tools that will be employed to assess the validity of these approaches: in addition, two possible techniques for extraction of the reflection and transmission coefficients will be assessed. The succeeding section will comparatively cover the approximate and semi-analytical methods for characterization of the "open" and "short" waveguide terminations; these techniques will pave the paths for the analysis of more intricate discontinuities. The final section will assess the reflection and tunneling behaviour of infinite plasmonic barriers through an extension of the developed termination models within a Fabry-Pérot formalism.

It should be noted that in addition to reflection, transmission of SPPs at the half-plane discontinuity ("side-coupling") is also an open problem. While there are different semi-analytical and numerical studies on SPP generation at slit end-faces [72, 73, 74], these models do not provide sufficient tools to develop a complete expression for SPP side-coupling with reasonable magnitude and phase terms. Hence, the discussion of SPP transmission at these edge discontinuities will not be featured.

### *3.1 Numerical methods and FDTD analysis*

Since most of the problems in electrodynamics, particularly those pertaining to nanophotonics, do not have closed-form analytical solutions, we are bound to use one of the full-wave algorithms that are available commercially. So, to set the stage

properly, a preliminary discussion on the numerical EM tools is provided here very briefly. Although there are many EM-based methods that have been developed and employed in the analysis of such problems, for the problems in optics, a vast majority of researchers have used and been using finite-difference time-domain (FDTD) and finite element (FEM) methods [15]. Alternative methods including method of moments (MoM) [75], multiple multipole method (MMP) [76] and Green's tensor approach [77, 78], have been used for some specific problems or geometries, where they could have computational advantage over the other methods. In this thesis, the FDTD method, via Lumerical's FDTD Solutions software [79], has been employed as the primary full-wave analysis method. First proposed by Kane S. Yee in 1966 [80], and developed further with the advent of computers and the computational power, this method enables the extraction of wideband transient and steady-state responses of an electromagnetic system. Therefore, it has become the method of choice for many photonic applications, including the study of reflection and transmission of SPPs in this work. A comprehensive review of the FDTD method and the Yee algorithm can be found in Taflove and Hagness's seminal textbook [81].

### *3.1.1 Notes on implementation of FDTD*

Although most practical discontinuities are three dimensional, understanding and modeling reflection and transmission from their 2D versions would be sufficient to build intuitions and perhaps to construct equivalent circuit models, with an added advantage of computational efficiency. Therefore, during this study, all discontinuities are assumed to be 2D, with their wedges uniform and extend to infinity in one dimension ($y$-direction, except otherwise stated), and the incident SPPs are assumed to be propagating normally to the discontinuity ($x$-direction, except otherwise stated). It should also be pointed out that Lumerical FDTD by convention sets the 2D simulation region normal to the $z$-axis, which contradicts with the aforementioned formulation that is assumed for the overalanalysis: during the simulation setup and data processing, the following coordinate transformations along the $x$-axis were employed to maintain consistency between the semi-analytical calculations and

simulation data:

$$\begin{aligned}(x', y', z') &\rightarrow (x, z, -y)\\ E'_x &\rightarrow E_x\\ E'_y &\rightarrow E_z\\ H'_z &\rightarrow -H_y\end{aligned} \tag{3.1}$$

where the prime and non-prime coordinates denote the FDTD and assumed conventions, respectively.

Once the main features of the geometries are decided, implementation of FDTD requires some additional fixes, like the stability factor and absorbing boundaries around the geometry to be simulated, which are chosen to be 0.99 to satisfy the Courant– Friedrichs–Lewy condition and the perfectly matched layer (PML) boundary condition, respectively. Moreover, Lumerical's conformal variant 0 mesh setting is applied to all simulations; this option applies an adaptive mesh to the dielectric regions in the simulation region. Even though the highest mesh settings are used, a mesh override region with a 2.5 nm-sized uniform grid is placed around the discontinuity, with a buffer region of 10 nm around the structure. The simulations are terminated after most of the fields inside the simulation region are absorbed by the PMLs, which is achieved through the built-in automatic-shutoff option.

Throughout this study, we have chosen 101 equally-spaced wavelengths over a range of wavelength between 500 nm and 1000 nm in every simulation, where SPPs exhibit suitable confinement properties and are used extensively. Regarding the materials used in the SPP waveguides, silver and gold are chosen in general as substrates, modeled as Drude materials with the following parameters obtained through a simplex fit to the experimental data by Babar and Weaver in the frequency range of interest [31]: for silver, $\varepsilon_\infty = 3.965$, $\omega_p = 1.398844e16$ rad/s and $\nu = 3.624054e13$ rad/s, and for gold, $\varepsilon_\infty = 1$, $\omega_p = 1.299e16$ rad/s and $\nu = 2.7954e13$ rad/s. Even though more intricate alternatives to the Drude materials are present, as reviewed in section 2.2, this model is relatively simple and efficient for proof of concept calculations in the desired frequencies, where interband transition effects are relatively low. Additionally, dispersion modeling of Drude

materials is well-established in the FDTD literature [81].

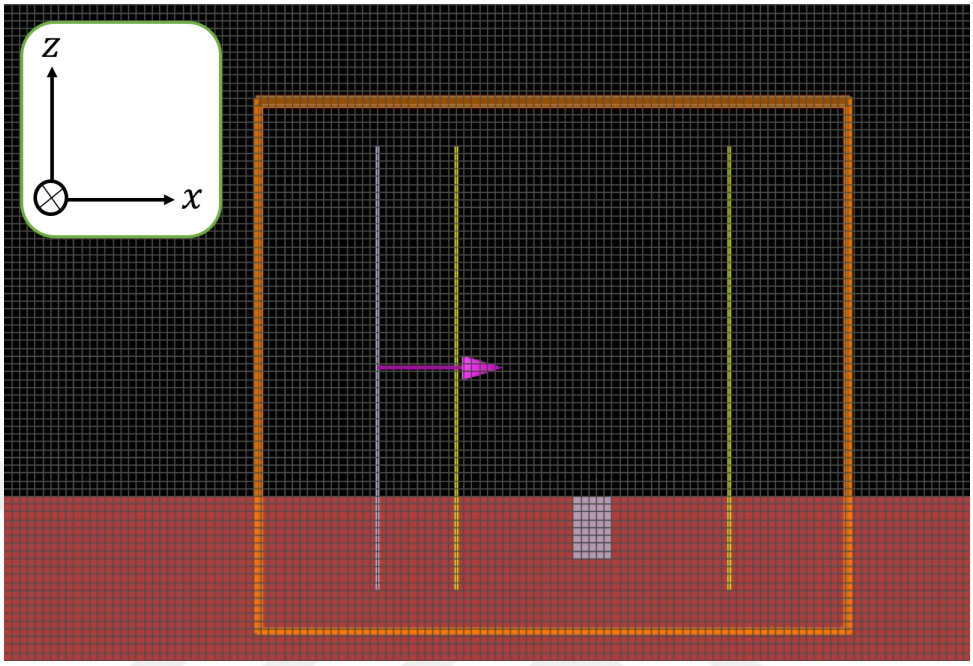


Figure 3.2: A typical Lumerical screenshot for a groove simulation with an excitation (gray line) and two frequency-domain monitor (yellow line) planes. The grids do not represent the Yee cells.

### *3.1.2 Modal sources and monitors*

In order to simulate SPP propagation, reflection and transmission at planar interfaces as accurately as possible, appropriate excitation model should be chosen from a few available sources like plane wave, dipole or mode source. Since plane waves can not excite SPPs at planar interfaces due to momentum mismatch (propagation constant $k$ of plane waves do not match $\beta$ of SPPs), they are not suitable for this problem. Dipolar sources like vertical electric dipole are able to excite SPPs along planar interfaces and have been used for the analysis of MIM structures [40]. However, since it also excites all sorts of other space waves around the interface, it makes it difficult to sort out the SPP modes and, in turn, to find the reflected and transmitted SPP waves. Based on this brief comparison of the possible excitations of SPPs with a view of tracking the incident, reflected and transmitted SPPs, the most straightforward option would be the mode source. A mode source is commonly used

for injecting the eigenmode supported by the cross-section of a waveguide, which is, in this case, a planar interface between a metal and dielectric half spaces.

Mode source is placed transverse to the direction of propagation and, in general, at the center of the waveguide (extending in both regions equally). However, in the case of SPP propagation along the interface, it is slightly offset towards the dielectric region as SPPs penetrate into the dielectric region more than they penetrate into the metal region. There are multiple options to characterize waveguide modes in Lumerical. One of these is the built-in finite-difference eigenmode solver [82], which extracts the approximate propagation constants and the mode profiles through enforcing pre-designated boundary conditions at the corners. For guided modes with evanescent components, such as SPPs or fiber optic modes, perfect electric conductor (PEC) or PML conditions can be enforced at the boundaries. For SPPs, source boundaries should be extended sufficiently to ensure that the fields decay almost completely. Since such mode solvers often involve eigenvalue equations with large matrices and should be run for each frequency point [83], they tend to be computationally expensive.

Another option is to use a custom spatial source profile, using the explicit expressions for the SPP field profiles at a cross section of the waveguide, as detailed in Section 2.3.1. This approach is relatively straightforward and mode profiles are calculated before the start of the simulation runs. As stated earlier, in the simulations provided in this work, the source and monitor boundaries have been extended well into the dielectric (3.5 $\mu m$ above the interface) to capture the large portion of the SPP profiles in the dielectric.

The spectrum of the source pulse (Fig. 3.3a) is modeled as a Gaussian function that is centered in the middle of the frequency band, as can be seen in Fig. 3.3b. Using the frequency-domain monitors and built-in Fast-Fourier transform subroutine, the steady-state field distributions for each frequency point at each grid on the monitor is extracted [79]. These time-harmonic data are processed through mode expansion monitors, which will be discussed in the next subsection.

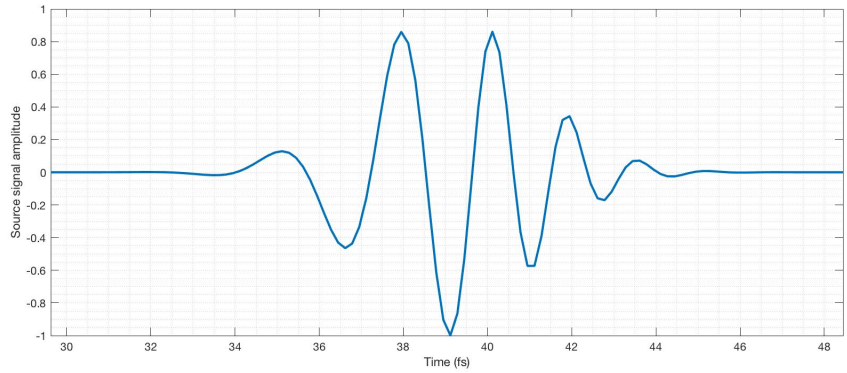


(a) Time-domain source signal

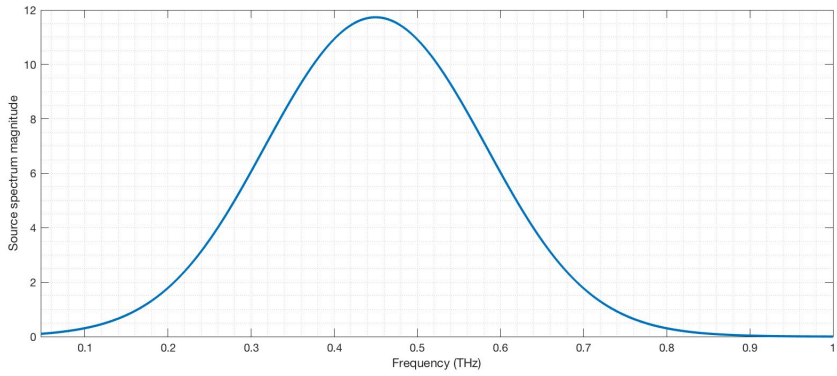


(b) Source signal magnitude spectrum

Figure 3.3: Time- and frequency-domain representation of the FDTD source signal

### *3.1.3 Mode and network analysis*

As a prerequisite for this study, a concrete definition of reflection and transmission coefficients is necessary. Unlike incident uniform plane waves in layered media where reflection and transmission coefficients are well-defined for both perpendicular and parallel polarizations, it is not the case for SPPs when they encounter a discontinuity. Because, at the discontinuity, incident SPPs give rise to not only the reflected and/or transmitted SPPs but also to other waves (evanescent and/or propagating) due to diffraction and scattering. Therefore, there is no unique definition of reflection and transmission coefficients in this problem. However, since a metallo-dielectric interface can only support SPPs, no matter what happens at the vicinity of discontinuity, they will be the only modes to exist away from the dis-

continuity, be it as reflection and/or as transmission, depending upon the geometry. So, one can define reflection and transmission based on a single field component in the SPP, as in the case of uniform plane wave incidence with $s$- or $p$-polarization in a layered medium. As a result, the reflection coefficient in this work and in the literature is defined as referenced to the perpendicular electric field component to the interface and to the direction of propagation, $E_z$ in Fig. 3.1. The choice of this field component as a reference is mainly because it is the defining and dominant field component in SPPs at metallo-dielectric interfaces.

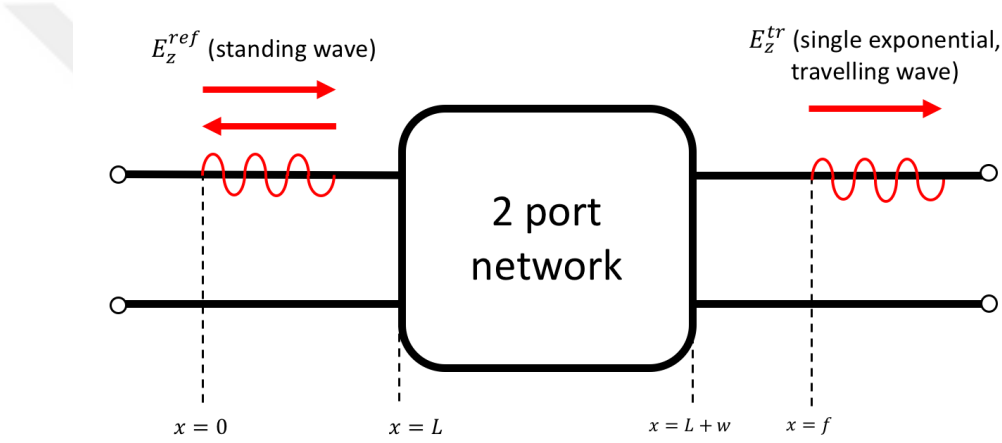


Figure 3.4: 2-port network model for discontinuities. Note that input and output ports are chosen a few wavelength away from the physical location of the discontinuity; $x = 0$ for incident and reflected waves, and $x = f$ for transmitted waves.

Motivated by the ultimate goal of modeling discontinuities for SPPs, discontinuities are considered as two-port networks with transmission line interconnects before and after, as shown in Fig. 3.4. In this schematic, the modal expansion is performed at the points $x = 0$ and $x = f$ for reflection and transmission, respectively. As for an ordinary transmission line, the total field at the input port is written as a linear combination of incident and reflected waves that form a standing wave, while only the transmitted wave is assumed to exist at the output port. Correspondingly, the total field at the field monitors at $x = 0$ and $x = f$ can be written as

$$E_z^{\text{monitor}}(x = 0) = a_i E_z^{SPP+} + a_r E_z^{SPP-} + E_z^{rad} \tag{3.2}$$

$$E_z^{\text{monitor}}(x=f) = a_t E_z^{SPP+} + E_z^{rad} \tag{3.3}$$

where $a_i$, $a_r$ and $a_t$ are the complex coefficients of the incident, reflected and transmitted waves, respectively, and $E_z^{rad}$ represents the radiated fields that are caused by the scattering off the discontinuity. Since the field representations in Eqs. (3.2) and (3.3) are at the monitor sites ($x = 0$ and $x = f$), i.e., away from the physical discontinuity, the ratios $a_r/a_i$ and $a_t/a_i$ give the reflection and transmission coefficients defined at $x = 0$ and at $x = f$, respectively, that is, not at the site of the discontinuity at $x = L$ and $x = L + w$, Fig. 3.4. Consequently, one needs to extract the response of the discontinuity from this information. In other words, the ratios $a_r/a_i$ and $a_t/a_i$ at the port locations ($x = 0$ and $x = f$) need to be transferred to the physical locations of the discontinuity at $x = L$ and $x = L + \text{w}$, referred to as de-embedding in microwave circuit terminology [17]. This yields the basic recipe for the reflection and transmission coefficients:

$$S_{11} = \Gamma = \frac{a_r}{a_i e^{i\beta_{\text{SPP}} 2L}} \tag{3.4}$$

$$S_{21} = t = \frac{a_t}{a_i e^{i\beta_{\text{SPP}}(f-\text{w})}} \tag{3.5}$$

Once the recipe is fixed, the only remaining step is to find the coefficients accurately in Eqs. (3.2) and (3.3), as the accuracy of the reflection and transmission coefficients depends on them. As stated earlier, the fields measured at the terminal planes consist of not only the sought after surface plasmon waves (SPPs) but also other modes generated by the discontinuity, including some intermodal transfers. That is, scattered and diffracted waves from the discontinuity surely give rise to radiated and evanescent waves at the terminals and make it difficult to extract the SPP modes to get their coefficients. There seems to be two practical approaches that we could use: i) exponential approximation of the field before and after the discontinuity, ii) eigenmode expansion analysis, both of which have been introduced, implemented and compared throughout the study.

For the exponential approximation of scattering parameters, there are mainly two algorithms: Prony's method and generalized pencil-of-function (GPOF) method. Since studies demonstrated that Prony's method is quite sensitive to numerical noise

in the system, GPOF method has been considered as one of the primary candidates for modal analysis of SPPs in this study. The technique was introduced to EM and signal processing communities for the efficient approximation of discrete signals with a finite number of complex exponentials in the form [84]:

$$y(n\Delta t) = \sum_{k=1}^{M} R_k e^{s_k n \Delta t} \tag{3.6}$$

where $\Delta t$, $R_k$ and $s_k$ are the sampling interval, complex residue and complex pole, respectively. Modal analysis by exponential approximation works only because SPPs in planar 2D interfaces are exponential in nature. For the geometry of interest, as modeled in Fig. 3.4, the standing wave at the input port and the transmitted wave at the output are composed of exponentials, two for the former and one for the latter. With presence of other modes due to the scattering from the discontinuity, one needs to use more exponentials, from which the ones that correspond to the SPPs are selected as the closest to $k_{\mathrm{SPP}}$ among $s_k$'s in Eq. (3.6).

For the sake of illustration, a typical sampling scheme for this analysis is shown in Fig. 3.5, where the monitor is placed at least a few wavelengths away from the source (2 $\mu m$) and slightly buried in metal layer, as shown as a yellow line in Fig. 3.5. This placement aims to minimize interference from non-SPP field components; the distance from the discontinuity would help near-field scattered components to die off and the depth from the surface into metal would guarantee the sampling of SPPs while further avoiding the radiation modes. In addition, a uniform mesh-override is placed around the monitor, since GPOF method requires uniform sampling of the signal to be approximated. Considering that simulations of such geometries are time consuming and computationally expensive, and the same data may be needed for future studies either by the author or other researchers, the steady-state field distributions for all wavelengths and simulations are stored in a cloud-based data repository.

The second approach, eigenmode expansion analysis (EME), is based on the mode orthogonality condition, which states that a transverse field distribution on a waveguide can be dissected into an orthogonal set of the discrete guided waves and continuum of radiation modes [37, 85]. In its most general form, it can be

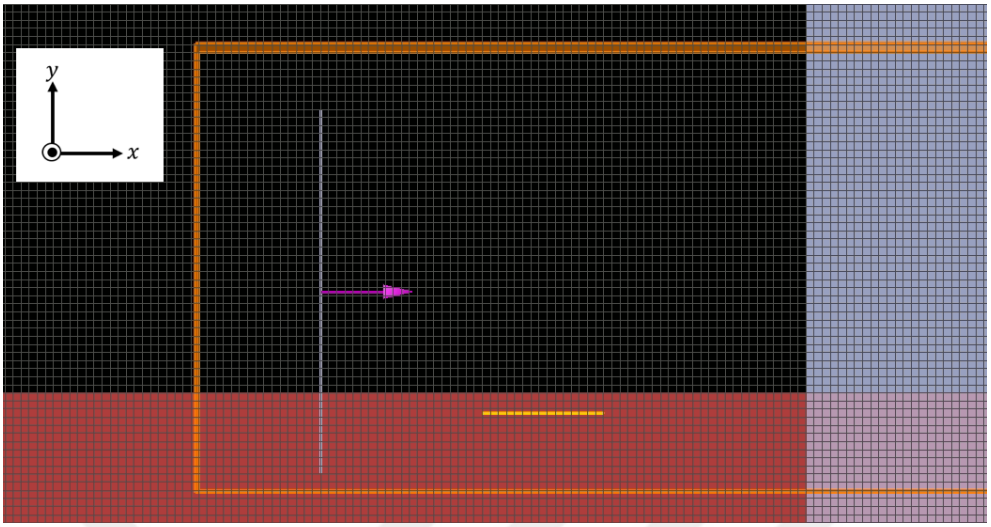


Figure 3.5: A typical GPOF sampling scheme for the simulations, where the horizontal yellow line denotes the sampling monitor. The depth of the monitor in metal is exaggerated for illustrative purpose.

represented as:

$$\iint_S \Psi_i \Psi_j dS = 0, \quad i \neq j \tag{3.7}$$

where $\Psi$ is the mode function and the subscripts denote the mode numbers. The integration is performed on the surface that is transverse to the direction of propagation; for 2D structures, it would take on the form of a line integral. Based on this identity, overlap integral expressions for complex amplitudes of a specified forward and backward mode can be defined. A general discussion on the mode orthogonality condition and the derivation of expansion coefficients are provided in Appendix B.

In Lumerical, EME is performed numerically through built-in functionalities. One approach is using a mode expansion monitor, which obtains the modes on a transverse cross section and calculates the overlap integrals from frequency-domain monitor data. Nevertheless, as for the built-in mode source, this operation is computationally expensive and performed at each simulation run for each frequency point, due to the presence of adaptive Yee meshes. Furthermore, this approach does not permit unconjugate expansions of the mode profile. A possible way to circumvent this is using frequency-domain monitors alone and calculating the mode overlaps with the readily-available custom source profiles: this is possible through the built-

in unconjugate expansion function ("expand2") in the Lumerical scripting language. This particular approach is adapted in this thesis for EME analyses.

A scheme for EME analysis of SPP reflection from a waveguide discontinuity is provided in Fig. 3.6. The steady-state field distributions are recorded on two different frequency-domain monitors at $x = 0$ and $x = d$. The monitored field data is expanded with respect to the pre-calculated SPP mode distribution; this yields the complex amplitudes for forward and backward waves at each ports. At the second port, where transmission is recorded, a small backward wave may be present due to possible reflections from the PML; these can be treated as a low-level numerical noise.

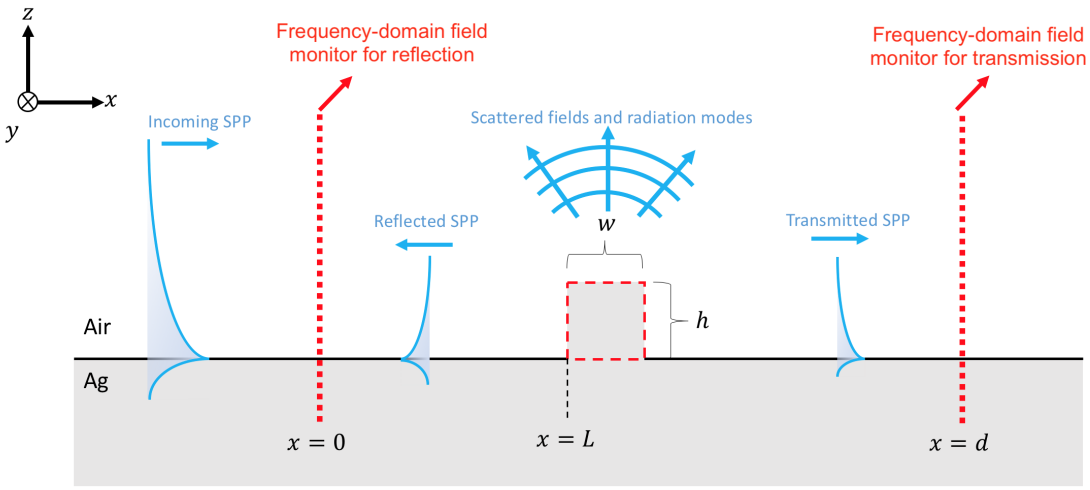


Figure 3.6: A typical surface discontinuity and the FDTD simulation schematic with source and monitor setup for the EME. The discontinuity is modeled as a ridge structure with a width of $w$ and a height of $h$. The frequency-domain field monitors (red-dotted lines) are located at $x = 0$ and $x = d$ for reflection and transmission calculation, respectively.

### *3.1.4 Performance of EME and GPOF methods*

Performance of EME and GPOF methods can be assessed through a simple test case, for which its solution is known. However, most problems with discontinuities on layered and lossy media, even ones with simple discontinuities like open terminations,

have no closed-form analytical solutions to compare and assess the performances of these two approaches. A basic numerical experiment can be constructed through inserting a hypothetical PEC discontinuity to the simulation region, as in Fig. 3.7, which is expected to yield an approximately unitary reflection coefficient with an relatively stationary phase of 180°. This can simply be achieved through changing the rightmost boundary from PML to PEC. In order to eliminate possible spurious radiation due to the source injection, both EME and GPOF monitors are located at 8 $\mu m$ away from the source. For the GPOF implementation, the length of the GPOF monitor over which the field is sampled is chosen 2 $\mu m$, a few multiple of the wavelengths in order to capture the field profile sufficiently accurate; this length covers twice the largest effective SPP wavelength ($\lambda_{\mathrm{SPP}} = 2/Re[\beta_{\mathrm{SPP}}]$.) Moreover, the GPOF monitor is positioned 5 $nm$ below the interface in a uniform mesh of 2.5 $nm$, and at least two exponentials are used in the GPOF fit, one for the incident and one for the reflected waves.

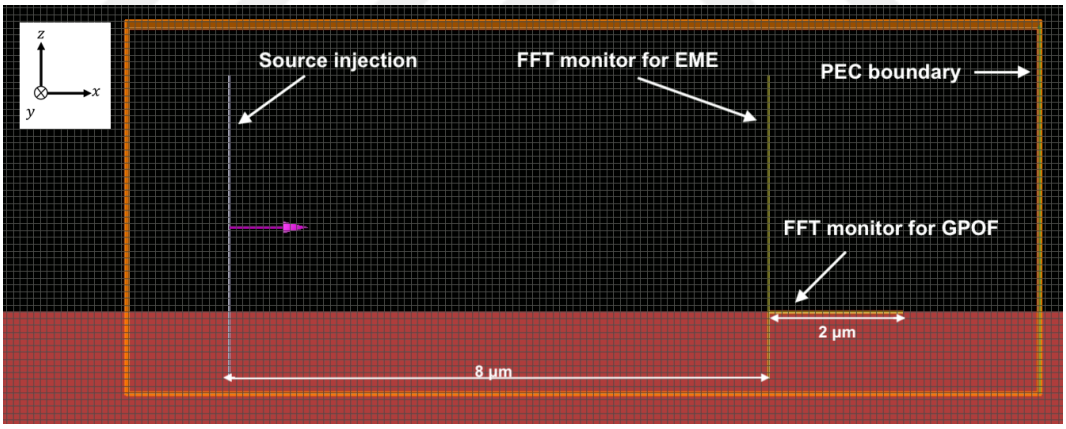


Figure 3.7: The geometry of a metal-dielectric waveguide with PEC termination; a test case for the EME and GPOF methods.

With careful implementation of both methods, the reflection coefficient data have been obtained and provided in Fig 3.8, with two exponentials in the GPOF method. Even though minor deviations and ripples are expected due to numerical noise, the GPOF results showcased increasing deviation from the EME results for longer wavelengths, particularly starting from 750 $nm$. Increasing the number of exponentials did not improve the performance of the GPOF; in contrary, it was

shown to dramatically aggravate the ripples, particularly at different wavelengths. In addition to the reflection coefficient, the propagation constant $k_{SPP}$ that has

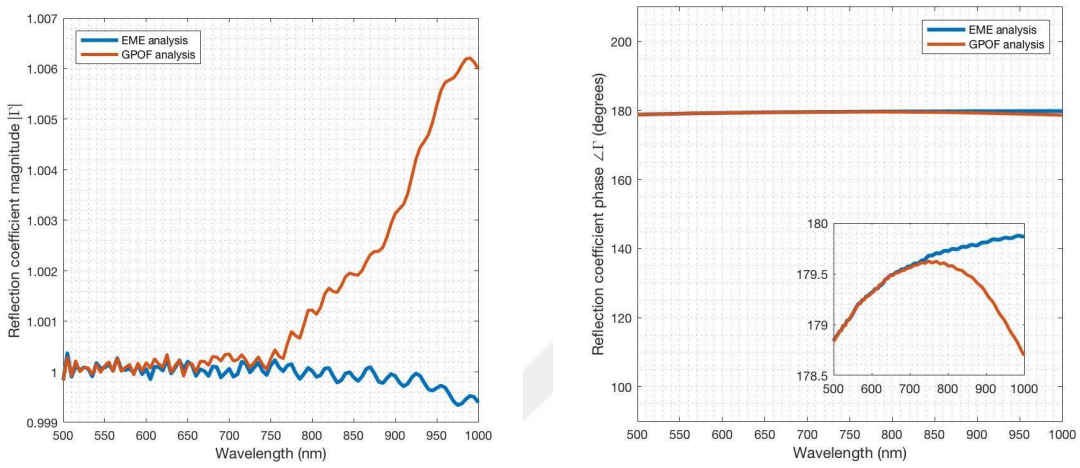


(a) Reflection coefficient magnitude vs. free-space wavelength

(b) Reflection coefficient phase vs. free-space wavelength

Figure 3.8: Comparison of the reflection coefficient magnitude *(a)* and phase *(b)* for the test case in Fig. 3.7

also been obtained from the GPOF analyses are compared with its analytical values from the dispersion relation in Fig. 3.9. While the real part of the propagation constant is compatible with the analytical result, the imaginary part deviates from the analytical curve starting at 700 nm. Around 900 nm, it becomes negative, corresponding to unphysical, growing field.

The distortion in wavevector pole at the general GPOF analysis of FDTD data can be attributed to the presence of so-called *"quasi-cylindrical"* or *"creeping wave"* components, which are possible byproducts of the scattering and diffraction events in layered plasmonic media [86, 87]. In the aforementioned test case, these components can be introduced through the spurious fields that may emanate from the source-like field singularity at the junction between metallo-dielectric layer and PEC. Being fundamentally distinct from the surface wave modes, these waves showcase an algebraic decay of $x^{-1/2}$ in the vicinity of the scatterer for 2D structures, hence the name quasi-cylindrical wave (QCW). This algebraic dependence translates to

a much rapid decay in comparison with the lossy SPP modes. Their asymptotic behavior in the far-field is much different, with algebraic dependence of $x^{-3/2}$; thus, they are often analogized with Norton surface waves in this regime [88]. In the general study of waves in inhomogenous media, the near- and far-field behavior of waves can be classified into the well-documented class of *space* and *lateral waves*, respectively [24, 89].

The effects of QCWs on the field distributions of plasmonic excitations such as grating coupling or extraordinary optical transmission is well-documented [86, 72]. The effects of these fields are largely dependent on the wavelength and material permittivities; for larger wavelength bands, such as near- and short-wavelength infrared, dominance of lateral excitations over SPPs are more pronounced, even over an order of magnitude of the free-space wavelength [86, 88]. Strongly-algebraic terms that stem from lateral wave components are the probable cause of the perturbed wavevector results of reflected wave components, since these constitutive terms cannot be cast into a finite number of exponential or plane wave forms. Furthermore, it should be pointed out that at longer wavelengths, SPP wavevector closely approaches to the branch point for air ($k_0$), latter of which is known to influence the lateral wave behavior [89].

Considering possible existence of the spurious fields due to source-like field singularity at the junction between metallo-dielectric layer and PEC, an additional test case may be advisable to define the merits of GPOF method: further assessment of the quasi-cylindrical wave constituents and their effect on this technique can be examined with a test case involving a magnetic line source impressed on the metallo-dielectric interface, as inspired by the approach in [89]; this analysis is provided on Appendix C.

Based on the overall assessments in this section, the EME approach will be employed as the main post-processing method for the rest of this thesis.

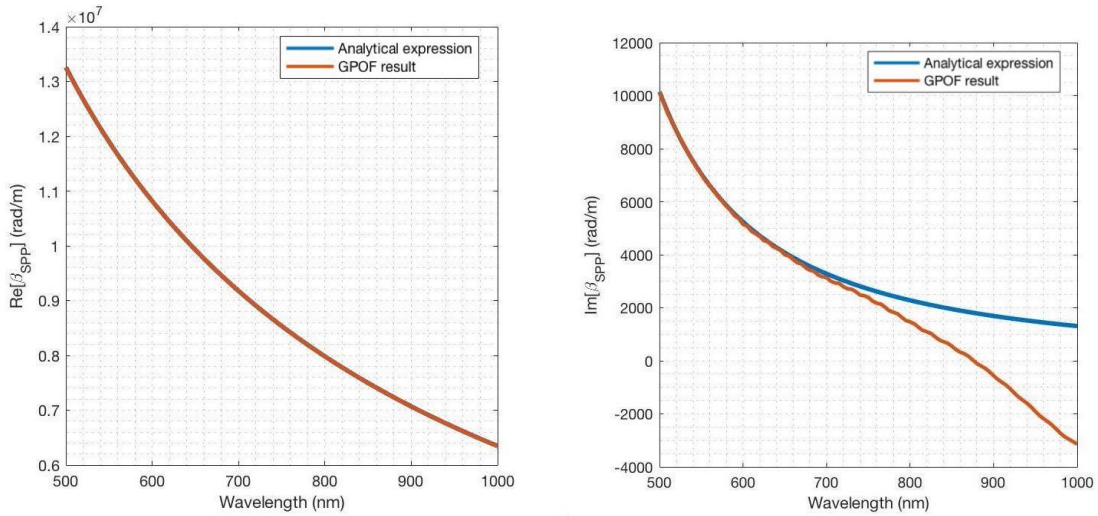


(a) Real part of the SPP wavevector vs. free-space wavelength

(b) Imaginary part of the SPP wavevector vs. free-space wavelength

Figure 3.9: Comparison of $\beta_{\mathrm{SPP}}$ results obtained by GPOF method and analytical expression vs. free-space wavelength $\lambda_0$

## *3.2 Simplified discontinuity models for terminations*

In this section, generalizable models for one-dimensional plasmonic discontinuities with a focus on abrupt waveguide terminations and barriers are introduced and critically reviewed. The basic models cover effective medium theory and vectorial mode-matching techniques. In addition, an approximate technique on the characterization of reflection coefficients, based on the first order impedance boundary condition, is introduced. The main focus of this study is metal-insulator waveguides with two types of abrupt discontinuities, namely open and short, as shown in Fig. 3.1. However, in a few places, MIM waveguides are briefly considered, and a few variations of open and short discontinuities, like finite-width open and short, are used in order to better understand either reflection and transmission mechanisms or the models themselves. The applicability and limits of these models are assessed through the FDTD simulations.

### *3.2.1 Effective medium model for reflection*

One of the simpler methods for characterization of SPP reflection from abrupt dielectric discontinuities is the effective dielectric waveguide model, which was used by Zia et al. in contextualizing slab waveguide modes by means of total-internal reflection phenomenon [90]. The model approximates the traveling SPPs as transverse plane waves in an effective medium with an index $n_{\text{eff}}$, characterized by the mode index:

$$n_{\text{eff}} = \frac{\beta_{\text{SPP}}}{k_0} \tag{3.8}$$

Thus, the model reduces down to the ray optics approximation. This approach is not unique to plasmonic structures, and dates back to the early analyses of dielectric waveguides in the 1970s [91]. In nano- and metaphotonics, the method has found applications in the characterization of metamaterials and silicon photonic structures [92, 82]. An alternative derivation for the mode index model can be obtained from the effective medium prescription by G. Shvets; this approach has been used to analyze the negative refraction in IMI waveguides [93]. Noting that the SPP propagates in $x$-direction on a medium planarly layered along the $z$-axis, equivalent expressions for effective electric ($\tilde{\mathbf{E}}$) and magnetic fields ($\tilde{\mathbf{H}}$) on a transverse plane can be written as:

$$\begin{aligned} \tilde{E}_{x,z} &= \int_{-\infty}^{\infty} E_{x,z}^{\text{SPP}} dz \\ \tilde{H}_y &= \int_{-\infty}^{\infty} H_y^{\text{SPP}} dz \end{aligned} \tag{3.9}$$

Based on the assumption that these equivalent fields propagate in an effective uniform medium with a relative permittivity and permeability of $\varepsilon_{\text{SPP}}$ and $\mu_{\text{SPP}}$, the expressions for these parameters can be extracted from the Maxwell's curl equations, Eqs. (2.1b) and (2.1d):

$$\varepsilon_{\text{SPP}} = \frac{\frac{d}{dx}\tilde{H}_y}{-i\omega\varepsilon_0\tilde{E}_z} = \frac{\int_{-\infty}^{\infty} \frac{d}{dx} H_y^{\text{SPP}} dz}{-i\omega\varepsilon_0 \int_{-\infty}^{\infty} E_z^{\text{SPP}} dz} \tag{3.10}$$

$$\mu_{\text{SPP}} = \frac{-\left(\frac{d}{dx}\tilde{E}_z - \frac{d}{dz}\tilde{E}_x\right)}{i\omega\mu_0\tilde{H}_y} = \frac{-\int_{-\infty}^{\infty} \frac{d}{dx} E_z^{\text{SPP}} dz + \int_{-\infty}^{\infty} \frac{d}{dz} E_x^{\text{SPP}} dz}{i\omega\mu_0 \int_{-\infty}^{\infty} H_y^{\text{SPP}} dz} \tag{3.11}$$

The second term on the numerator of Eq. (3.11) is simply the difference of $E_x^{SPP}$ at $z = \infty$ and $z = -\infty$, which is zero as $E_x^{SPP} \to 0$ as $z \to \infty$ due to the radiation condition. The resulting effective index can be written as the square root of the two quantities; through further simplification, we can obtain:

$$\begin{aligned} n_{\text{eff}}^2 &= \varepsilon_{\text{SPP}}\mu_{\text{SPP}} \\ &= \frac{\int_{-\infty}^{\infty} \frac{d}{dx} H_y^{\text{SPP}} dz}{-i\omega\varepsilon_0 \int_{-\infty}^{\infty} E_z^{\text{SPP}} dz} \frac{-\int_{-\infty}^{\infty} \frac{d}{dx} E_z^{\text{SPP}} dz}{i\omega\mu_0 \int_{-\infty}^{\infty} H_y^{\text{SPP}} dz} \\ &= \frac{i\beta \int_{-\infty}^{\infty} H_y^{\text{SPP}} dz}{-i\omega\varepsilon_0 \int_{-\infty}^{\infty} E_z^{\text{SPP}} dz} \frac{-i\beta \int_{-\infty}^{\infty} E_z^{\text{SPP}} dz}{i\omega\mu_0 \int_{-\infty}^{\infty} H_y^{\text{SPP}} dz} \\ &= \frac{\beta^2}{\omega^2\varepsilon_0\mu_0} = \frac{\beta^2}{k_0^2} \end{aligned} \tag{3.12}$$

The primary downsides of this approach are as follows: (i) the TM-polarized nature of the SPPs is ignored, and (ii) the near-field evanescent components that are involved in diffraction phenomena are not accounted for. The peculiarities of the SPP reflection problem that distinguish it from the plane-wave Fresnel relations were noted in the 1980s by Stegeman et al. [94]. Based on these shortcomings of the method, it is likely to fail to deduce the response of a homogeneous dielectric termination. In this case, it would be necessary to use a more comprehensive vectorial reflection model with appropriate boundary conditions.

Nevertheless, the effective medium model is able to approximate the reflection from an abrupt metallic termination, largely due to the finite conductance of the bulk material. As a result, the metallic wall behaves approximately as a reactive impedance surface. Hence, the reflection coefficient can be defined simply by the effective indices:

$$\Gamma_m \approx \frac{n_{\text{eff}} - n_m}{n_{\text{eff}} + n_m} = \frac{\frac{\beta}{k_0} - \sqrt{\varepsilon_m}}{\frac{\beta}{k_0} + \sqrt{\varepsilon_m}} \tag{3.13}$$

### *3.2.2 Vectorial mode-matching method for reflection from a terminated junction*

One of the most classic techniques in analyzing the discontinuities is mode-matching method with a direct application of interface boundary conditions, Eqs. 2.12, along the discontinuity. However, this approach is complicated by the presence of diffracted fields beyond the termination, as well as the backscattered radiation modes in the

waveguide. In the common vectorial approach to this problem for full dielectric terminations, the backscattered fields are eluded by the approximation of SPPs as the dominant mode in the waveguide [45, 95, 96]. Thus, the radiation modes is largely negligible, as long as the termination features the same dielectric substrate as the plasmonic waveguide. As in the analysis of reflection of polarized light, the tangential field on the waveguide along the discontinuity is dissected into the impinging and reflected modal components, while the transmitted field is represented by an angular spectrum of plane waves. In addition to standard interface boundary conditions, continuity of the power flux is also enforced. Originally developed for obliquely-incident surface waves single-interface waveguides [95, 96], this approach has been also extended to dielectric terminations in MIM waveguides [45] and IMI waveguides [97]. In this subsection, the vectorial approach will be explored from the very basics and will be reformulated for metallic terminations.

An explicit expression for the reflection coefficient for the structure on the left side of Fig. 3.1 can be derived. For TM modes, $E_x$, $E_z$ and $H_y$ components of the electromagnetic field are present and the tangential electric and magnetic fields along interface are continuous, if the surface current density is neglected. The plasmon mode in the waveguide ($E^{SP}$) at $x = 0^-$ and diffracted field ($E^{FS}$) at $x = 0^+$ can be represented with the reflection coefficient $\Gamma$:

$$E_z^{MI}(x = 0^-) = (1 + \Gamma)E_z^{SP} = E_z^{FS}(x = 0^+) \tag{3.14}$$

$$H_y^{MI}(x = 0^-) = (1 - \Gamma)H_y^{SP} = H_y^{FS}(x = 0^+) \tag{3.15}$$

Another applicable boundary condition is the $x$-directed power flux ($S_x$) along the discontinuity, which is characterized by the tangential components of the TM waves:

$$\int S_x^{MI}(x = 0^-)dz = \int S_x^{FS}(x = 0^+)dz \tag{3.16}$$

which can be expanded by the time-averaged form:

$$\int E_z^{MI} H_y^{MI^*} dz = \int E_z^{FS}(x = 0^+)H_y^{FS*}(x = 0^+)dz \tag{3.17}$$

Substituting Eqs. (3.14) and (3.15) into Eq. (3.17) results in:

$$(1 + \Gamma)(1 - \Gamma^*) \int_{-\infty}^{\infty} E_z^{SP} H_y^{SP^*} dz = \int_{-\infty}^{\infty} E_z^{FS}(x = 0^+)H_y^{FS^*}(x = 0^+)dz \tag{3.18}$$

At the discontinuity ($x = 0$), the diffracted plane waves in Eq. (3.14) can be represented by their angular spectra, which consists of plane waves propagating in $z$-direction with spectral function of $f(k_z)$:

$$E_z^{FS}(x = 0^+) = \int f(k_z) e^{ik_z z} dk_z \tag{3.19}$$

Using (3.14), the angular spectrum may be written in terms of the Fourier transform of the spatial distribution of the guided plasmon mode as

$$\begin{aligned} f(k_z) &= \mathcal{F}\{(1+\Gamma)E_z^{SP}\} \\ &= \frac{(1+\Gamma)}{2\pi} \int_{-\infty}^{\infty} E_z^{SP} e^{-ik_z z} dz \\ &= \frac{(1+\Gamma)}{2\pi} I_1(k_z) \end{aligned} \tag{3.20}$$

It should be noted that the angular spectrum representation of the diffracted fields throughout the whole dielectric half-space also involves an additional propagator term, $e^{i\sqrt{k_0^2 - k_z^2}x}$, that complements the free-space diffraction phenomenon (Fig. 3.1a); this term reduces down to unity at the discontinuity, yielding a one-dimensional Fourier integral. The complete description of $E_z^{FS}$ at the dielectric half-space can thus be given as:

$$E_z^{FS} = \frac{(1+\Gamma)}{2\pi} \int I_1(k_z) e^{ik_z z} e^{i\sqrt{k_0^2 - k_z^2}x} dk_z \tag{3.21}$$

This expression is needed to obtain the expressions for $E_x^{FS}$ and $H_y^{FS}$. The latter can be derived through source-free Gauss' law (Eq. (2.1c)):

$$\begin{aligned} E_x^{FS} &= -\int dx \frac{\partial E_z^{FS}}{\partial z} \\ &= -\int dx \frac{\partial}{\partial z} \left( \frac{(1+\Gamma)}{2\pi} \int I_1(k_z) e^{ik_z z} e^{i\sqrt{k_0^2 - k_z^2}x} dk_z \right) \\ &= -\frac{(1+\Gamma)}{2\pi} \int dx \left( \int I_1(k_z) e^{ik_z z} e^{i\sqrt{k_0^2 - k_z^2}x} (ik_z) dk_z \right) \\ &= -\frac{(1+\Gamma)}{2\pi} \int I_1(k_z) e^{ik_z z} e^{i\sqrt{k_0^2 - k_z^2}x} \frac{k_z}{\sqrt{k_0^2 - k_z^2}} dk_z \end{aligned} \tag{3.22}$$

Benefiting from the available electric field functions, the expression for the magnetic field in the free-space ($H_y^{FS}$), can be extracted through the application of Faraday's

law (Eq. (2.1b)):

$$\begin{aligned} H_y^{FS} &= \frac{-1}{i\omega\mu_0}\left(\frac{\partial E_z^{FS}}{\partial x} - \frac{\partial E_x^{FS}}{\partial z}\right) \\ &= -\frac{(1+\Gamma)}{2\pi\omega\mu_0}\int I_1(k_z)e^{ik_z z}e^{i\sqrt{k_0^2-k_z^2}x}\frac{k_0^2}{\sqrt{k_0^2-k_z^2}}dk_z \end{aligned} \tag{3.23}$$

Since the integrals are to be evaluated at $x = 0$ because of the boundary conditions in Eqs. (3.14-3.16), the $x$-dependent terms can be discarded for the forthcoming steps. Hence, the Poynting flux in the free space, just at the boundary, takes on the form:

$$\begin{aligned} &\int_{-\infty}^{\infty} S_x^{FS}dz = -\int_{-\infty}^{\infty} E_z^{FS}H_y^{FS^*}dz \\ &= -(1+\Gamma)\int_{-\infty}^{\infty} E_z^{SP}H_y^{FS^*}dz \\ &= -(1+\Gamma)\int_{-\infty}^{\infty} dz E_z^{SP}\int_{-\infty}^{\infty}\frac{-(1+\Gamma^*)}{2\pi\omega\mu}I_1^*(k_z)e^{-ik_z^* z}\frac{k_0^2}{(\sqrt{k_0^2-k_z^2})^*}dk_z \end{aligned} \tag{3.24}$$

It should be noted that $E_z^{SP}$ can be written in angular spectrum representation as in Eq. (3.20), since it is related to its free-space counterpart through the boundary conditions. This results in a complicated integral representation as

$$\begin{aligned} \int_{-\infty}^{\infty} S_x^{FS}dz = \frac{(1+\Gamma)(1+\Gamma^*)}{2\pi\omega\mu}\int_{-\infty}^{\infty} dz\left(\int_{-\infty}^{\infty} I_1(k_z)e^{ik_z z}dk_z\right) \\ \times\left(\int_{-\infty}^{\infty} I_1^*(k_z)e^{-ik_z^* z}\frac{k_0^2}{(\sqrt{k_0^2-k_z^2})^*}dk_z\right) \end{aligned} \tag{3.25}$$

Integration of the Poynting flux essentially corresponds to the total energy along the z-axis. In this case, the space-domain $E \times H^*$ is the energy per unit space. Parseval's relation [98] dictates that the total energy of the signal can be deduced from the spatial or spectral power density. Thus, time-domain field contributions can be reduced down under a single integral along the spectral domain with their angular components only $(E(k_z)H(k_z)^*)$. The Poynting integral thus reduces down to:

$$\int_{-\infty}^{\infty} S_x^{FS}dz = \frac{(1+\Gamma)(1+\Gamma^*)}{2\pi\omega\mu}\int_{-\infty}^{\infty}\frac{|I_1(k_z)|^2k_0^2}{(\sqrt{k_0^2-k_z^2})^*}dk_z \tag{3.26}$$

Through the assumed power flux boundary condition, Eqs. (3.18) and (3.26) can be equated as:

$$-(1+\Gamma)(1-\Gamma^*)\int_{-\infty}^{\infty} E_z^{SP}H_y^{SP*}dz = \frac{(1+\Gamma)(1+\Gamma^*)}{2\pi\omega\mu}\int_{-\infty}^{\infty}\frac{|I_1(k_z)|^2k_0^2}{(\sqrt{k_0^2-k_z^2})^*}dk_z \tag{3.27}$$

Further simplification of the obtained identity yields:

$$\frac{(1-\Gamma^*)}{(1+\Gamma^*)} = \frac{-1}{2\pi\omega\mu\int_{-\infty}^{\infty} E_z^{SP} H_y^{SP*} dz} \int_{-\infty}^{\infty} \frac{|I_1(k_z)|^2 k_0^2}{(\sqrt{k_0^2 - k_z^2})^*} dk_z \tag{3.28}$$

In addition, integral substitution with $dk_z = k_0 du$ can be applied to the expression [99], which boils down to:

$$\frac{(1-\Gamma^*)}{(1+\Gamma^*)} = \frac{-1}{\lambda_0\eta_0\int_{-\infty}^{\infty} E_z^{SP} H_y^{SP*} dz} \int_{-\infty}^{\infty} \frac{|I_1(u)|^2}{(\sqrt{1-u^2})^*} du \tag{3.29}$$

where $\lambda_0$ and $\eta_0$ are the wavelength and wave impedance in free-space, respectively. This expression has singularities at $k_z = \pm k_0$; as a result, appropriate measures should be taken during the numerical integration. A similar derivation for the metallic discontinuity (Fig. 3.1b) can also be made. It follows the same assumptions and expands the diffracted fields as a continuum of plane waves in the conductive half-space. Due to the finite conductivity of the metal, a large portion of the plane wave spectrum consists of evanescent fields. The reflection formula for this case can be summarized as:

$$\frac{(1-\Gamma^*)}{(1+\Gamma^*)} = \frac{-1}{\lambda_0\eta_0\int_{-\infty}^{\infty} E_z^{SP} H_y^{SP*} dz} \int_{-\infty}^{\infty} \frac{|I_1(u)|^2 \varepsilon_m^*}{(\sqrt{\varepsilon_m - u^2})^*} du \tag{3.30}$$

where $\varepsilon_m$ is the complex relative permittivity of the metal.

In a recent paper by Sharifi and Gordon [100], the mode-matching formula has adapted the unconjugated orthogonality relationship. The validity and interpretation of this approach is elaborated in Appendix B.

### *3.2.3 First-order surface impedance approximation*

In constrast to the vectorial mode maching method, for which the numerical integration is necessary, calculation of the evanescent fields inside the metallic termination (as in Fig. 3.10) can be completely bypassed through the application of the first-order surface impedance boundary condition (SIBC), also known as the Leontovich boundary condition. This condition is applicable to conductive surfaces in which the internal field in the tangential direction varies relatively small as compared to the normal field. Moreover, the structure is also assumed to be much larger than the skin depth of the metal [101]. The Leontovich boundary condition relates the

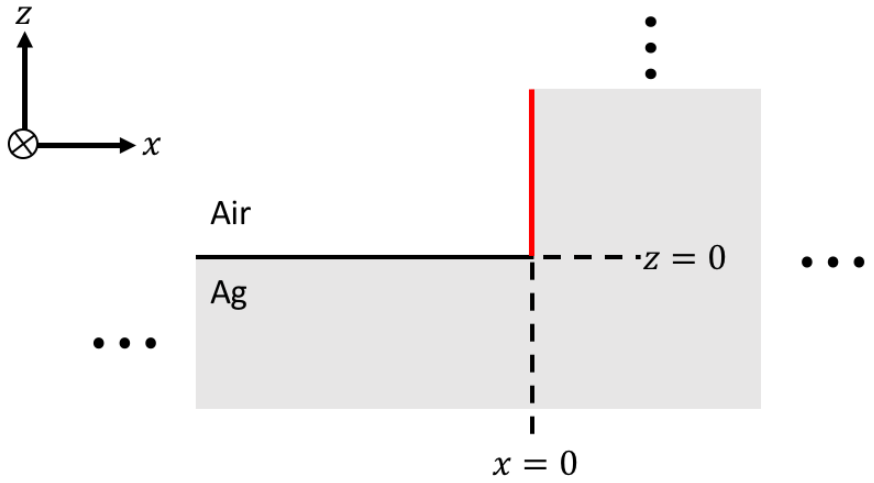


Figure 3.10: An abrupt metallic termination for SPPs, referred to as "short" in the text. The impedance boundary conditions are applied to the semi-infinite interface as highlighted in red.

tangential components of the incident field at a finitely conducting interface as

$$E_t(x=0) = \eta_m H_t(x=0) \times \hat{n} \tag{3.31}$$

where $E_t$ and $H_t$ are the total electric and magnetic fields at the surface of the vertical metal termination, $\eta_m$ is the surface impedance of the metal and $\hat{n}(=-\hat{x})$ is the surface normal to the termination on Fig. 3.10. Because the large portion of the SPP for $x < 0$ is concentrated in the metal-dielectric interface, and because it extends into the air more than it does into the metal, applying the boundary condition (3.31) for $z > 0$ is assumed to capture the effect of the termination in the reflected fields. Therefore, substituting the SPP field components into the boundary condition (3.31) results in:

$$E_z^{SP}(1+\Gamma) = -\eta_m H_y^{SP}(1-\Gamma) \tag{3.32}$$

and, with a simple rearrangement,

$$\frac{1-\Gamma}{1+\Gamma} = -\frac{E_z^{SP}}{H_y^{SP}\eta_m} \tag{3.33}$$

Note that, although the ratio of the transverse field components of waves (TE, TM and TEM) in homogenous media is generally defined as the wave impedance, the

ration in (3.33) can not be directly referred to as the wave impedance because of the inherent inhomogeneity of the structure that supports SPPs. However, since the boundary conditions are enforced only for $z > 0$, the wave impedance of the dielectric half-space can be utilized as a reasonable approximation for the ratio of $E_z^{SP}/H_y^{SP}$. Substituting the SPP field expressions in (2.33) and (2.35) into (3.33), a simple and approximate expression for the reflection coefficient can be obtained as

$$\Gamma \approx \frac{1 - \frac{\beta}{\omega\varepsilon_0\eta_m}}{1 + \frac{\beta}{\omega\varepsilon_0\eta_m}} \tag{3.34}$$

While the approximate model can reasonably predict the induced phase, it fails to capture the trend for the magnitude of the reflection. This could be attributed to the partial application of the boundary conditions at $x = 0$, which is essentially a crude approximation and it has turned out to be so in this study. The surface impedance in the vicinity of sharp edges is subject to change due to non-smooth discontinuity and often entails rigorous treatment by means of perturbation theory [101].

### *3.2.4 Numerical assessment of approximate models*

In this subsection, the performance of the derived models are compared with the results from the FDTD simulations for two different terminations, referred to as "open" and "short" corresponding to dielectric and metallic terminations, respectively, as shown in Fig. 3.11 with their transmission line analogues. For reference, the reflection coefficients were obtained using both the EME and GPOF methods, and for the GPOF method, two exponentials were used for the approximations of the propagating waves along the interface. In order to further assess the applicability of the models to different metallic terminations, an additional test case with an inhomogeneous wedge is also studied.

*Dielectric termination: "Open circuit"*

The comparison of the models for reflection coefficient values from the "open" termination is presented in Fig. 3.11a. It should be noted that the SIBC model is not

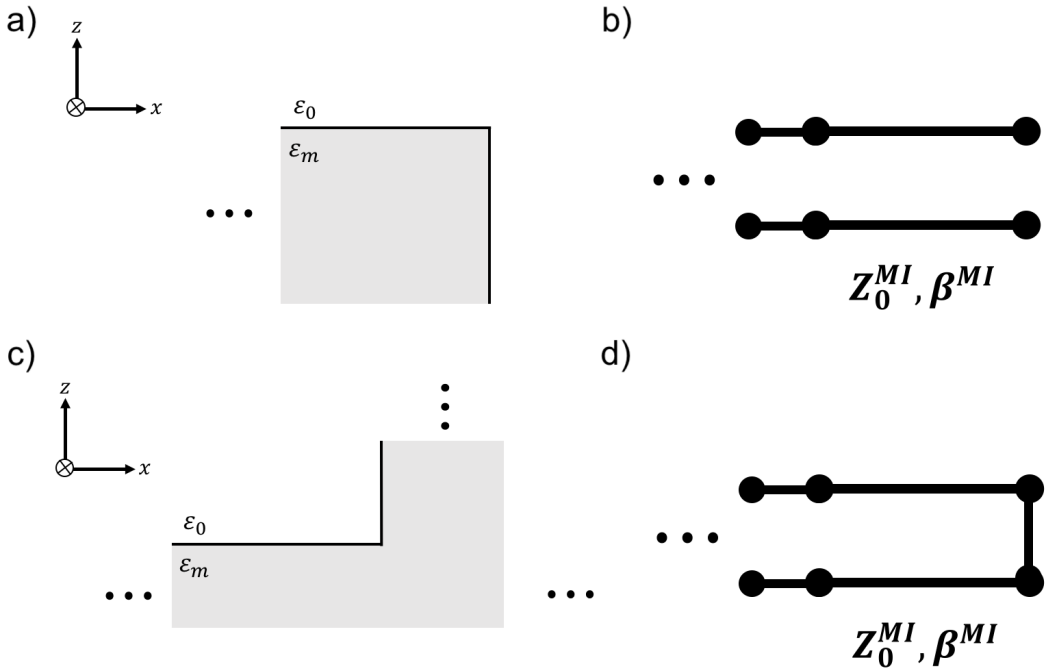


Figure 3.11: Plasmonic discontinuities and their transmission line analogues in microwave theory: a) "Open" metallic termination, b) Open-circuited transmission line, a) "Short" metallic termination, b) Short-circuited transmission line

applicable to this problem due to its dependence on explicit impedance boundaries, which is absent in dielectric termination. The FDTD results were processed by the EME and GPOF methods, and the ones with EME are assumed to be the reference data to check the accuracy of the other methods. As expected, the effective medium approach underestimates the reflection magnitude and completely fails to represent the phase, since the TM nature of the mode and complex diffraction phenomena at the end face are completely ignored. While the vectorial mode-matching method offers the closest coefficients to the FDTD simulations, some degree of discrepancy between these results exist, possibly due to the nature of the approximation, which assumes the absence of backscattered radiation modes. Despite the early numerical observations by Wallis et al. [102], which forms the basis of the assumption for the vectorial approach [95], backscattering in the near to far-field zone is predicted by the Sommerfeld-Malyuhinets theory [65, 69], and also demonstrated by experimental work [69]. Based on the aforementioned observations, the vectorial approach

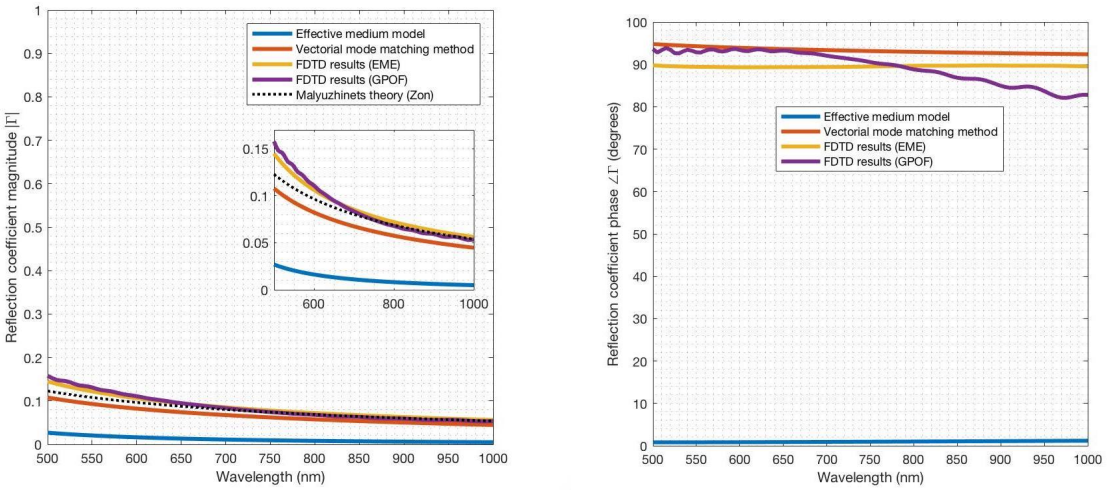


(a) Reflection coefficient magnitude vs. free-space wavelength

(b) Reflection coefficient phase vs. free-space wavelength

Figure 3.12: Reflection coefficients vs. wavelength, obtained from the effective medium model, vectorial mode-matching method and the FDTD simulations for "open-circuited" termination (dielectric termination in Fig. 3.1). For reference purposes, the magnitude of reflection coefficient as predicted by Malyuzhinets theory is also provided. The FDTD results are presented with both the EME and GPOF post-processing in order to assess their performances.

appears to be more grounded and efficient for MIM waveguides, as these structures largely lack the radiative modes due to highly absorbing claddings [45].

In addition, Malyuzhinets technique-based calculations predict varying degrees of SPP coupling to the waveguide and end-faces. Zon has reported that a small portion of the incoming SPP field is reflected back, which the author characterized with an approximate reflection formula for metals with dominantly imaginary surface impedances in the optical domain [65]:

$$|\Gamma| \approx \frac{-2\eta''_m}{3\sqrt{3}} \tag{3.35}$$

where $\eta_m = \eta'_m + i\eta''_m$. This expression is also plotted in Fig. 3.12 for reference; it shows close agreement with the vectorial method and the FDTD data. Nevertheless, Zon's results were contested by a subsequent formulation by Kotelnikov et al., who argued that the diffracted fields are not able to excite reflected or refracted SPPs on the either edge of the wedge [69]. By contrast, numerical results by Mayoral-

Astorga et al. suggest SPP coupling at both faces of the wedge. [103] Similarly, FDTD calculations in this thesis indicate a very small coupling to backward SPP modes, ranging from 1.8% to 0.04% of the incident power.

*Metallic termination: "Short circuit"*

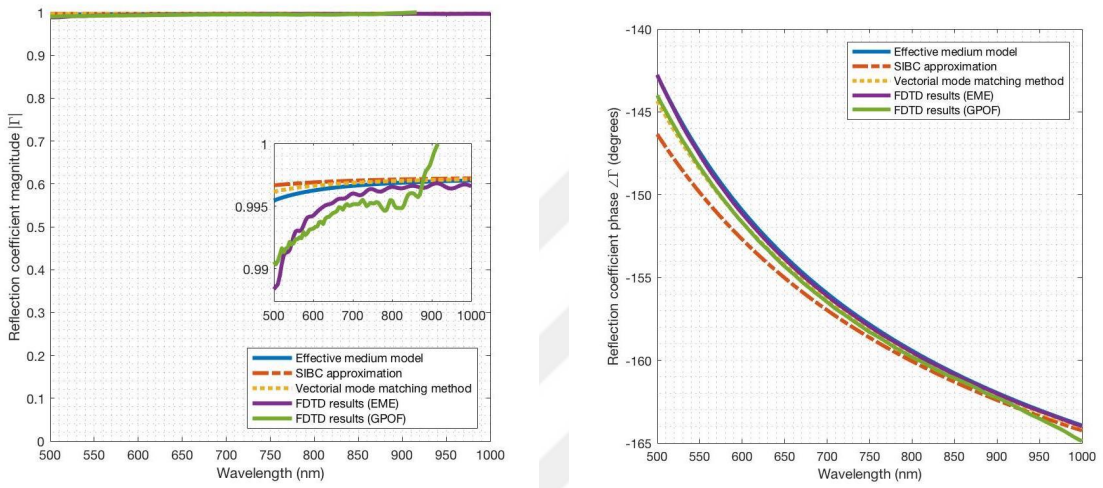


(a) Reflection coefficient magnitude vs. free-space wavelength

(b) Reflection coefficient phase vs. free-space wavelength

Figure 3.13: Comparison of reflection coefficients obtained from approximate models and FDTD simulations for a metallic wall (Fig. 3.10). FDTD results were provided both for EME and GPOF post-processing; divergence of the amplitude at longer wavelengths for GPOF processing is unphysical.

The comparison of generalizable models for metallic reflection case is provided on Fig. 3.13. Even though all approaches are able to predict the primarily inductive behavior of the metallic wall, owing to the primarily reactive nature of bulk metals in optical frequencies [19],[1] none of the models are able to reproduce the exact amplitude curve of the FDTD results, particularly for shorter wavelengths. In terms of amplitude, all generalizable models yield very close results, with the effective medium model yielding the closest result, albeit still with a relative divergence.

[1]It should be noted that the phasor of an inductor would take on the form $-i\omega L$ for the $e^{-i\omega t}$ time dependency [19].

In contrast to the dielectric termination case, the vectorial method does not offer an improvement over the simpler models; moreover, it is more computationally expensive compared to the other techniques. The GPOF results were also shown to diverge for larger wavelengths.

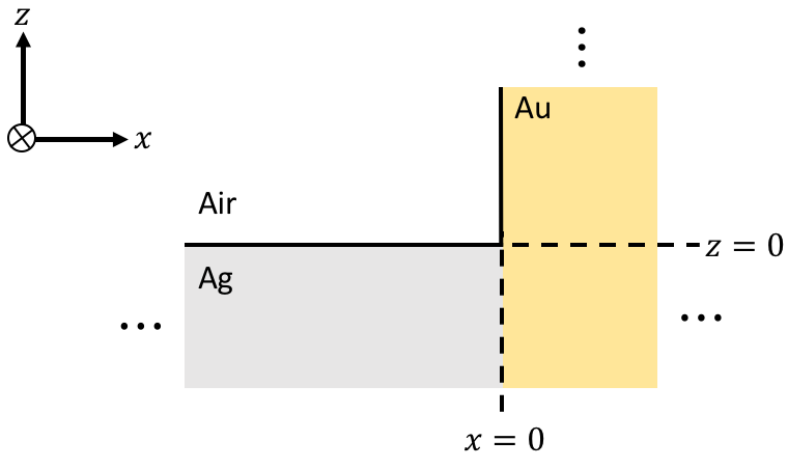


Figure 3.14: Reflection from an inhomogenous metallic wall. The wall is modeled as a gold half-space.

To demonstrate their limitations, the models were also assessed with an inhomogenous discontinuity, where the impedance wall is modeled as gold, as seen on Fig. 3.14. The Drude parameters are obtained from the gold dataset by Babar and Weaver [31] ($\varepsilon_\infty = 1$, $\varepsilon_\infty = 1$, $\omega_p = 1.299e16$ rad/s and $\nu = 2.7954e13$ rad/s). The reflection magnitude and phase plots for this case are provided on Fig. 3.15. The phase results are in close agreement with the FDTD data, which supports the fact that reflection is largely mediated by the reactive nature of the barrier. All methods except the mode index approach showcase relatively aggravated magnitude results, with SIBC approximation and vectorial method producing completely irreconcilable curves with respect to the simulation data. Nevertheless, considering that the radiation coupling is low for this structure and the reflection amplitude is close to unity for all approaches and the simulation calculations, the developed models can be assumed to be valid, particularly for higher wavelengths. The analogous case for SPP reflection from an inhomogenous dielectric discontinuity is not considered,

since this configuration is known to produce significant backscattering [94, 102].

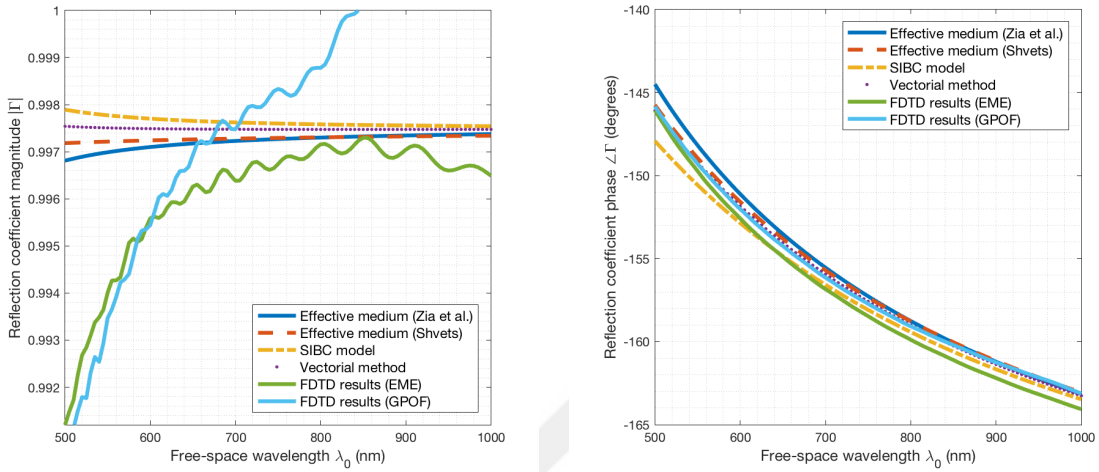


(a) Reflection coefficient magnitude vs. free-space wavelength

(b) Reflection coefficient phase vs. free-space wavelength

Figure 3.15: Comparison of reflection coefficients obtained from approximate models and FDTD simulations for an inhomogenous metallic wall (Fig. 3.14) with alternative Drude parameters ($\varepsilon_\infty = 1$, $\omega_p = 1.2976e16$ rad/s, $\nu = 3.26751e13$ rad/s)

### *3.2.5 Fabry-Pérot model for resonant optical tunneling*

The performances of the developed models can be further appraised through extended examples, such as SPP tunneling from infinitely-long but finitely-thick barriers, as shown in Fig. 3.16. Tunneling behavior in optics is largely associated with evanescent wave coupling. It is analogous to one-dimensional electron tunneling through a finite potential barrier in quantum mechanics [104]. Tunneling phenomenon can also occur in metallic structures which are relatively lossy in the optical regime; in such cases, frustrated-total internal reflection and attenuated total internal reflection often go hand-in-hand.

Optical tunneling of surface plasmons have been studied for periodic grooves [105, 106], inhomogeneous discontinuities in hybrid waveguides [107, 108, 109] and nanoparticle gaps [110]. In this section, a simple interference model is introduced for the tunneling of surface plasmon polaritons from a finitely-thick metallic barrier

(Fig. 3.16). The metallic barrier is assumed to be infinitely tall to bypass any possible edge-diffraction effects at the upper end: it extended through the PML regions. The results are compared with those by the FDTD simulations. Due to the additional memory requirements associated with the GPOF method and its relatively noisy performance, the EME method has been appropriated as the sole post-processing method for this study.

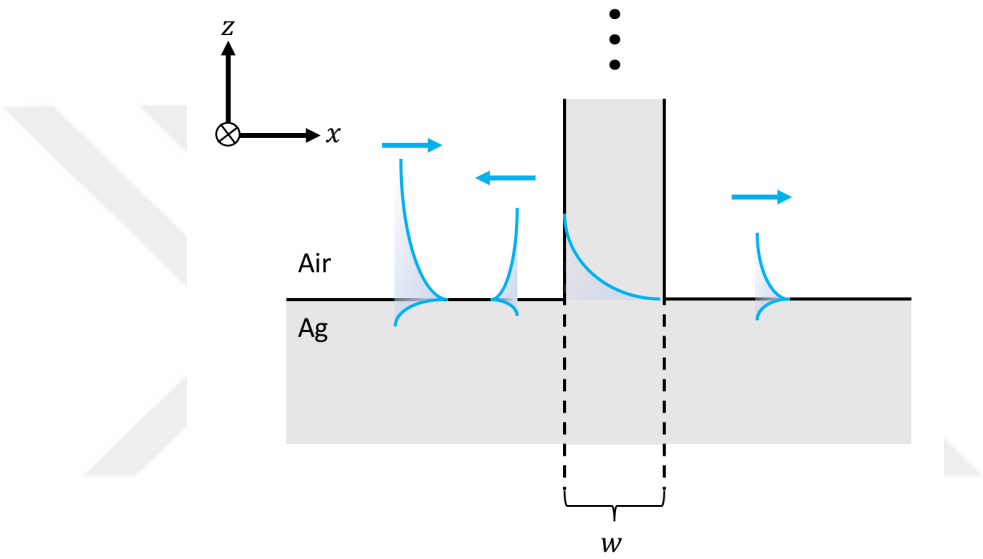


Figure 3.16: An infinitely-tall metallic barrier on a single-interface plasmonic waveguide. The discontinuity has a width of $w$.

Even though tunneling of plasmons from dielectric barriers has been modeled computationally and experimentally in the past [107, 111, 103], a Fabry-Pérot model is not applicable to this problem, since this model is mediated largely by the conductive properties of the intermediate metallic layer. Notwithstanding the use of effective medium model for similar channel plasmon slots by Bozhevolnyi [112], this approach is not applicable to this reflection problem as it is mainly centered on the modal analyses of such structures. Thus, the complex diffraction phenomena involving multiple edge scattering events for this case necessitate a more extensive treatment, preferably by means of full-wave analysis.

*Thin-film interference analysis*

An infinitely-long metallic barrier on a single-interface plasmonic waveguide can be interpreted as a lossy Fabry-Pérot cavity that is stacked in between a homogenous medium, as seen on Fig. 3.18. Assuming that the Leontovich surface impedance boundary conditions hold for metals in the optical regime, an arbitrary TM-field impinging upon the metal barrier would penetrate it almost normally, with little to no lateral variation [101, 113]. Thus, the field inside the cavity can be approximated as a TEM wave with a uniform phase pickup and a complex wavenumber of $k_m$. Additionally, it would be imperative to define appropriate reflection and transmission coefficients for each interface, which can be seen in Fig. 3.17: $r_{12}$ and $t_{12}$ represent the reflection and transmission coefficients for a wave travelling from waveguide *(medium 1)* to metallic region *(medium 2)*. $r_{21}$ and $t_{21}$ correspond to the respective parameters for the reversed propagation direction. Treating the plasmonic waveguide as a single effective medium would simplify the analysis to a three-layered transverse resonance problem; this approach is in line with the quasi-TEM approximation inside the barrier.

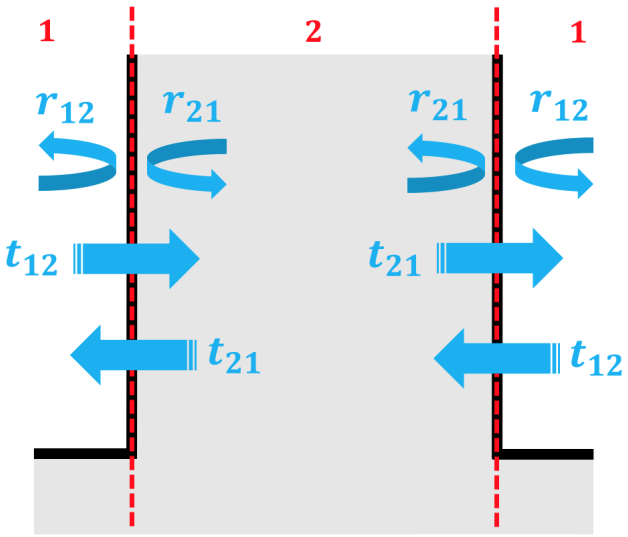


Figure 3.17: Reflection and transmission coefficients for a metallic barrier structure

Based on the standard thin-film interference for a cavity of length $w$, the gener-

alized transmission coefficient $\hat{t}$ can be defined based on a sum of infinite series of the transmitted fields, as seen in Fig. 3.18. The end result is the same as Eq. (2.19):

$$\hat{t} = \frac{(1 - r_{12}^2)e^{ik_m w}}{1 - r_{12}^2 e^{ik_m 2w}} \tag{3.36}$$

In a similar fashion, the overall reflection coefficient of the system is the same as the GRC given in Eq. (2.18):

$$\hat{r} = \frac{r_{12} - r_{12}e^{ik_m 2w}}{1 - r_{12}^2 e^{ik_m 2w}} \tag{3.37}$$

for which the relation $r_{21} = -r_{12}$ is presumed to hold, owing to the effective

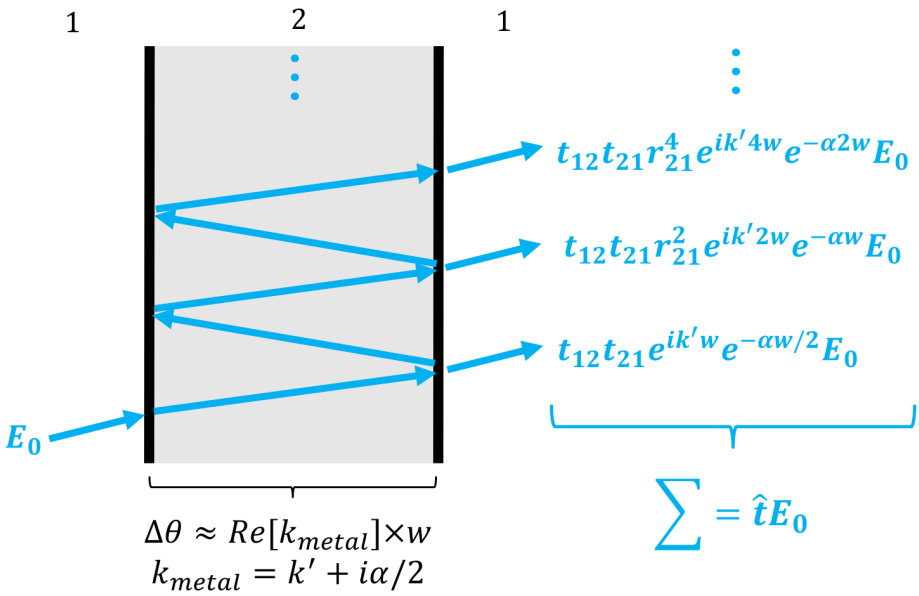


Figure 3.18: A lossy Fabry-Pérot etalon. Medium 2 is the metallic barrier sandwiched between the dielectric materials on both sides, chosen to be the same. Total transmitted field can be represented by the sum of an infinite series, due to the multiple reflections in Medium 2.

medium treatment of the metal-dielectric interface. Based on this approach, the inhomogeneous medium can be represented by the approximate models that were developed on section 3.2.

*Complex penetration constant*

In order to accurately formulate the Fabry-Pérot model, we would need the complex propagation constant of the field inside the barrier, which can be approximated by the wavenumber in metal, $k_m$ ($= \sqrt{\varepsilon_m} k_0$). We can alternatively define this parameter as the *complex penetration constant* to distinguish it from the actual propagation constant of the SPP in metal-insulator waveguide. Considering the approximations that we have made in the previous subsections, we can utilize the following alternatives based on the approximate modal analyses:

1. In the barrier, the inbound SPP would oscillate as it would dampen. Per transverse resonance condition, a portion of the oscillating wave would couple to a distinct insulator-metal-insulator mode for the three layered interface, which would propagate throughout the infinitely-long barrier: this corresponds to the $z$-direction in Fig. 3.16. A reasonable approach is picking the penetration depth and constant of this mode in the metallic layer for our analysis. In order to obtain this parameter, we would need the propagation constant of the primary, long-rage IMI mode ($\beta_{barrier}$), which would be defined by the transcendental dispersion relation. The "dielectric" layers can be considered either as vacuum or effective SPP index that was defined in the previous section.

2. Both surfaces of the metallic barrier can be treated independently. In this case, the field inside the cavity can be assumed to penetrate it in the same way as an SPP in single interface would, reducing the penetration constant to:

$$k_{metal} = \sqrt{\varepsilon_m k_0^2 - \beta_{\mathrm{SPP}}^2} \tag{3.38}$$

   This approach would be more reasonable for thicker barriers, for which the surface excitations decouple.

Numerical calculations indicate that both approaches yield very close results. Since the former includes iterative root-finding operations by the courtesy of IMI approach, the latter method is more desirable.

*Numerical results*

The numerical results for the transmission and reflection coefficients are provided in Figs. 3.19 and 3.20 for the reference free-space wavelengths of 630 and 1000 nm. The barrier widths are normalized with respect to the SPP skin depth $\delta_m$, which is defined as [21]:

$$\delta_m = \frac{1}{Re[k_{zm}]} = \frac{1}{Re[\sqrt{\beta^2 - \varepsilon_m k_0^2}]} \tag{3.39}$$

While all models showcase close agreement with the FDTD data for transmission magnitude, there is minor divergence for thinner barriers. This is expected, as the surface impedance approximation that forms the basis of the approach slowly breaks down for dimensions smaller than the skin depth. Phase relations for different models also present a similar trend; nevertheless, deviation and convergence offset is higher for smaller wavelengths.

## *3.3 Conclusion and summary*

This chapter focused on the SPP behavior at an abrupt termination in a one-dimensional waveguide. These abrupt discontinuities are often modeled as conductive exterior and interior wedges; nevertheless, due to the scattering and diffraction effects, their analyses by analytical means are either impossible or quite tedious. Therefore, approximate and generalizable models are used to robustly extract the constitutive network parameters, such as reflection coefficients.

Effective medium and vectorial mode matching theories at discontinuities have been developed from the electromagnetic theory; dominance of the fundamental SPP mode at the waveguide is presented as a key assumption. In addition, a simple model based on SIBC is introduced. The approaches have been compared with the reflection coefficients obtained from the FDTD analyses. Finally, the validity of the generalizable approaches are further assessed through an application on the optical tunneling from a finitely-thick impedance barrier by the means of a Fabry-Pérot formalism. This model was shown to yield efficient results and estimate the reflection and transmission coefficients of the barrier with relatively high accuracy.

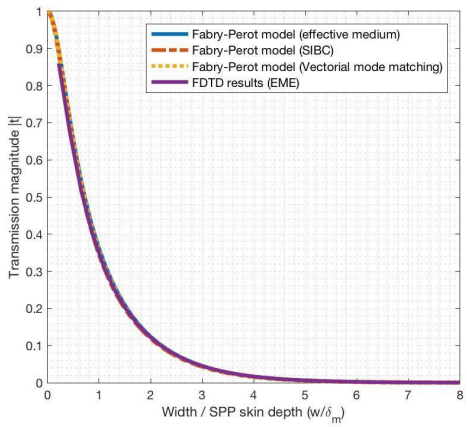


(a) Transmission magnitude for free-space wavelength of 630 nm

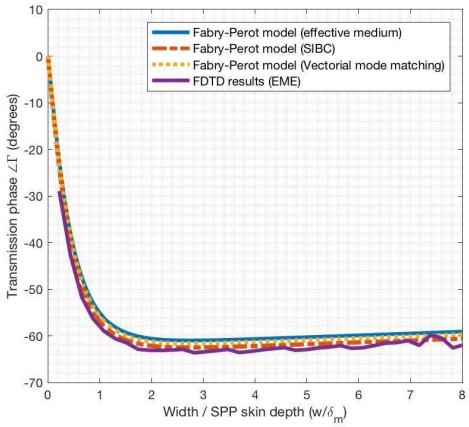


(b) Transmission phase for free-space wavelength of 630 nm

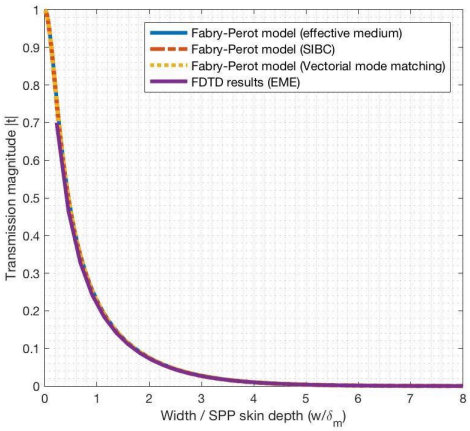


(c) Transmission magnitude for free-space wavelength of 1000 nm

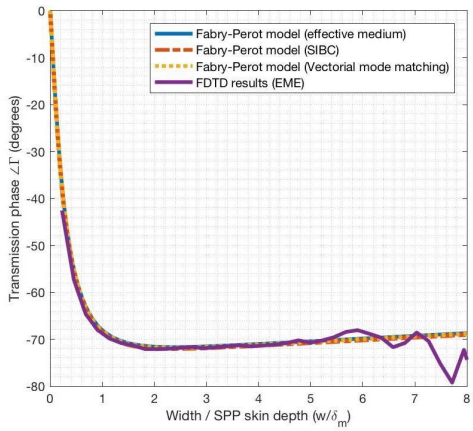


(d) Transmission phase for free-space wavelength of 1000 nm

Figure 3.19: Transmission coefficient plots with respect to normalized barrier widths for optical tunneling of a SPP wave for the structure in Fig. 3.16 at two different wavelengths: 630 and 1000 nm

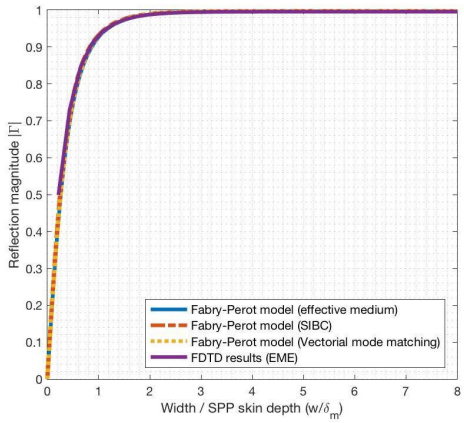


(a) Reflection magnitude for free-space wavelength of 630 nm

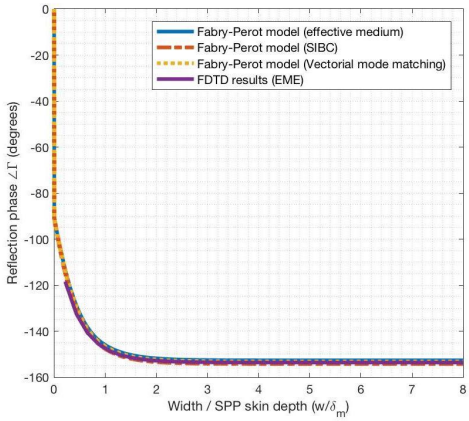


(b) Reflection phase for free-space wavelength of 630 nm

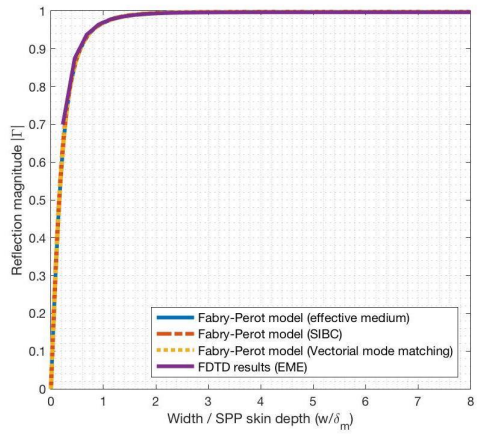


(c) Reflection magnitude for free-space wavelength of 1000 nm

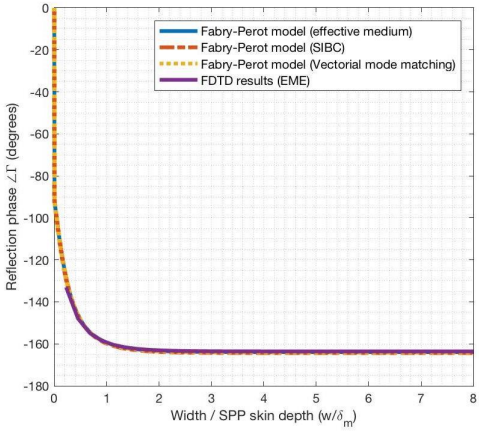


(d) Reflection phase for free-space wavelength of 1000 nm

Figure 3.20: Reflection coefficient plots with respect to normalized barrier widths for the structure in Fig. 3.16 at two different wavelengths: 630 and 1000 nm

# Chapter 4

# SURFACE PLASMON BEHAVIOUR AT STEP AND GAP DISCONTINUITIES

While the generalizable models for "shorted" and "open" plasmonic terminations offer an intuitive background to the SPP behaviour at end-faces, they alone do not offer the full picture. Unlike full-on waveguide terminations, discontinuities involved in the design of most plasmonic devices such as gratings, couplers and optical nano-antennas often feature depths and widths as additional degrees of freedom. Furthermore, interaction of surface waves with such subwavelength geometries give rise to unique electromagnetic phenomena, such as extraordinary optical transmission (EOT) [72]. The transmissive behavior of the SPPs, largely due to the coupling effects of the diffracted angular spectra, is largely overlooked in the previous chapter; this phenomenon will form the catalysis of this chapter.

In order to provide a better understanding of SPP interaction with finite-sized nanoscale discontinuities, side-coupled cavity model and its application to steps and grooves will be discussed. Based on this approach, SPP reflection and transmission can be characterized by internal resonances at the cavities formed by the rear or side surfaces, akin to the localized surface plasmon phenomenon. Largely centralized for groove-like, depressed indentations [114, 115], this treatment will also be extended to cover the salient properties of step and ridge structures. Throughout this chapter, the Drude model for silver, introduced for the previous discussions on SPP reflection, will be employed to model discontinuities.

Even though the SPPs are not the sole contributors to the reflective and transmissive behaviour of subwavelength metallic structures, particularly due to the presence of QCWs in the near-field [86, 88], steady-state response of many such geometries can be sufficiently described or at least interpreted by the cavity resonances of such

surface waves [72]. Since reflection and transmission coefficients are closely intertwined with the network theory in microwave engineering, the side-coupled cavity model will be further contextualized by the introduction of possibly-equivalent network and transmission line topologies for these structures.

## *4.1 Step discontinuities*

Wedge-type discontinuities, covered extensively in the previous chapter, may be further complicated by introducing a finite height to the discontinuity, which results in simple steps with a depth or a height, as shown in Figs. 4.1(a) and (b), respectively. For convenience, these structures will be referred as steps with negative and positive heights with respect to the leftmost layer. Such discontinuities were examined numerically by H. A. Jamid and S. J. Al-Bader [116] as an extension of their past work on dielectric ("open") terminations [117]. Refraction and diffraction of SPPs through step discontinuities were also experimentally realized and analyzed by multiple research groups, either by means of prism or electron coupling [118, 119].

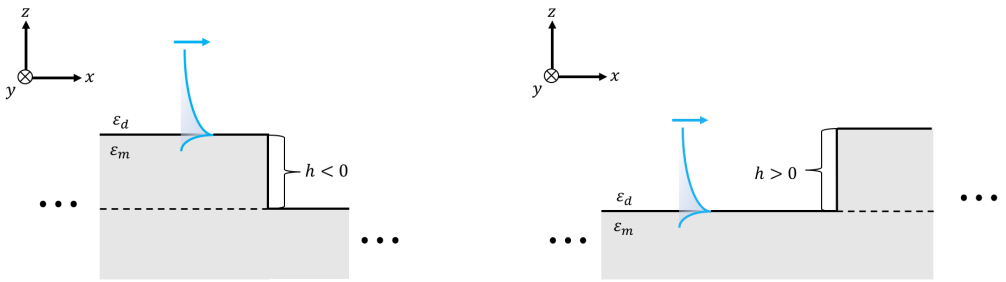


(a) Depressed step discontinuity with "a negative height"

(b) Elevated step discontinuity with "a positive height"

Figure 4.1: Two types of step discontinuities with a height of $h$; the incident SPP, propagating in positive $x$-direction, is highlighted as blue.

These two steps, while being mirror images of each other with respect to the $z$-axis, are not reciprocal due to the inhomogeneity of the surface waveguide and the SPP field: in more rigorous terms, the input impedance that the SPP field sees at the edge of the discontinuity is different due to the asymmetric material

properties. Existence of an additional edge also introduces a secondary source for plasmon diffraction, which results both in SPP excitation in the both sides of the discontinuity. In addition, the response of the step is further complicated by the cross-coupling between SPPs and QCWs in the near field [86], which is rampant especially for subwavelength heights. Radiative losses in these structures due to the open-nature of constitutive waveguides contrast with their microstrip counterparts in RF technology, which are largely reactive in nature [17].

In this section, salient properties of step discontinuities will be analyzed through supplementary FDTD data, which is obtained for depressed and elevated steps, simulated by increments of 10 $nm$ up to 1 $\mu m$. As a result of these simulations, the magnitudes and phases of reflection and transmission coefficients are compiled in Fig. 4.2, where magnitudes and phases are coded in colors while height of the step and wavelength of the operation (i.e., independent variables) are used as the vertical and horizontal axes, respectively.

### *4.1.1 Cavity model: Asymmetry of the scattering parameters and periodic reflection*

Upon studying the reflection and transmission coefficients given in Fig. 4.2, it can be observed that (i) they demonstrate fundamentally different natures for the positive and negative heights of the steps, and (ii) for the negative heights (depressed steps), the reflection coefficient exhibits periodic signature with respect to the height of the step, manifesting a resonance behavior along the vertical edge of the step. Observed as early as in the paper by H. A. Jamid and S. J. Al-Bader [116], this periodic behavior is largely absent from steps with positive heights. This can be reasoned through the effective impedance that the inbound SPP first encounters at the discontinuity: since the impedance of the elevated step relatively slowly converges to the asymptotic limit for a full metallic half-space ("shorted" termination), the reflection coefficient is mostly affected by the diffraction and scattering at the edges. Thus, the modulatory effect of side-coupling is largely suppressed for the elevated steps and convergence to the asymptotic reflection coefficient value is quick and smooth: even for relatively small heights, the effective reflection phase closely

follows the inductive phase limit that is predicted by the reflection models in Chapter 3. In contrast, the effective impedance that the surface wave first sees at the upper edge of the depressed step quickly approaches to that of the dielectric half-space ("open" termination) due to the SPP skin depth. It should be noted that the reflection coefficient magnitude and phase roughly oscillates around this asymptotic value, even for large step depths: this is a result of SPP side-coupling.

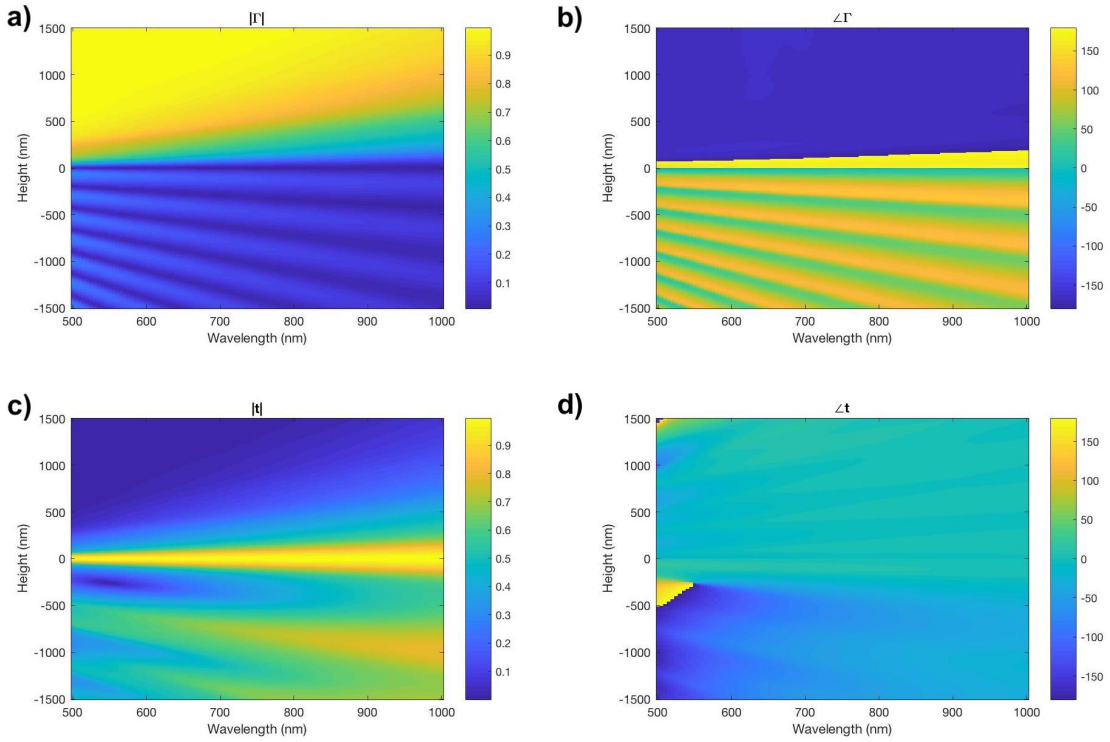


Figure 4.2: SPP behavior at metallic steps with different heights: a) reflection coefficient magnitude $|\Gamma|$; b) reflection coefficient phase $\angle\Gamma$; c) transmission coefficient magnitude $|t|$ and d) transmission coefficient phase $\angle t$. Negative and positive heights are associated with Figs. 4.1a and 4.1b, respectively.

Based on the oscillatory behavior of the reflection coefficient for the step-down discontinuities, the interaction of SPPs with these junctions can be modeled by a transmission line network, at which the SPP field along the vertical edge, denoted by an equivalent voltage, bounces back and forth between the "open" and "short" terminations. Thus, the side wall of the step can be viewed as a cavity on its own, as it is depicted in Fig. 4.3 together with its circuit model, where each wedge is

modeled as two-port network, denoting the quasi-open and quasi-short junctions. Since the corners of the step discontinuity, one on the top and one at the bottom,

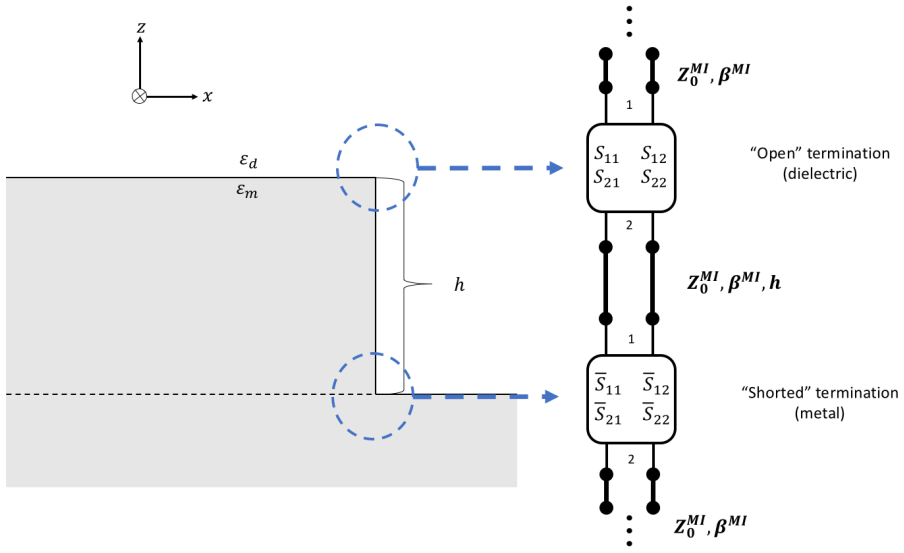


Figure 4.3: Equivalent network for a depressed step discontinuity

have already been studied in terms of their reflection and transmission coefficients, each constituting parts of the step can be characterized by its own two-port S-parameters as

$$\begin{aligned} S_{11} &= S_{22} = \Gamma_d \\ S_{12} &= S_{21} = t_d \\ \overline{S}_{11} &= \overline{S}_{22} = \Gamma_m \\ \overline{S}_{12} &= \overline{S}_{21} = t_m \end{aligned} \tag{4.1}$$

where $\Gamma$ and $t$ denote the reflection and transmission coefficients while the associated subscripts $d$ and $m$ indicate the "open" (dielectric) and "short" (metallic) junctions, respectively. In addition, the section that connects these two corners are also modeled as an intermediate transmission line with the same characteristic impedance ($Z_0^{\mathrm{MI}}$) and propagation constant ($\beta$) as the single interface plasmonic waveguide. Since the side-cavity is preceded and succeeded with the same type of waveguide, the entrance and exit ports of the whole network are matched with the same characteristic impedance $Z_0^{\mathrm{MI}}$. While the characteristic impedance $Z_0^{\mathrm{MI}}$ can be defined

arbitrarily as long as the equivalent voltages and currents on the transmission line accurately represent the SPP power flow [37], this is not necessary for this analogy.

As covered in the previous chapter, the edge discontinuities in question showcase different resistive and reactive properties. Thus, the resulting overall response of the step discontinuity is expected to be non-reciprocal, notwithstanding the symmetry of each individual network. Noting the characteristic impedance loads at each end-face, it can be deduced that the impedance which inbound voltage waves encounter would be different by each direction of propagation ($\mp x$). This results in asymmetry of reflection and transmission coefficients by the sign of the step height.

Based on the side-coupling approach, the periodic behavior of the total reflection coefficient for the step-downs can be associated with a Fabry-Pérot resonance on the representative transmission line. Thus, based on the GRC representation in Eq. (2.18), the total reflection coefficient of a step-down with depth $h$ can be written as:

$$\Gamma_{\text{step}} = \Gamma_d + \frac{t_d t_d \Gamma_m}{1 - \Gamma_d \Gamma_m e^{i\beta_{\text{SPP}} 2h}} \tag{4.2}$$

In addition, the associated resonance condition can also be summarized as

$$l2\pi = 2Re[\beta]h + \angle\Gamma_d + \angle\Gamma_m \tag{4.3}$$

with the resonance order $l$ being a natural number. Since the necessary S-parameters in Eqs. (4.1) can be deduced from a single-run FDTD simulation, the reflection coefficient of this structure can be closely reproduced from this data. The predicted magnitude and phase curves for this coefficient are provided in Figs. 4.4a to Figs. 4.4d for the free-space wavelengths of 630 $nm$ and 1000 $nm$, respectively. The model offers a very close agreement with the FDTD results for steps that are deeper than the skin depth of the SPP in metal. For steps that are shallower than the skin depth of the metal, effective impedance that inbound SPP sees at the open-circuited wedge is different from the asymptotic value for the wedge-type discontinuity. In addition, quasi-cylindrical and evanescent modes are also likely to play roles for the observed deviations from the model.

In addition to the reproduction of reflection coefficients by the FDTD data,

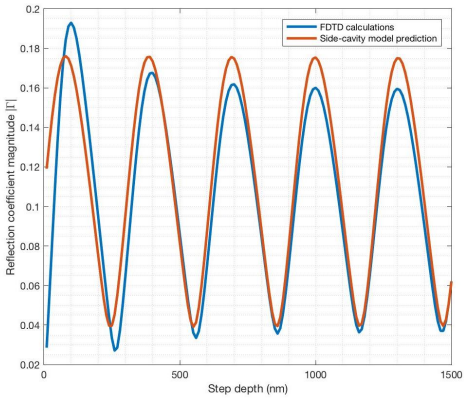


(a) Reflection coefficient magnitude at $\lambda_\circ = 630\ nm$

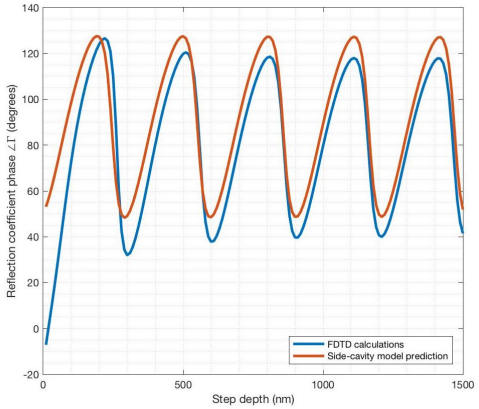


(b) Reflection coefficient phase at $\lambda_\circ = 630\ nm$

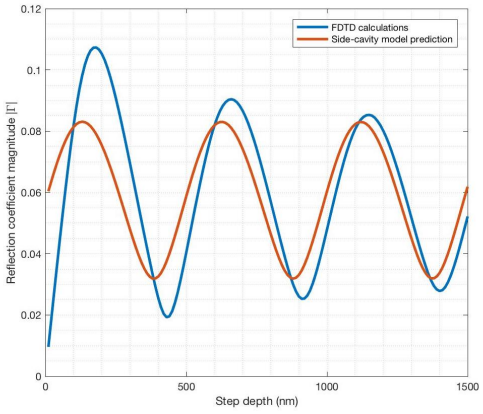


(c) Reflection coefficient magnitude at $\lambda_\circ = 1000\ nm$

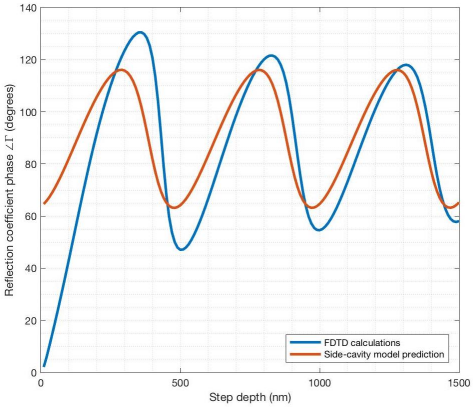


(d) Reflection coefficient phase at $\lambda_\circ = 1000\ nm$

Figure 4.4: Comparison of FDTD data and side-coupled cavity model for the reflection coefficient at step-down discontinuities of different heights (Fig. 4.3) .

the resonance peaks of a depressed step can be readily deduced from the semi-analytically calculated values for open- and short-circuited discontinuities alone; these were the primary topic of Chapter 3. In order to model the reflection parameters of the short- and open-circuited discontinuities, effective medium model and vectorial mode-matching method were used in order; these two approaches were found to provide optimal results for their respective structures. Predicted resonance orders are provided in Fig. 4.5 for the wavelength spectrum of interest. In spite of a minor shift, the discrete orders closely follow the peaks, validating the side-coupling

model of the plasmons. The slight deviations from the predicted peaks can be attributed to the backscattering and reflection of nonmodal field components such as evanescent portion of the diffracted angular spectra and QCWs. The shallow-depth limit of this model has been previously documented by Liu et al. [115].

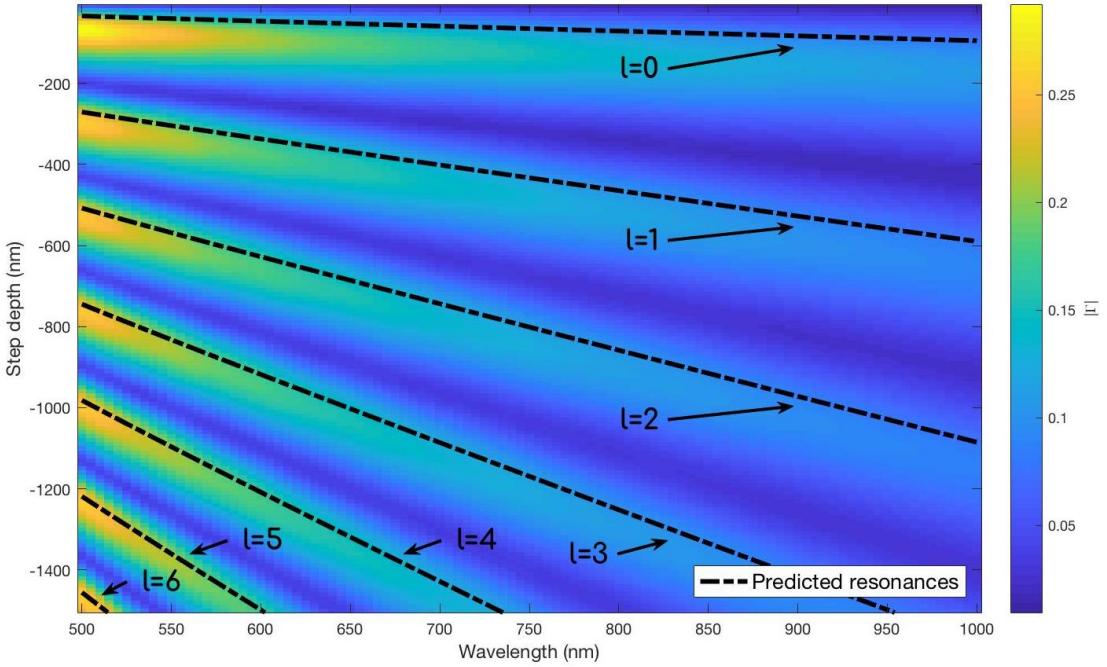


Figure 4.5: Distribution of reflection coefficient magnitudes with respect to free-space wavelengths and step depths for depressed steps (Fig. 4.1a). Analytically-predicted resonance depths for each frequency, as well as the associated resonance orders per Eq. (4.3), are superimposed on the plot.

While the side-coupling-based network model accurately predicts the characteristics of SPP reflection at depressed steps, it fails to accurately capture the analogous case for elevated steps, as covered briefly for the reflection coefficient case. This shortcoming is a consequence of the two main limitations of this approach: (i) the corner discontinuities are approximated strictly as "open-" and "short-circuited" junctions irregardless of the step height, and (ii) electromagnetic interactions at these discontinuities are assumed to be only mediated by side-coupled SPPs. The former limitation can be explained through the effective impedance that the inbound SPP sees at each junction: since the skin depth of plasmonic excitations in

metals is extremely small, the SPP at a depressed step essentially encounters an approximately homogenous dielectric half-space. Thus, the effective impedance at this junction quickly converges that of an "open" termination, even for small step depths (as seen on Figs. 4.4a and 4.4c). Nevertheless, the same case is not applicable for reflection and transmission coefficients of an elevated step. As the penetration depth of SPPs at metals are much more larger, the effective impedance that the SPP first encounters is not that of a shorted termination. Therefore, the actual result very slowly converges to that of the network model, possibly at extreme step heights. In addition, the SPP field in the dielectric encounters the upper corner discontinuity without sufficiently decaying, which provides an additional medium of reflection and transmission through diffraction and scattering.

The diffraction of SPPs at sharp wedges also directly pertains to the latter limitation of the model, which is based on the assumption that resonance is dominated mainly by the interaction of SPPs, rather than other wave constituents. While this approach significantly simplifies the model, QCWs, notable contributors to plasmonic excitations [72], are throughly neglected. Furthermore, in the case of SPP transmission at depressed steps, the diffracted angular spectrum at the upper junction produces a continuum of evanescent and radiative waves, which couples directly to the lower waveguide surface in addition to the side-cavity. This proves to be an auxiliary or even dominant mechanism of SPP transmission and is not covered in the derived model; as a result, the expected periodicity of the transmission coefficient is not as pronounced.

In the case of subwavelength steps that are much smaller than the free-space wavelength of the incident SPP, elevated and depressed steps with the same height or depth ($|h|$) behave almost identically. The limits of this "symmetric" behavior can be approximated by half-power curves around the zero-depth peak, beyond which the transmission coefficient magnitudes slowly begin to diverge from each other. These curves are highlighted in Fig. 4.6; it can also be seen that the almost-symmetric curve around the zero-depth peak broadens with increasing free-space wavelength.

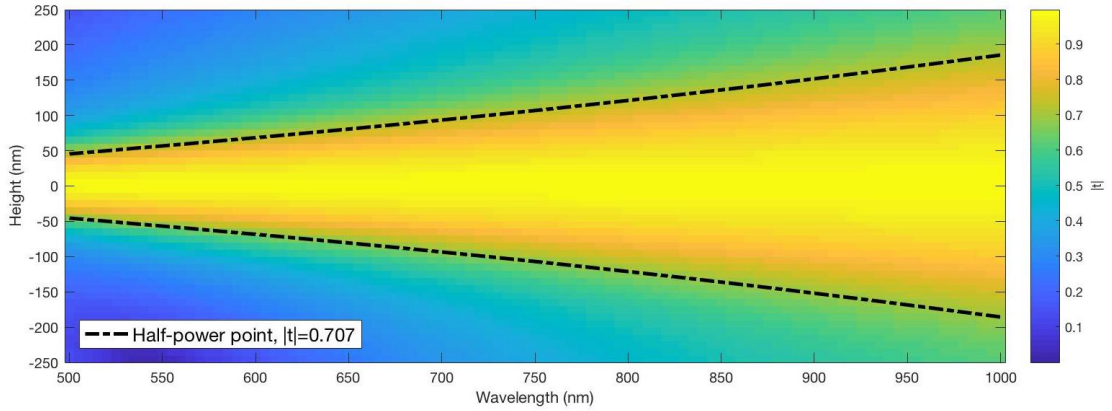


Figure 4.6: Magnitude of the transmission coefficient for subwavelength steps. Half-power curves, which denotes the limits of symmetry, are highlighted.

### *4.1.2 Extinction of SPPs by step discontinuities*

Another figure of merit for SPP interaction is the radiative characteristics of such discontinuities: owing to the nature of these structures as open surface waveguides, a significant portion of the inbound field is expected to decouple and radiate into free-space. As a consequence of the different impedance conditions for the fields impinging on the depressed and elevated steps (Figs. 4.1a and 4.1b), SPP-to-photon conversion is expected to be different for both cases [119]. While the radiated power can be associated with the difference between the unit power and sum of reflectance and transmittance, the resultant value also accounts for the material absorption at the junction, regardless of how minor it is. Thus, for conceptual accuracy, this quantity is named in this thesis as the *SPP extinction* $(1-|\Gamma|^2-|t|^2)$, after a similar cross section parameter in light scattering analysis. The relevant extinction values are provided in Fig. 4.7 for the wavelengths and heights of interest, where little to no extinction or radiation is observed for steps with small $|h|$ and the broadening of the associated low-extinction limit around $|h| = 0$ is noted to be similar to those of the transmission coefficients (Fig. 4.6). For step-down discontinuities, the extinction extrema is inversely correlated with those of the transmission plot, owing to the low-amount of power reflection from these discontinuities. This phenomenon can be exemplified by a particular case of a depressed step with a depth of 250 $nm$,

which showcases a drastic transmission dip for a free-space wavelength of 550 nm (Fig. 4.2). On Fig. 4.7, this exact point corresponds to the local extinction maxima, indicating an efficient level of radiative coupling.

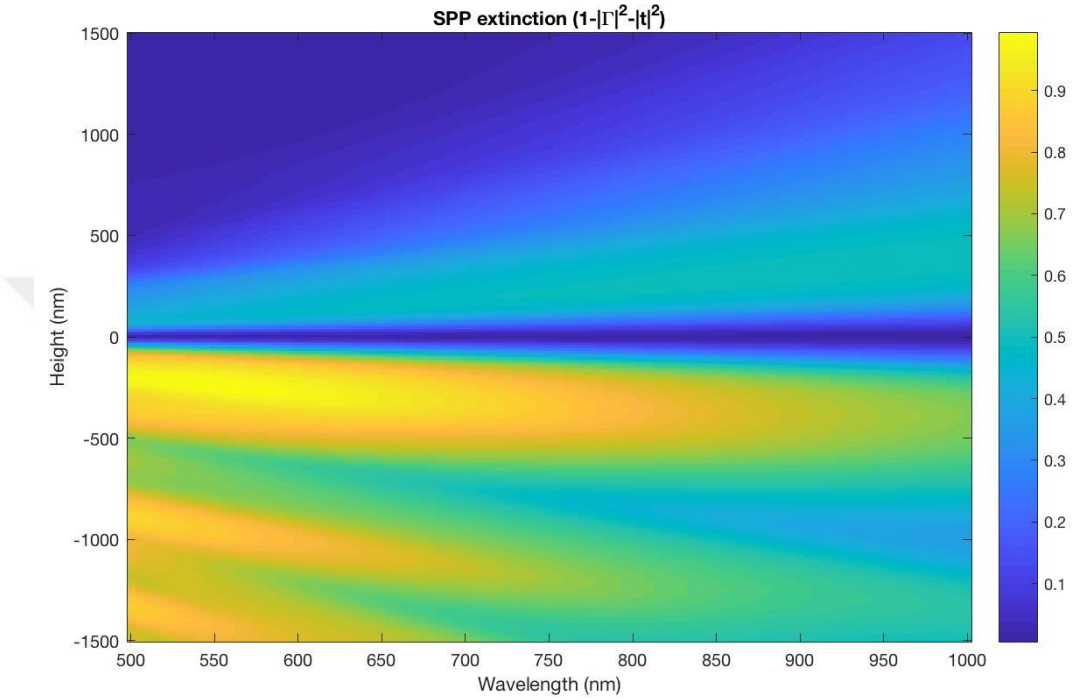


Figure 4.7: SPP extinction at steps with different heights

For step-up discontinuities, the extinctive behavior is more or less similar to the transmission of SPPs in the same structure: the extinction curve, as well as its associated peak is subject to broadening and a quadratic increase with increasing wavelength, respectively (Figs. 4.8a and 4.8b).

## *4.2 Gap discontinuities: metallic grooves and ridges*

Another discontinuities of interest in plasmonics are nanoscale gaps on metallic films, which can be classified into grooves (indentations) and ridges (protrusions), as shown in Figs. 4.9a and 4.9b, respectively. These are used as constituent units of cardinal devices such as plasmonic gratings, which are used to launch SPPs. Thus, such perforations are often analyzed as infinitely periodic structures [120, 121]. The pre-

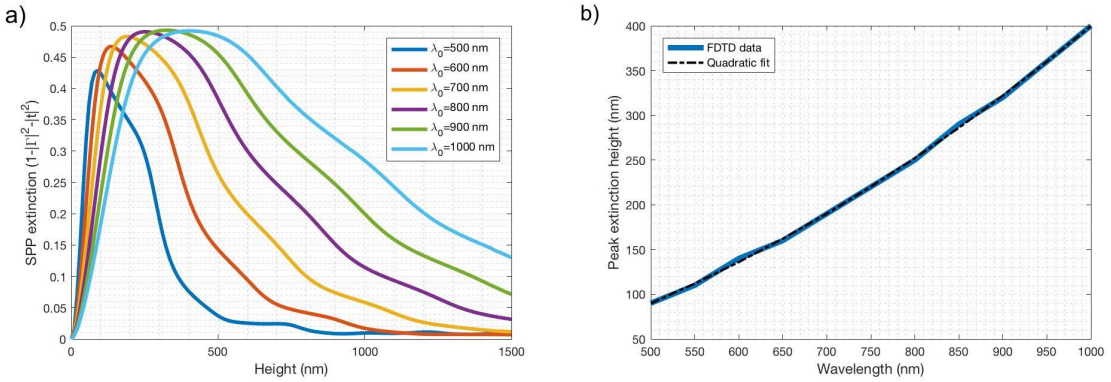


Figure 4.8: SPP extinction for elevated step discontinuities: a) Broadening of extinction curves at different free-space wavelengths, b) Change of extinction peaks vs. free-space wavelength

requisite for modeling the response of such systems is understanding the SPP-groove interaction for solitary units. In past works, scattering from such discontinuities have been studied by method of moments (MoM) or Green's tensor technique [75, 77], which necessitate the calculation of layered-media dyadic Green's functions. Rigorous coupled-wave analysis (RCWA), a popular method in diffractive optics, were also used in the analysis of such structures when periodicity is present [122]. G. Brucoli and L. Martín-Moreno, who extensively studied the reflective, transmissive and radiative properties of the plasmonic gaps [77, 78], have also utilized a more simplified approach that is based on asymptotic analysis: they treated sufficiently shallow ridges and grooves as point dipoles, whose far-field behavior shaped the radiation patterns of the studied structures. While their work cleared up some of the significant loose ends regarding the reflective and transmissive behaviors of solitary and periodic gaps [78], the issue of reflection and transmission phase was largely overlooked.

In this section, the resonant behavior of groove and ridge transfer coefficients will be studied through the side-coupled cavity formalism of the previous section. Equivalent network models for both structures will be provided and response of nanostructure will be reproduced by available approximate models, whenever applicable. Due to a large number of possible configurations that are involved, the FDTD data were obtained for the combinations of widths and heights ranging from

10 to 500 $nm$, with increments of 10 $nm$ for each parameter.

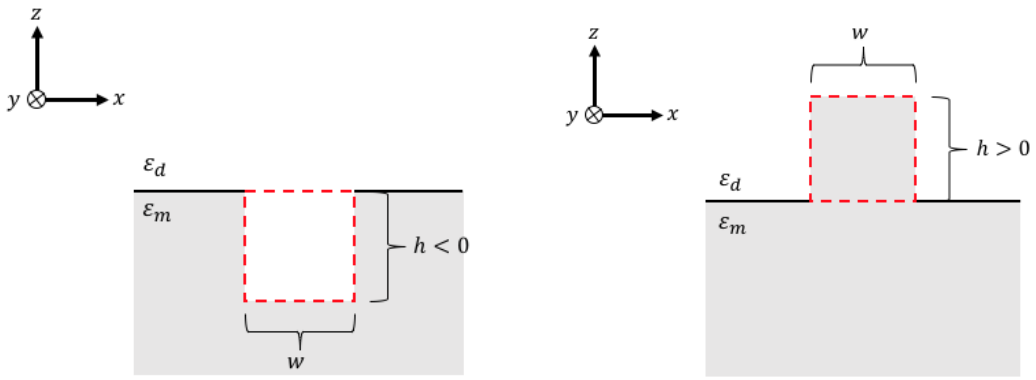


(a) Groove discontinuity (b) Ridge discontinuity

Figure 4.9: Typical gap discontinuities. (a) Groove and (b) Ridge with widths of $w$ and heights/depths of $h$.

### *4.2.1 Cavity model for grooves*

Side-coupled cavity model was originally conceived to describe the interaction of SPPs with etched grooves [114]. While the perforation can be thought of as a vertically-positioned MIM cavity as in Fig. 4.10, the ensuing network topology is radically different from that of the step case. As the cavity is able to support two distinct modes, namely the symmetric and anti-symmetric modes, the whole groove is represented by a 4-port network, given in Fig. 4.10. First and second ports represent the connections to the main single-interface waveguides on both sides of the groove with characteristic impedance of $Z_0^{MI}$ and propagation constant of $\beta^{MI}$, while the remaining ports account for the modal interactions within the cavity, with third and fourth ports representing the symmetric and anti-symmetric SPPs, respectively. For each mode, the corresponding cavity is cascaded with a transmission line of the groove depth $h$; the propagation constants and characteristic impedances of the lines are distinct and dependent on the groove width, designated by $\beta^{a,s}(\mathrm{w})$ and $Z_0^{a,s}(\mathrm{w})$ where the superscripts $a$ and $s$ are for anti-symmetric and symmetric cases, respectively. Since the coupled SPP in the cavity interacts with

the effectively short-circuited termination in the form of an impedance boundary, both ports are terminated with an equivalent complex load.

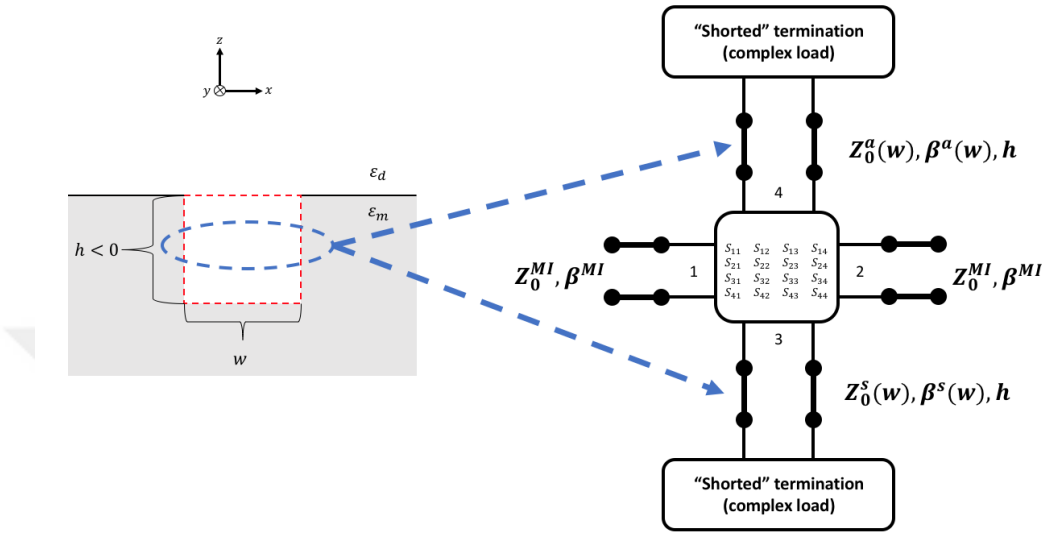


Figure 4.10: Equivalent 4-port network for a groove discontinuity with a height $h$ and width $w$.

The corresponding S-parameters for the 4-port network are provided in Eq. (4.4). In this network representation, the 2-by-2 matrix on the upper left corresponds to the reflection and transmission coefficients that result from the direct tunneling of the incoming SPP mode in between the groove end-faces. The upper right and lower left 2-by-2 matrices represent the coupling from and to the cavity modes, respectively. Due to the mirror symmetry of the gap, intercoupling between symmetric and anti-symmetric modes at the upper end of the groove is non-existent [115]: thus, $S_{34}$ and $S_{43}$ parameters on the matrix diagonal, which represent intermodal coupling between these MIM modes, are essentially zero. As in the case for traditional microwave networks, these scattering parameters can be obtained from matching unused ports with their characteristic impedances and seeking out the steady-state responses from only the sought ports. A few examples for some of the involved physical phenomena and their corresponding scattering coefficients can be provided on Fig. 4.11; while these examples only pertain to the symmetric MIM modes in the gap, they are also

equally valid for the anti-symmetric modes. In this context, matching refers to the extension of the waveguide to the infinity, which was performed on the ports for the gap modes; thus, the individual scattering responses of the system, i.e. the direct SPP tunneling at the gap without any back-reflection from the bottom of the groove, can be extracted [115].

$$S_{\text{groove}} = \begin{bmatrix} S_{11} & S_{12} & S_{13} & S_{14} \\ S_{21} & S_{22} & S_{23} & S_{24} \\ S_{31} & S_{32} & S_{33} & S_{34} \\ S_{41} & S_{42} & S_{43} & S_{44} \end{bmatrix} = \begin{bmatrix} \Gamma_{11} & t_{12} & S_{13} & S_{14} \\ t_{21} & \Gamma_{22} & S_{23} & S_{24} \\ S_{31} & S_{32} & \Gamma_d^s & 0 \\ S_{41} & S_{42} & 0 & \Gamma_d^a \end{bmatrix} \tag{4.4}$$

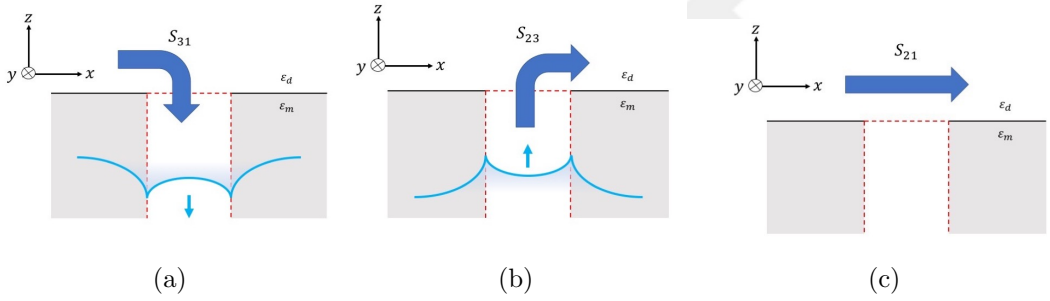


(a) (b) (c)

Figure 4.11: Examples of scattering parameters for the metallic groove: a) $S_{31}$, transmission from main SPP mode to symmetric MIM mode; b) $S_{23}$, transmission from symmetric MIM mode to main SPP mode; c) $S_{23}$, direct SPP transmission across the gap (tunneling).

Invoking the interference condition in Eq. (4.3), the resonant behavior of coupled SPPs in the multi-modal cavity can be summarized into two distinct conditions:

$$\begin{aligned} l2\pi &= 2Re[\beta^s_{\text{MIM}}]h + \angle\Gamma^s_d + \angle\Gamma^s_m \quad \text{(Symmetric mode)} \\ l2\pi &= 2Re[\beta^a_{\text{MIM}}]h + \angle\Gamma^a_d + \angle\Gamma^a_m \quad \text{(Anti-symmetric mode)} \end{aligned} \tag{4.5}$$

where $l$ is the discrete resonance order, and $\Gamma^{a,s}_m$ and $\Gamma^{a,s}_d$ are the reflection coefficients of the short- and open-circuited cavity terminations, respectively; the superscripts $s$ and $a$ denote symmetric and anti-symmetric modes. In the study by Liu et al., the simultaneous satisfaction of these two conditions is interpreted to cause reflection resonances and transmission anti-resonances, since both cases coincide with the

symmetric and/or anti-symmetric MIM resonances in the nanocavity. As the fields that resonate within the cavity couple back to the metal-insulator surface, they constructively interfere with the fields that are directly reflected from the gap ($S_{11}$ and $S_{22}$). Similarly, they destructively interfere with the fields that directly tunnel to the other end of the gap ($S_{12}$ and $S_{21}$) [115].

Since anti-symmetric MIM modes exist only for certain groove widths, resonant and anti-resonant curves on the transfer coefficient plots may be ascribed to a particular dominant modal behavior [115], which can be observed in Fig. 4.12 for a free-space wavelength of 500 $nm$. Using Eqs. (4.5), the resonance curves were computed numerically with the short- and open-circuited discontinuity models in Chapter 3. Due to the absence of propagating anti-symmetric modes for shorter groove widths, symmetric modes dominate the corresponding behavior. As the width goes beyond a value that permits the excitation such propagating modes, anti-symmetric fields begin to influence the curves. Additionally, the increasing groove depth is associated with higher-order Fabry-Pérot resonances. Nevertheless, the zeroth order anti-symmetric resonances in Figs. 4.12a and 4.12b do not align perfectly; this can be attributed to the co-excitation of both modal components.

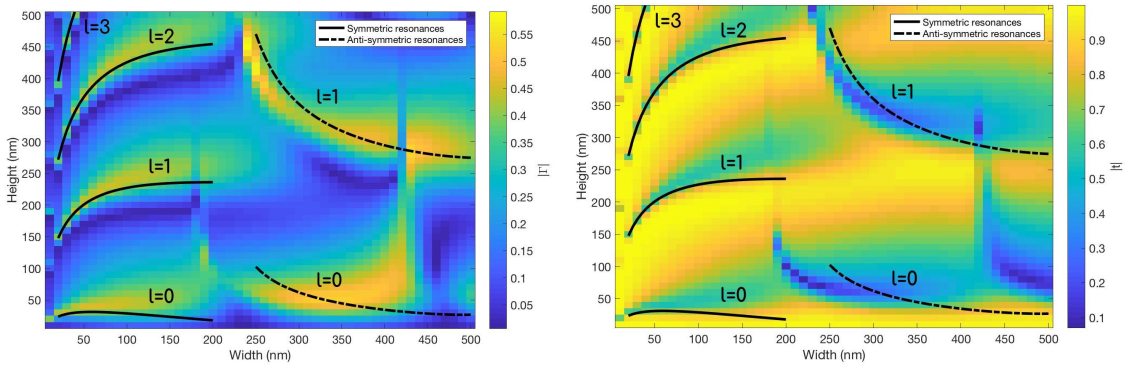


(a) Reflection coefficient magnitude

(b) Transmission coefficient magnitude

Figure 4.12: Magnitudes of (a) reflection and (b) transmission coefficients from the FDTD data, as a function of groove width and height at $\lambda_0 = 500\ nm$. The straight and dashed lines correspond to numerically-calculated resonances of symmetric and anti-symmetric MIM modes from Eq. (4.5), respectively.

A similar resonant behavior can also be observed for the SPP extinction (1 −

$|\Gamma|^2 - |t|^2$) at the groove, which is shown in Fig. 4.13. Different resonance orders, denoted by $l$, exhibit strong extinctive and by extension, radiative properties. The maximal peaks at larger widths suggest that contribution of anti-symmetric modes is an aggravating factor for the radiation intensity. Nevertheless, the absolute peak extinction rate, observed for a groove width of 460 nm and height of 90 nm, is not captured by the curves.

For the sake of brevity, total reflection coefficients were not reproduced, since these necessitated further FDTD simulations for modal-intercoupling in between single and multi-interface waveguides, which were beyond the scope of this thesis. Readers are referred to the extensive study by Liu et al. [115], which reports the appropriate results.

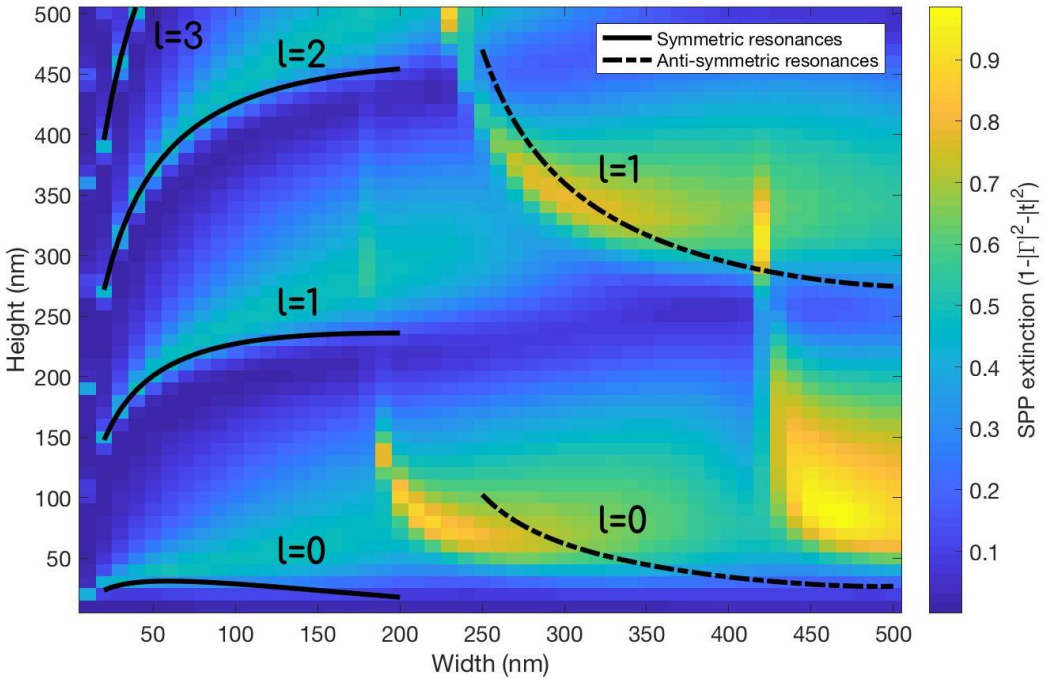


Figure 4.13: SPP extinction as calculated from the FDTD data, as a function of groove width and height at $\lambda_0 = 500\ nm$. The straight and dashed lines correspond to numerically-calculated resonances of symmetric and anti-symmetric MIM modes, respectively.

Based on the observations in Fig. 4.12 and Fig. 4.13, while the model offers close predictions of the SPP resonances in moderate yet subwavelength dimensions, it

fails accurately represent the surface wave behavior in the wide groove limit [115]; this can be attributed to the diffractive effects that hindered the performance of the network model for step discontinuities.

### *4.2.2 Cavity model for ridges*

Side-coupled cavity model can also be employed to deduce the transfer coefficients of ridges or indentations. While the original model for grooves warrant that the ridge should be dissected into a 4-port network, a simpler and more intuitive approach can be employed by considering the ridge as a laterally-positioned Fabry-Pérot cavity. In this model, the step discontinuities themselves are modeled as effective cavity boundaries with height-dependent transfer functions. This reduces down the computational burden of calculating the propagation constants and reflection coefficients for two different cavity modes for IMI structures, the long- and short-range modes. While this approach was previously employed by K. Ozawa and N. Yamamoto [123], their work relied upon the data-fitting of transfer functions for steps. Since a complete set of effective models for step transfer coefficients is not readily available, FDTD data for step discontinuities will be used in this section instead.

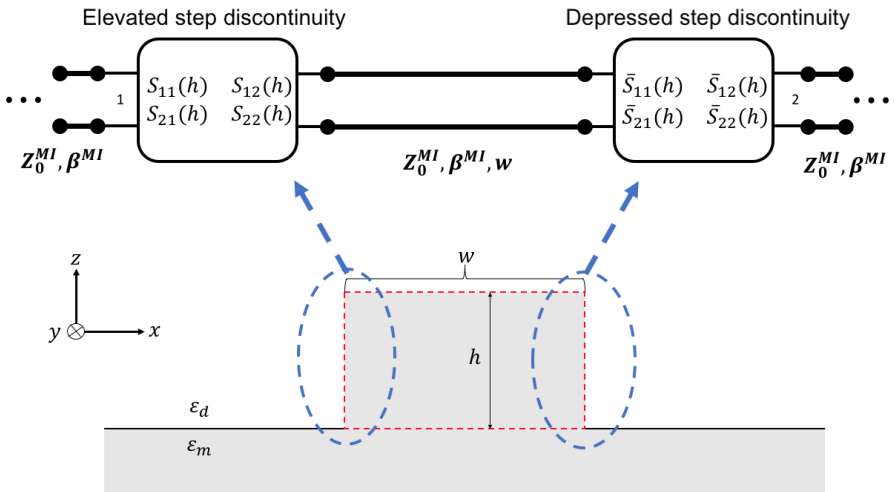


Figure 4.14: Equivalent network for a ridge discontinuity

The equivalent network for this structure is given in Fig. 4.14, and the model

parameters closely resembles those of the step discontinuities in Eqs. 4.1. The only difference stems from the fact that S-parameters here are functions of the ridge height $h$. Similar to the previous cases, the resonance condition can be stated as

$$l2\pi = 2Re[\beta]\mathrm{w} + \angle S_{22}(\mathrm{h}) + \angle \overline{S}_{11}(\mathrm{h}) \tag{4.6}$$

where $l$ is the resonance order, $w$ is the ridge width, and $S_{22}(\mathrm{w})$ and $\overline{S}_{11}(\mathrm{w})$ are the reflection coefficients for elevated and depressed steps, respectively. The resulting network model yields the cumulative reflection ($\Gamma_{ridge}$) and transmission ($t_{ridge}$) expressions:

$$\begin{aligned} \Gamma_{ridge}(w,h) &= S_{11}(h) + \frac{S_{21}(h)S_{12}(h)\overline{S}_{11}(h)e^{i\beta 2w}}{1 - S_{22}(h)\overline{S}_{11}(h)e^{i\beta 2w}} \\ t_{ridge}(w,h) &= \frac{S_{21}(h)\overline{S}_{21}(h)e^{i\beta w}}{1 - S_{22}(h)\overline{S}_{11}(h)e^{i\beta 2w}} \end{aligned} \tag{4.7}$$

Comparisons of reflection and transmission coefficients obtained by the side-coupled cavity model and the FDTD simulations are provided in Figs. 4.15 to 4.17 at the reference wavelength of 630 $nm$. In terms of the magnitude and phase of the reflection coefficients in Fig. 4.15, the model showcases a very close agreement with the actual FDTD results, except for very small ridge widths, where tunneling effects are expected to dominate. The same properties were observed for SPPs at different wavelengths in the range of 500 to 1000 nms. In addition, resonances of the lateral cavity along the ridge, i.e., along the width of the ridge $w$, can be observed through the periodicity of the magnitudes and phases with respect to the structure width. Those resonances, calculated via Eq. (4.6) and predicted by the cavity model itself, coincide with the localized magnitude dips and accompanying lineshape broadenings, as seen in Fig. 4.16 at the reference wavelength.

While the cavity model offers good agreement in the reflection coefficient results as compared to the FDTD simulations, its performance on the prediction of transmission coefficient is relatively poor, albeit still within acceptable range (Fig. 4.17). For this particular ridge structure and dielectric function, deviations from the actual results are much more apparent as the ridge height surpasses a quarter of the incident SPP wavelength for a fixed width: the model converges much more rapidly to the zero transmission limit, while the phase shifts drastically.

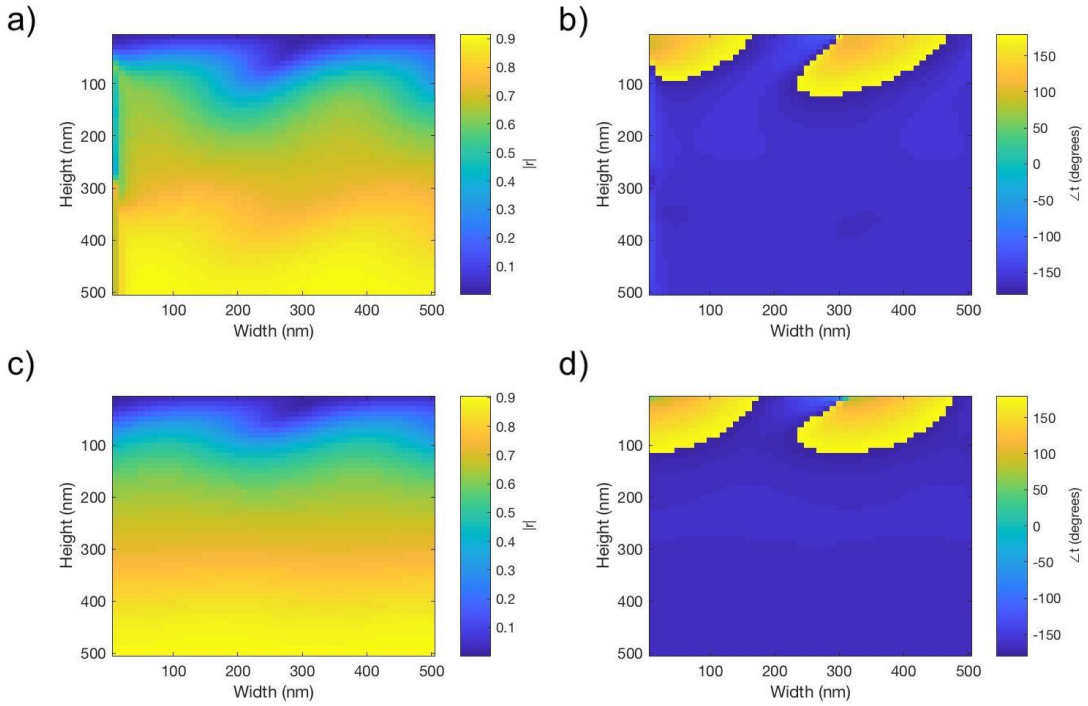


Figure 4.15: Reflection coefficients for the SPP from the ridges with different widths and heights at $\lambda_\circ = 630\ nm$, Fig. 4.14: a) Magnitude (FDTD), b) Phase (FDTD), c) Magnitude (model), d) Phase (model).

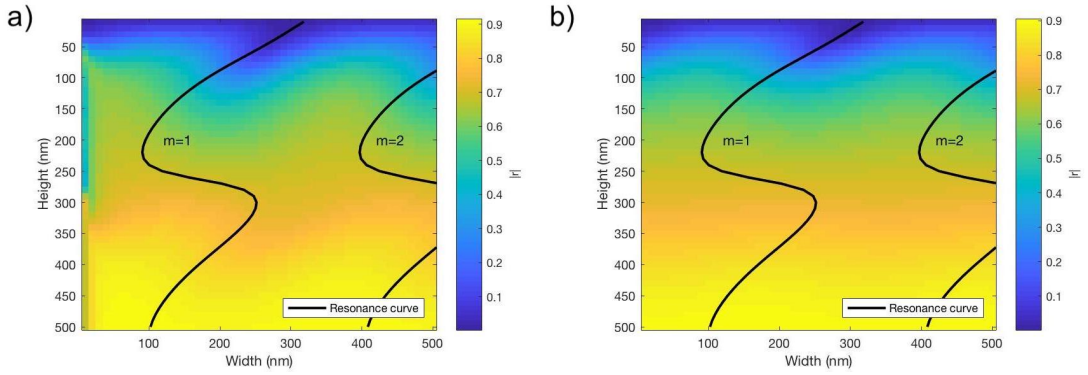


Figure 4.16: Magnitudes of the reflection coefficients for the SPP from ridges, with different widths and heights at $\lambda_\circ = 630\ nm$, along with the resonance curves: a) FDTD results, b) Network model.

As a result of the relatively subpar performance of the transmission model, extinction plot, as shown in Fig. 4.18, showcases deviations from the FDTD data, albeit

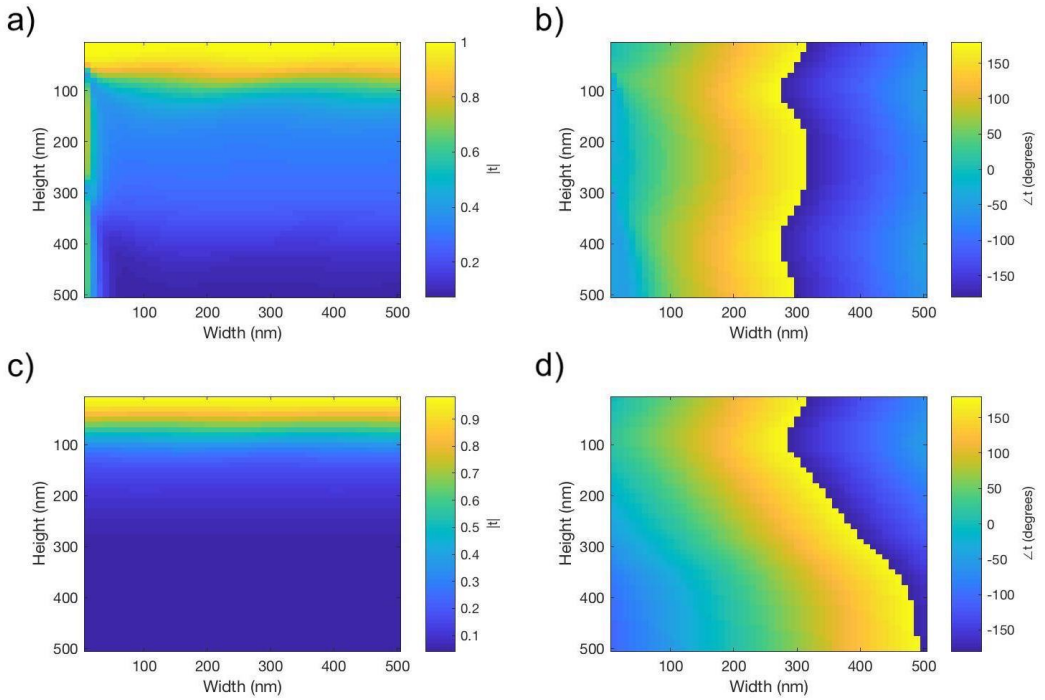


Figure 4.17: Transmission coefficients for the SPP from the ridges with different widths and heights at $\lambda_\circ = 630\ nm$, Fig. 4.14: a) Magnitude (FDTD), b) Phase (FDTD), c) Magnitude (model), d) Phase (model).

still maintaining the salient extinctive features of the structure. It fails to account for the thin-ridge limit and overestimates broadening of the radiative resonances. The adjacent extinctive peaks roughly correspond to half of the SPP wavelength ($\lambda_{\mathrm{SPP}}$), indicating the effects of resonant light scattering from the ridge.

*Thin-ridge limit for resonances*

As observed in Figs. 4.15-4.18, the side-coupled network model in Fig. 4.14 fails to represent the behavior of very thin ridges with thicknesses within a few orders of the SPP skin depth. This result is expected, as the inbound surface wave can sufficiently penetrate the protrusion to tunnel efficiently. Thus, as in the case for the etched indentations, the discontinuity functions as a three-layered cavity that supports IMI modes. Excitation and resonance of these modal components can be shown to guide the response of such subwavelength structures.

A close-up of the reflection, transmission and extinction parameters of a ridge

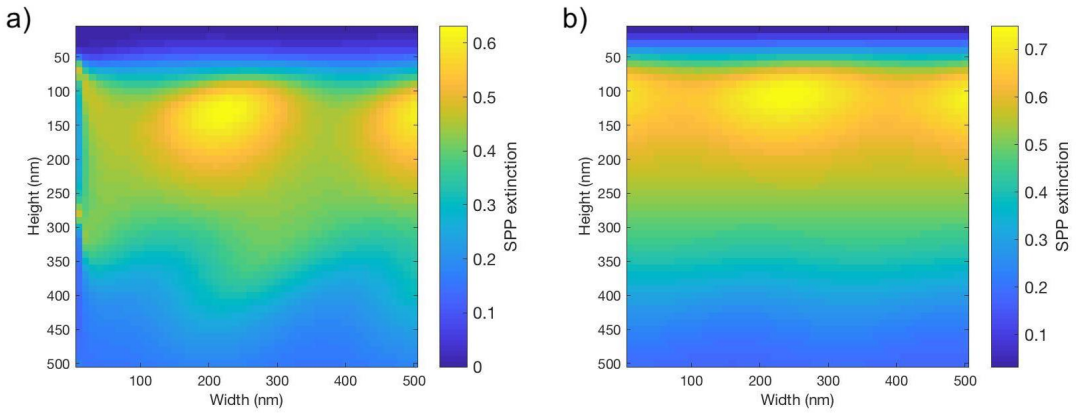


Figure 4.18: SPP extinction rate for the ridges with different widths and heights at $\lambda_\circ = 630\ nm$: a) FDTD results; b) Network model

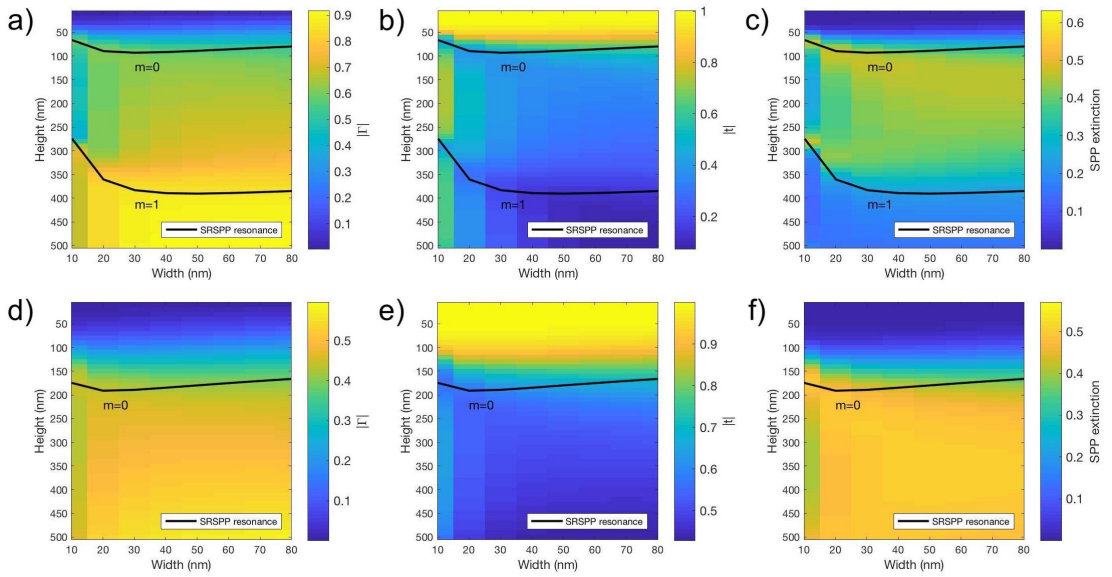


Figure 4.19: Close-up of reflection, transmission and extinction of a ridge within small-width limits, along with the SRSPP modes: a) Reflection coefficient magnitude, $\lambda_\circ$=630 $nm$; b) Transmission coefficient magnitude, $\lambda_\circ$=630 $nm$; c) SPP extinction rate, $\lambda_\circ$=630 $nm$; d) Reflection coefficient magnitude, $\lambda_\circ$=1000 $nm$; e) Transmission coefficient magnitude, $\lambda_\circ$=1000 $nm$; f) SPP extinction rate, $\lambda_\circ$=1000 $nm$.

within the small-width limit is provided in Fig. 4.19 for the free-space wavelengths of 630 $nm$ and 1000 $nm$. It can be observed that small-scale resonances in the reflection coefficient magnitude and the extinction rate follow the approximately-calculated zeroth- and first-order resonances for the SRSPP modes. Furthermore,

these curves also correspond to local anti-resonances of the transmission coefficients. The results strongly indicate that in the small-width limit, SRSPPs, despite being harder to excite compared to LRSPPs, guide the transfer behavior. In addition, it can also be suggested that the scattered fields and these resonances destructively interfere with the tunneled SPP components, since the SRSPP resonance orders closely follow the local transmission dips at this limit, as seen in Figs. 4.19b and 4.19e.

## *4.3 Conclusion and summary*

Plasmonic nanostructures such as gratings and nano-antennas feature either solitary or periodic arrangements of two dimensional discontinuities such as ridges and grooves to manipulate the excitation and/or propagation of SPPs. The key to understanding and designing these structures lies in the application of intuitive models to efficiently describe the surface wave interaction. Building upon the approximate models for "open-" and "short-circuited," wedge-type terminations in Chapter 3, this section featured the derivation and analysis of network- and cavity-based models to explain the resonant behavior of reflection, transmission and extinction on more complex yet fundamental plasmonics junctions. Steps, ridges and grooves on single-interface plasmonic waveguides were characterized through analogous transmission-line models, with reproduction of either the FDTD data or the resonance curves being the primary objective. For ridges and grooves, effects of coupled SPP modes on the resonant behavior were investigated.

# Chapter 5

# CONCLUSION AND FUTURE WORK

This thesis covered the interaction of surface plasmon polaritons with 2D discontinuities within a reflection and transmission formalism, for which the efficient methods to recover and generalize these parameters were studied.

The second chapter of this thesis focused on the electromagnetic background of plasmonics. In order to provide a comprehensive introduction on the field, fundamental equations that govern plasmonic phenomenona were derived step-by-step from Maxwell's equations and their associated boundary conditions. These phenomenona were grouped into surface plasmon polaritons (SPPs) and localized surface plasmons (LSPs), former of which is the primary topic of this thesis. Since SPPs are inherently associated with layered media, Fresnel and generalized reflection coefficients (GRC) were also introduced. Different modes on single- and multi-layered plasmonic structures were studied. Optical properties of metals, which facilitate the light-metal excitations on surfaces, were also reviewed.

The focal point of the third chapter was the SPP reflection from one of the most basic form of discontinuities, termination of single-layered metallo-dielectric waveguides with dielectric or metallic half-spaces. As a physical analogy with their counterparts in RF transmission line theory, these two types of terminations were categorized as "open-circuited" (dielectric) and "short-circuited" (metallic) discontinuities. As a prerequisite for evaluation of such junctions, foundations of finite-difference time-domain (FDTD) method, primary simulation technique that was employed throughout this thesis, were established. Since a strong numerical tool necessitates an equally-competent post-processing technique for modal analysis of the results, two candidate methods, namely the generalized pencil-of-function (GPOF) and eigenmode expansion (EME), were compared with each other through possible test cases. Following the establishment of necessary tools, effective medium, surface-impedance

and mode-matching based reflection models were developed and their applicabilities were comparatively studied. While all featured models were found to accurately represent the inductive nature of short-circuited terminations, only the mode-matching approach proved to be adequately applicable for the open-circuited case. To further validate the applicability of these models, their performance was demonstrated on a simple test case on the SPP tunneling from a semi-infinite impedance barrier.

In the fourth chapter, step- and gap-type discontinuities on metallo-dielectric surfaces were studied. Due to the involvement of more complex diffraction and refraction phenomena in the interaction of SPPs with such structures, intricate network- and transmission line-based approaches were employed for approximate models. A depressed step discontinuity was observed to behave as a nanocavity, with the reflection coefficient closely following that of a Fabry-Pérot etalon in terms of magnitude and phase. Being grouped into indentations and protrusions, the gap discontinuities were characterized by their cavity resonances that result from the SPP edge-coupling. Based on these models, extrema in SPP reflectances and transmittances were associated along the lateral dimensions of these gaps. The limits of the developed models were throughly assessed.

Even though EME was chosen as the primary post-processing subroutine in this thesis, the generalized pencil-of-function (GPOF) method has been assessed to offer favorable results regarding the complex wave amplitudes: in the past work, it has also been successfully used to recover scattering parameters of microwave waveguides from the FDTD data [124]. Considerable further research is needed to develop this method into a generalized and robust modal analysis tool for optical applications, especially for cases in which the dispersion relation can be enforced analytically, as in the case for SPPs.

Another possible topic of future study is further improvement of approximate discontinuity models that were studied in this thesis, as well as derivation of appropriate and meaningful transmission coefficients at the terminations: while models on SPP generation at plasmonic slits are available in optics literature [72, 73, 74], they lack expressions regarding transmission magnitudes and phases. Based on the performances of approximate reflection coefficients in conjunction with the network

models for steps and gaps, an approximate transmission coefficient is the missing step towards the realization of a full-scale, generalizable model for canonical discontinuities. Variational methods based on equivalence principle [125, 126], aperture theory [127] and/or geometrical theory of diffraction [128] may offer promising paths towards the improvement of such approaches. The resulting reflection and transmission data can be used in the realization of robust circuit models via network synthesis tools such as vector-fitting method [129]. Deduction of reflection and transmission coefficients of multiple cascaded scatterers, as well as those of hybrid metallo-dielectric structures (i.e. air-Si-Ag waveguides) can also be ideated as a possible extension of this study.

# Appendix A

# DISCRETE DIPOLE MODEL FOR PLASMONIC NANOCHAINS

In discrete-dipole approximation (DDA), the scatterer is approximated as a finite collection of individual dipoles that are coupled to each other, akin to the distinct atoms that constitute a dielectric medium. These dipoles are polarized in a similar manner to how the dielectric medium itself is polarized by an inbound electric field; each polarization of the individiual dipole is dependent on the other ones and the source field, which is often a plane wave. Thus, the resulting scattered field and cross section can be determined by ease from the dipole moments [60]. In order to provide a basis for this formulation, the general light scattering from an arbitrary material body can be written as a volume-integral equation [130]:

$$\mathbf{E}(r) = \mathbf{E}^{inc}(r) + \int_V \overline{\mathbf{G}}(r, r')\mathbf{E}(r')\chi(r')dr'^3 \tag{A.1}$$

where $\overline{\mathbf{G}}(r, r')$ is the dyadic Green's function for electric field while $\chi(r')$ corresponds to the space-dependent susceptibility of the scatterer. This equation illustrates the full picture of the scattering within the limits of classical electrodynamics: each infinitesimal element of the scatterer is treated as a radiation source that is dependent on the incident field and other elements. DDA essentially approximates the continuous scattering medium with a finite number of radiating dipoles. Reconsidering the problem within this framework, the total electric field resulting from a finite number of identical elements can be expressed as:

$$\mathbf{E}_n = \mathbf{E}_n^{inc} + \sum_{n \neq m} \overline{\mathbf{G}}_{nm}\mathbf{E}_m\alpha_m(\omega) \tag{A.2}$$

In this formula, $\alpha_m(\omega)$ refers to the polarizability of the dipole $m$, which is usually denoted by the Clausius-Mossotti relation in conjunction with the radiation

damping force [60], which was provided on Eq. (2.55):

$$\frac{1}{\alpha_r(\omega)} = \left[4\pi\varepsilon_0 \left(\frac{\varepsilon(\omega)-1}{\varepsilon(\omega)+2}\right) a^3\right]^{-1} - i\frac{\omega^3}{6\pi\varepsilon_0 c^3} \tag{A.3}$$

This polarizability essentially links the volumetric susceptibility of the medium with the dipole moments. The radiation damping component is included to cover the dipole's reaction to the radiation via charge acceleration; for LSP excitations in MNPs with a radius larger than 20 nm, the effect is non-negligible and broadens the plasmon linewidth [56].

For free-space, dyadic Green's function reduces down to the simple Hertzian dipole expression. As a result, an electric field of a Hertzian dipole with a moment of $\mathbf{p}$ can be written as [53]:

$$\mathbf{E}(\mathbf{r},t) = \frac{1}{4\pi\varepsilon_0}\left[\left(1-\frac{i\omega r}{c}\right)\frac{3\hat{\mathbf{r}}\cdot\mathbf{p}\hat{\mathbf{r}}-\mathbf{p}}{r^3} + \frac{\omega^2}{c^2}\frac{\mathbf{p}-\hat{\mathbf{r}}\cdot\mathbf{p}\hat{\mathbf{r}}}{r}\right] e^{i\frac{\omega r}{c}} \tag{A.4}$$

On Weber and Ford's formulation of the discrete-dipole model [56], the dipoles are linearly ordered along the $\hat{\mathbf{r}}$ vector and the inter-dipole spacing is fixed to $d$. Reappropriating (A.4) with the induced dipole moment relation ($\mathbf{p} = \alpha\mathbf{E}$) for an arbitrary number of coupled dipoles, we obtain:

$$\begin{aligned}\mathbf{p}_n =& \alpha_r(\omega)\sum_{m\neq n}\frac{1}{4\pi\varepsilon_0}\left[\left(1-\frac{i\omega|n-m|d}{c}\right)\frac{3\hat{\mathbf{r}}\cdot\mathbf{p}_m\hat{\mathbf{r}}-\mathbf{p}_m}{|n-m|^3d^3}\right.\\ &\left.+\frac{\omega^2}{c^2}\frac{\mathbf{p}_m-\hat{\mathbf{r}}\cdot\mathbf{p}_m\hat{\mathbf{r}}}{|n-m|d}\right] e^{i\omega|n-m|d/c}\end{aligned} \tag{A.5}$$

Eq. (A.5) describes the moment of the nth dipole; the unit vector $\hat{\mathbf{r}}$ points in the direction of the chain. The normal modes or *eigenfunctions* of the system can be assumed to be in the form $\mathbf{p}_n \propto e^{inkd}$, which indicates travelling waves. The polarization $\mathbf{p}_n$ can take on two different and orthogonal forms: *transverse* and *longitudinal polarizations*, which are perpendicular ($\mathbf{p}_n \perp \hat{\mathbf{r}}$) and parallel to the direction of chain ($\mathbf{p}_n \parallel \hat{\mathbf{r}}$), respectively. As a result, (A.5) reduces down to their respective equations, (A.6) and (A.7).

$$\begin{aligned}\mathbf{p}_n =& \alpha_r(\omega)\sum_{m\neq n}\frac{1}{4\pi\varepsilon_0}\left[\left(1-\frac{i\omega|n-m|d}{c}\right)\frac{-\mathbf{p}_m}{|n-m|^3d^3}\right.\\ &\left.+\frac{\omega^2}{c^2}\frac{\mathbf{p}_m}{|n-m|d}\right] e^{i\omega|n-m|d/c}\end{aligned} \tag{A.6}$$

$$\mathbf{p}_n = \alpha_r(\omega) \sum_{m \neq n} \frac{1}{4\pi\varepsilon_0} \left[ \left( 1 - \frac{i\omega|n-m|d}{c} \right) \frac{2\mathbf{p}_m}{|n-m|^3 d^3} \right] e^{i\omega|n-m|\frac{d}{c}} \tag{A.7}$$

### *A.1 Finite nanochains*

For a chain with finite number of MNPs, a system of coupled linear equations can be derived. Thus, the coupled dipole identity in (A.6) can be converted to a matrix equation in the form $M\hat{p} = v$.

For a system with $N$ dipoles, the coupling relation can be written as [56]:

$$\begin{bmatrix} p_1 \\ \vdots \\ p_N \end{bmatrix} = \alpha(\omega) \left( \begin{bmatrix} G_{11} & \dots & G_{1N} \\ \vdots & \ddots & \vdots \\ G_{N1} & \dots & G_{NN} \end{bmatrix} \begin{bmatrix} p_1 \\ \vdots \\ p_N \end{bmatrix} + \begin{bmatrix} E_1^d \\ \vdots \\ E_N^d \end{bmatrix} \right) \tag{A.8}$$

In (A.8), $\mathbf{p}$ and $\mathbf{E^d}$ vectors represent the polarization and input driving electric field for each dipole, respectively. $\overline{\mathbf{G}}$ matrix represents the coupling matrix that links the each dipole moment with the other ones; as a result, its diagonal is zero. Rearranging the formulation, we can write:

$$\frac{1}{\alpha(\omega)} \begin{bmatrix} p_1 \\ \vdots \\ p_N \end{bmatrix} - \begin{bmatrix} G_{11} & \dots & G_{1N} \\ \vdots & \ddots & \vdots \\ G_{N1} & \dots & G_{NN} \end{bmatrix} \begin{bmatrix} p_1 \\ \vdots \\ p_N \end{bmatrix} = \begin{bmatrix} E_1^d \\ \vdots \\ E_N^d \end{bmatrix} \tag{A.9}$$

The first polarization vector in (A.9) can be expanded with identity matrix. A new coupling matrix $\overline{\mathbf{M}}$ can be defined by using the distributivity property in matrix algebra; since the coupling matrix $\overline{\mathbf{G}}$ already has zero diagonals, the new matrix will only differ by those values and the overall sign:

$$\underbrace{\begin{bmatrix} \frac{1}{\alpha(\omega)} & \dots & -G_{1N} \\ \vdots & \ddots & \vdots \\ -G_{N1} & \dots & \frac{1}{\alpha(\omega)} \end{bmatrix}}_{\overline{\mathbf{M}}} \begin{bmatrix} p_1 \\ \vdots \\ p_N \end{bmatrix} = \begin{bmatrix} E_1^d \\ \vdots \\ E_N^d \end{bmatrix} \tag{A.10}$$

Thus, the elements of the coupling matrix can be written as:

$$\begin{aligned}
\overline{\mathbf{M}}_{nm} &= \frac{a^3}{\alpha(\omega)}, \quad (m=n) \\
\overline{\mathbf{M}}_{nm} &= \frac{a^3}{4\pi\varepsilon_0 d^3}\left(1-\frac{i\omega|n-m|d}{c}-\frac{\omega^2|n-m|^2d^2}{c^2}\right) \\
&\quad\times\frac{e^{i\omega|n-m|d/c}}{|n-m|^3}, \quad (\text{transverse}, m\neq n) \\
\overline{\mathbf{M}}_{nm} &= \frac{-2a^3}{4\pi\varepsilon_0 d^3}\left(1-\frac{i\omega|n-m|d}{c}\right)\frac{e^{i\omega|n-m|d/c}}{|n-m|^3}, \quad (\text{longitudinal}, m\neq n)
\end{aligned} \tag{A.11}$$

The eigenvectors of this matrix yield the characteristic modes of the nanochain. Noting that the dispersion relation falls in the complex $\beta-\omega$ space due to temporal and intrinsic losses, the actual SP wavevectors are also expected to be complex [63]. These can be obtained through the GPOF analysis of the eigenvectors: the corresponding results were reported on Figs. 2.15a and 2.15b.

## *A.2 Infinite nanochains*

Another theoretically-important case is the infinitely-stacked nanochain, whose characteristic dispersion equation can be derived through the application of infinite series on the polarization identities on (A.6) and (A.7) [56]. These expressions are provided in this section for transverse and longitudinal excitations.

### *A.2.1 Transverse excitation*

For transverse excitation, Eq. (A.6) can be rewritten by substituting the polarization terms with the travelling wave expression ($e^{iknd}$):

$$\begin{aligned}
e^{iknd} =& \alpha(\omega)\sum_{m\neq n}\frac{1}{4\pi\varepsilon_0}\left[\left(1-\frac{i\omega|n-m|d}{c}\right)\frac{-e^{ikmd}}{|n-m|^3d^3}\right. \\
&\left.+\frac{\omega^2}{c^2}\frac{e^{ikmd}}{|n-m|d}\right]e^{i\omega|n-m|d/c}
\end{aligned} \tag{A.12}$$

Eq. (A.12) can alternatively be expressed as:

$$\begin{aligned}
1 =& -\frac{\alpha(\omega)}{d^3}\frac{1}{4\pi\varepsilon_0}\sum_{m\neq n}\left[\left(1-\frac{i\omega|n-m|d}{c}\right)\frac{-e^{ik(m-n)d}}{|n-m|^3}\right. \\
&\left.+\frac{\omega^2d^2}{c^2}\frac{e^{ik(m-n)d}}{|n-m|}\right]e^{i\omega|n-m|d/c}
\end{aligned} \tag{A.13}$$

Dividing the equation for preceding and succeeding coupled dipoles, we can write:

$$\begin{aligned}1 =& -\frac{\alpha(\omega)}{d^3}\frac{1}{4\pi\varepsilon_0}\sum_{m=-\infty}^{n-1}\left[\left(1-\frac{i\omega|n-m|d}{c}\right)\frac{e^{-ik(n-m)d}}{|n-m|^3}\right.\\ &\left.-\frac{\omega^2d^2}{c^2}\frac{e^{-ik(n-m)d}}{|n-m|}\right]e^{i\omega|n-m|d/c}+\\ &-\frac{\alpha(\omega)}{d^3}\frac{1}{4\pi\varepsilon_0}\sum_{m=n+1}^{\infty}\left[\left(1-\frac{i\omega|n-m|d}{c}\right)\frac{-e^{ik(m-n)d}}{|n-m|^3}\right.\\ &\left.-\frac{\omega^2d^2}{c^2}\frac{e^{ik(m-n)d}}{|n-m|}\right]e^{i\omega|n-m|d/c}\end{aligned} \tag{A.14}$$

Rearranging the complex exponentials and substituting them with their order difference $j=(n-m)$, we can obtain:

$$\begin{aligned}1 =& -\frac{\alpha(\omega)}{d^3}\frac{1}{4\pi\varepsilon_0}\sum_{j=1}^{\infty}\left[\left(1-\frac{i\omega|n-m|d}{c}\right)\frac{1}{|n-m|^3}\right.\\ &\left.-\frac{\omega^2d^2}{c^2}\frac{1}{|n-m|}\right]e^{i\omega|n-m|d/c}\left(e^{-ikdj}+e^{ikdj}\right)\end{aligned} \tag{A.15}$$

Per Euler's identity, the last complex exponential sum can be written as $e^{-ikdj}+e^{ikdj}=2cos(jkd)$. The final dispersion relation formula then translates to:

$$0 =1+\frac{2\alpha(\omega)}{d^3}\frac{1}{4\pi\varepsilon_0}\sum_{j=1}^{\infty}\left[\left(1-\frac{i\omega jd}{c}\right)\frac{1}{j^3}-\frac{\omega^2d^2}{c^2}\frac{1}{j}\right]e^{i\omega jd/c}cos(jkd) \tag{A.16}$$

### *A.2.2 Longitudinal excitation*

For longitudinal excitation, the same transformations as the transverse excitation can be applied. Substitution with $e^{iknd}$ yields:

$$\begin{aligned}e^{iknd} =&\alpha(\omega)\sum_{m\neq n}\frac{1}{4\pi\varepsilon_0}\left[\left(1-\frac{i\omega|n-m|d}{c}\right)\frac{2e^{ikmd}}{|n-m|^3d^3}\right]\\ &\times e^{i\omega|n-m|d/c}\end{aligned} \tag{A.17}$$

Applying the same expansion as (A.13), we can write:

$$\begin{aligned}1 =& \frac{2\alpha(\omega)}{d^3}\frac{1}{4\pi\varepsilon_0}\sum_{m=-\infty}^{n-1}\left[\left(1-\frac{i\omega|n-m|d}{c}\right)\frac{e^{i(m-n)kd}}{|n-m|^3}\right]\\ &\times e^{i\omega|n-m|d/c}\\ &+\frac{2\alpha(\omega)}{d^3}\frac{1}{4\pi\varepsilon_0}\sum_{m=n+1}^{\infty}\left[\left(1-\frac{i\omega|n-m|d}{c}\right)\frac{e^{i(m-n)kd}}{|n-m|^3}\right]\\ &\times e^{i\omega|n-m|d/c}\end{aligned} \tag{A.18}$$

Redefining $m - n$ as $j$:

$$1 = \frac{2\alpha(\omega)}{d^3}\frac{1}{4\pi\varepsilon_0}\sum_{j=1}^{\infty}\left[\left(1 - \frac{i\omega d}{c}j\right)\frac{e^{ijkd} + e^{-ijkd}}{j^3}\right]e^{i\omega jd/c} \tag{A.19}$$

Exploiting the Euler's identity, we can obtain the longitudinal analogue for Eq. (A.16):

$$0 = 1 - \frac{4\alpha(\omega)}{d^3}\frac{1}{4\pi\varepsilon_0}\sum_{j=1}^{\infty}\left(1 - \frac{i\omega d}{c}j\right)\frac{cos(jkd)}{j^3}e^{i\omega jd/c} \tag{A.20}$$

### *A.2.3 Dispersion characterization*

It should be noted that for $e^{-i\omega t}$ time dependence, $Im[\omega]$ takes on negative sign to account for loss. The infinite sums in (A.16) and (A.20) converge only for $Im[\omega] > 0$; this complicates their analytical evaluation [56]. In order to obtain the correct dispersion relation for such infinite structures, the following approaches could be employed:

- Quasistatic approximation can be applied to simplify the polarization expressions. In this approach, the light speed $c$ and electron scattering loss $\nu$ are assumed to tend to $\infty$ and zero, respectively. Being valid for the systems much smaller than the wavelength of the incident electromagnetic wave [53], this technique may fail to accurately represent the full dispersive behavior of the infinite chain [56].

- Polylogarithm functions can be used to evaluate the real wavevector solutions in the complex domain [63].

- The continuous dispersive behavior can be approximated with the discrete dispersion relation of a sufficiently-long finite nanochain, which admits the expression [56],

  $$k = \left[\frac{(N-2)l + 1}{N(N-1)}\right]\frac{\pi}{d}$$

  where $k$ is the real wavevector, $N$ is the number of nanoparticles and $l$ is the mode number.

# Appendix B

# APPLICABILITY OF MODE ORTHOGONALITY

In the analysis of different types of guided wave structures, mode orthogonality is a strong and versatile tool, particularly for the characterization of field and power coupling. In this appendix, limits and applicability of generalized and special cases of mode orthogonality will be briefed from a theoretical and numerical standpoint.

An arbitrary field distribution along a waveguide cross section can be decomposed into the characteristic solutions to Maxwell's equations for given boundary conditions. Known also as characteristic modes, these can be categorized into guided modes, which are often discrete, and radiation modes, which present themselves as a continuum. For layered waveguides, the incident fields on the waveguide can be written as [85]:

$$\begin{aligned} \mathbf{E}_{inc} &= \sum_{j=1}^{N} (a_j \mathbf{E}_j + b_j \mathbf{E}_{-j}) + \mathbf{E}_{rad} \\ \mathbf{H}_{inc} &= \sum_{j=1}^{N} (a_j \mathbf{H}_j + b_j \mathbf{H}_{-j}) + \mathbf{H}_{rad} \end{aligned} \tag{B.1}$$

where the coefficients $a_j$ and $b_j$ denote the complex amplitude coefficients for the forward and backward propagating guided modes. Mode orthogonality relations exploit the fact that each of these mode solutions are *linearly independent* from each other. A simple derivation of the mode orthogonality relation is possible with the manipulation of Lorentz reciprocity theorem, which can be expressed as [37]:

$$\oint_S \left[\mathbf{E}_1 \times \mathbf{H}_2 - \mathbf{E}_2 \times \mathbf{H}_1\right] \cdot dS = \int_V \left[\mathbf{J}_1 \cdot \mathbf{E}_2 - \mathbf{J}_2 \cdot \mathbf{E}_1\right] dV \tag{B.2}$$

where $\mathbf{J}_n$ represents the current density $n$, while $\mathbf{E}_n$ and $\mathbf{J}_n$ are the associated field distributions. Since the characteristic modes of a guided wave system are sought, the current densities can be discarded; the guided and radiation modes of this system

should be able to sustain themselves without a forced response. Thus, the $m$th and $n$th mode of a waveguide can be related as:

$$\int_S \mathbf{E}_m \times \mathbf{H}_n \cdot dS = \int_S \mathbf{E}_n \times \mathbf{H}_m \cdot dS = 0 \tag{B.3}$$

which is also referred as the unconjugate mode orthogonality [85]. It should be noted due to absence of the volume integral, the integration on the left-handside is performed at the transverse plane instead on a closed surface.

A more specific form of this relation with conjugation is known as power orthogonality or orthonormality, which indicates that the cumulative power flow through the cross section is the algebraic sum of individual mode powers [37]:

$$\int_S \mathbf{E}_m \times \mathbf{H}_n^* \cdot dS = \int_S \mathbf{E}_n \times \mathbf{H}_m^* \cdot dS = 0 \tag{B.4}$$

While the power orthogonality condition strictly holds for lossless waveguides, it is not necessarily valid for lossy structures, such as those studied throughout this thesis.

Backward-propagating modes at Eq. (B.1) can be represented with transverse and normal vectorial components of the forward-propagating modes [37]:

$$\begin{aligned} \mathbf{E}_j &= \mathbf{E}_j^t + \mathbf{E}_j^n \\ \mathbf{E}_{-j} &= \mathbf{E}_j^t - \mathbf{E}_j^n \\ \mathbf{H}_j &= \mathbf{H}_j^t + \mathbf{H}_j^n \\ \mathbf{H}_{-j} &= -\mathbf{H}_j^t + \mathbf{H}_j^n \end{aligned} \tag{B.5}$$

with superscripts $t$ and $n$ representing the transverse and normal components of the mode fields, respectively. For a one-layered plasmonic waveguide, only a single guided mode exists: the SPP mode. Applying Eqs. (B.3) and (B.5) on the modal expansions on (B.1), radiation modes can be eluded and following identities can be extracted:

$$\begin{aligned} \int_S \mathbf{E}_{inc} \times \mathbf{H}_{\mathrm{SPP}} \cdot dS &= (a_{\mathrm{SPP}} + b_{\mathrm{SPP}}) \int_S \mathbf{E}_{\mathrm{SPP}} \times \mathbf{H}_{\mathrm{SPP}} \cdot dS \\ \int_S \mathbf{E}_{\mathrm{SPP}} \times \mathbf{H}_{inc} \cdot dS &= (a_{\mathrm{SPP}} - b_{\mathrm{SPP}}) \int_S \mathbf{E}_{\mathrm{SPP}} \times \mathbf{H}_{\mathrm{SPP}} \cdot dS \end{aligned} \tag{B.6}$$

The algebraic manipulation of the identities above yields the explicit expansion coefficients for the SPP mode:

$$\begin{aligned} a_{\mathrm{SPP}} &= \frac{\int_S \mathbf{E}_{inc} \times \mathbf{H}_{\mathrm{SPP}} \cdot dS + \int_S \mathbf{E}_{\mathrm{SPP}} \times \mathbf{H}_{inc} \cdot dS}{2 \int_S \mathbf{E}_{\mathrm{SPP}} \times \mathbf{H}_{\mathrm{SPP}} \cdot dS} \\ b_{\mathrm{SPP}} &= \frac{\int_S \mathbf{E}_{inc} \times \mathbf{H}_{\mathrm{SPP}} \cdot dS - \int_S \mathbf{E}_{\mathrm{SPP}} \times \mathbf{H}_{inc} \cdot dS}{2 \int_S \mathbf{E}_{\mathrm{SPP}} \times \mathbf{H}_{\mathrm{SPP}} \cdot dS} \end{aligned} \tag{B.7}$$

Since power orthogonality does not necessarily hold for lossy waveguides, the expansion coefficients above *may not* represent the actual complex mode amplitudes besides a reasonable proportionality: integral at the denominator no longer corresponds to the guided mode power due to unconjugation [73]. This does not affect the reflection and transmission coefficients that are provided on Eqs. (3.4) and (3.5), as both expansion coefficients are normalized with respect to each other rather than with the mode power. Additionally considering that the surface modes in question decay considerably before the spatial truncation, the expansion coefficients can be calculated with a sufficiently high accuracy [74]. In the case of intermodal coupling, such as the excitation of a gap mode with an incoming SPP wave, this approach is not valid and other alternatives, such as GPOF method, should be sought.

A recent work by Sharifi and Gordon [100] considers the application of aforementioned orthogonality relations to the mode-matching approach in Section 3.2.2. Mainly suggested by the losses in the metal, the approach yields the unconjugated form of Eq. (3.29):

$$\frac{(1-\Gamma)}{(1+\Gamma)} = \frac{-1}{\lambda_0 \eta_0 \int_{-\infty}^{\infty} E_z^{SP} H_y^{SP} dz} \int_{-\infty}^{\infty} \frac{(I_1(u))^2}{\sqrt{1-u^2}} du \tag{B.8}$$

Even though the application of a more general orthogonality relation may be more appropriate for this case, since the power orthogonality is not strictly valid for lossy waveguides and only approximately valid for weakly-absorbing ones [85], this approach brings out certain problems. Parseval's theorem, which is used to represent the Poynting flux with the angular spectra of the free-space scattered fields at Eq. (3.26), no longer holds for unconjugated inner-product. While the evaluation of the newly-introduced formula produces results nearly identical with the conjugated form for MIM discontinuities, it fails to represent the behaviour of MI terminations altogether.

# Appendix C

# SURFACE PLASMON POLARITON EXCITATION WITH A MAGNETIC LINE SOURCE

One of the key methods to analyze the validity of any numerical approach is comparison with an analytically-proven test case. To assess the performance of GPOF method for surface waves, a test case can be constructed through the use of a *magnetic line source* that is impressed at the interface between vacuum ($\varepsilon_d = 1$) and metallic half-space ($\varepsilon_m$). While these sources are not found in nature in their purest forms, they are often used by engineers as virtual sources to simplify complex radiation and diffraction problems [131], including those related to the excitation of surface waves [89, 132].

A magnetic line source in a 2D medium can be regarded either as an infinitesimally-small electric current loop, or a current of fictitious magnetic charges. By the duality principle in electromagnetics, Maxwell equations on Eqs. (2.1) can be adapted for the latter case as follows [24, 131]:

$$\nabla \cdot \mathbf{B} = \rho_m \tag{C.1a}$$

$$\nabla \times \mathbf{E} - i\omega\mathbf{B} = -\mathbf{J}_m \tag{C.1b}$$

$$\nabla \cdot \mathbf{D} = 0 \tag{C.1c}$$

$$\nabla \times \mathbf{H} + i\omega\mathbf{D} = 0 \tag{C.1d}$$

where $\rho_m$ and $\mathbf{J}_m$ are the magnetic charge and current densities, respectively. In this formulation, the electric charges and current densities are assumed to be non-existent. Fields from a single line source can be obtained through vectorial wave equation for magnetic field, which can be derived from the modified Maxwell's equa-

tions in a similar manner to its electric analogue:

$$\begin{aligned} \nabla \times (\nabla \times \mathbf{H}) &= \nabla \times (-i\omega \mathbf{D}) \\ \nabla(\nabla \cdot \mathbf{H}) - \nabla^2 \mathbf{H} &= -i\omega\varepsilon_0(i\omega\mathbf{B} - \mathbf{J}_m) \\ \nabla(\nabla \cdot \mathbf{H}) - \nabla^2 \mathbf{H} &= \omega^2 \varepsilon_0 \mu_0 \mathbf{H} + i\omega\varepsilon_0 \mathbf{J}_m \end{aligned} \tag{C.2}$$

Invoking the continuity equation, which is also valid for magnetic charges and currents, Eq. (C.2) can be further simplified as:

$$\begin{aligned} \nabla \underbrace{(\nabla \cdot \mathbf{H})}_{\frac{\nabla \cdot \mathbf{J}_m}{i\omega\mu_0}} - \nabla^2 \mathbf{H} &= \omega^2 \mu_0 \varepsilon_0 \mathbf{H} + i\omega\varepsilon_0 \mathbf{J}_m \\ \nabla^2 \mathbf{H} + \omega^2 \mu_0 \varepsilon_0 \mathbf{H} &= \frac{\nabla\nabla \cdot \mathbf{J}_m}{i\omega\mu_0} - i\omega\varepsilon_0 \mathbf{J}_m \\ \nabla^2 \mathbf{H} + \omega^2 \mu_0 \varepsilon_0 \mathbf{H} &= -i\omega\varepsilon_0 \left[\bar{\mathbb{I}} + \frac{\nabla\nabla}{\omega^2 \mu_0 \varepsilon_0}\right] \mathbf{J}_m \\ \nabla^2 \mathbf{H} + k^2 \mathbf{H} &= -i\omega\varepsilon_0 \left[\bar{\mathbb{I}} + \frac{\nabla\nabla}{k^2}\right] \mathbf{J}_m \end{aligned} \tag{C.3}$$

where $\bar{\mathbb{I}}$ is the unit dyad and $k$ is the wavevector. Substituting the source term with an impulse yields the dyadic Green's function for magnetic field, which can be written as:

$$\mathbf{G}^H(\mathbf{r}, \mathbf{r'}) = \left[\bar{\mathbb{I}} + \frac{\nabla\nabla}{k^2}\right] g(\mathbf{r} - \mathbf{r'}) \tag{C.4}$$

with $g(\mathbf{r} - \mathbf{r'})$ being the Green's function for scalar wave equation. The final expression essentially parallels with the dyadic Green function for electric field, with the fields and sources being interchaged with their analogues, and vice versa [24]. For an arbitrary magnetic current density distribution in a homogenous space ($\mathbf{J}_m$), the corresponding magnetic field can thus be written as:

$$\mathbf{H}(\mathbf{r}) = i\omega\varepsilon_0 \int dV \mathbf{G}^H(\mathbf{r}, \mathbf{r'}) \mathbf{J}_m(\mathbf{r'}) \tag{C.5}$$

It should be noted that for our test case, the line current is situated along the axis of translational invariance ($y$-axis); thus, the Green's function for scalar wave equation takes on its 2D form. The resulting TM-polarized magnetic field

distribution ($H_y$) due to a $y$-oriented source can be written as:

$$\begin{aligned} H_y(x,z) &= i\omega\varepsilon_0 \left(1 + \frac{1}{k^2}\underbrace{\frac{d^2}{dy^2}}_{=0}\right) g(x,y) \\ &= i\omega\varepsilon_0 g(x,y) \end{aligned} \tag{C.6}$$

Since the fields are assumed to be the same throughout $y$-axis, the associated double derivative in the dyad vanishes. In order to obtain the excited SPP distribution along the interface ($z = 0$), we need the spatial-domain Green's function for scalar wave equation, which can be extracted through the Fourier inversion of its angular spectrum. Since this plane wave spectrum emanating from the source is also reflected from the lower metallic half-space, the integrand should be modified accordingly. For this particular problem, this modification can be performed in conjunction with the TM-polarization Fresnel equation $R^{TM}$ (Eq. (2.14)) for the metallo-dielectric boundary [24],

$$\begin{aligned} H_y(x,z) &= i\omega\varepsilon_0 \frac{i}{2\pi}\int_{-\infty}^{\infty} dk_x \frac{e^{ik_z|z|+ik_x x}}{2k_z}\left[1 + R^{TM}(k_z)\right] \\ &= i\omega\varepsilon_0 \frac{i}{2\pi}\int_{-\infty}^{\infty} dk_x \frac{e^{ik_z|z|+ik_x x}}{2k_z}\left[1 + \frac{\varepsilon_m k_{zd} - k_{zm}}{\varepsilon_m k_{zd} + k_{zm}}\right] \\ &= i\omega\varepsilon_0 \frac{i}{2\pi}\int_{-\infty}^{\infty} dk_x e^{ik_z|z|+ik_x x}\left[\frac{\varepsilon_m}{\varepsilon_m k_z + k_{zm}}\right] \\ H_y(x, z=0) &= \frac{-\omega\varepsilon_0}{2\pi}\int_{-\infty}^{\infty} dk_x e^{ik_x x}\left[\frac{\varepsilon_m}{\varepsilon_m k_z + k_{zm}}\right] \end{aligned} \tag{C.7}$$

with $k_z = \sqrt{k_0^2 - k_x^2}$ and $k_{zm} = \sqrt{\varepsilon_m k_0^2 - k_x^2}$. This inversion integral, named as the Sommerfeld integral, has no analytical solution in most cases. Therefore, spatial-domain Green's functions are mostly obtained through different approaches such as numerical quadrature [24] or closed-form Green's functions [134]. Since we are only seeking the complex amplitude of the SPP wave at the metallo-dielectric boundary, a full-scale evaluation of this integral is not necessary and our calculations simplify considerably. This surface wave contribution from the line source is extracted from the residue of the inversion integral in Eq. (C.7) [89]. Observing that the pole of the integrand (surface wave pole) corresponds to the SPP propagation constant $\beta_{\mathrm{SPP}}$

(Eq. (2.31)), the residue can be evaluated as:

$$\begin{aligned}\mathrm{Res}_{\beta_{\mathrm{SPP}}} &= \lim_{k_x \to \beta_{\mathrm{SPP}}} (k_x - \beta_{\mathrm{SPP}}) e^{ik_x x} \left[ \frac{\varepsilon_m}{\varepsilon_m k_z + k_{zm}} \right] \\ &= \frac{e^{i\beta_{\mathrm{SPP}}|x|}}{-\beta_{\mathrm{SPP}} \left[ (k_0^2 - \beta_{\mathrm{SPP}}^2)^{-\frac{1}{2}} + \varepsilon_m (\varepsilon_m k_0^2 - \beta_{\mathrm{SPP}}^2)^{-\frac{1}{2}} \right]}\end{aligned} \tag{C.8}$$

Per residue theorem, the generated SPP field is:

$$\begin{aligned}H_y^{\mathrm{SPP}}(x, z=0) &= \frac{-\omega\varepsilon_0}{2\pi} (2\pi i \, \mathrm{Res}_{\beta_{\mathrm{SPP}}}) \\ &= \frac{i\omega\varepsilon_0 e^{i\beta_{\mathrm{SPP}} x}}{\beta_{\mathrm{SPP}} \left[ (k_0^2 - \beta_{\mathrm{SPP}}^2)^{-\frac{1}{2}} + \varepsilon_m (\varepsilon_m k_0^2 - \beta_{\mathrm{SPP}}^2)^{-\frac{1}{2}} \right]}\end{aligned} \tag{C.9}$$

## *C.1 FDTD simulations*

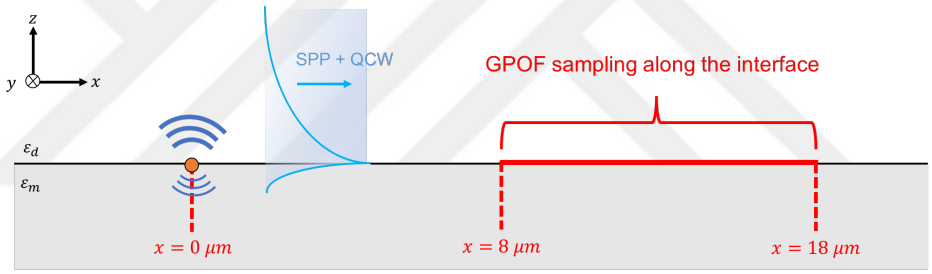


Figure C.1: SPP and quasi-cylindrical wave (QCW) excitation via a magnetic line source at the origin on a metallic surface. The layers are translationally-invariant along the $y$-axis.

The FDTD simulation scheme is provided on Fig. C.1: the 2D line source is impressed at the origin, which is located on the interface between dielectric and vacuum. In order to weed out the radiation modes from the source, magnetic field distribution on the interface is sampled at a distance of 8 $\mu m$ from the origin for 10 $\mu ms$. To perform GPOF analysis, a uniform mesh size of 10 nms in applied on the frequency-domain sampling monitor to induce equal intervals between adjacent points. As field monitoring was performed over a large spatial domain, only the data for 6 equally-spaced free-space wavelengths between 500 and 1000 nms were stored. The number of exponentials for approximation was determined by the mag-

nitude of normalized singular, with 1$e$-4 being chosen as the tolerance; the dominant exponential was assumed to pertain to the SPP wave.

Since Lumerical's current sources use dipole moments as unit amplitudes, normalization is necessary to make an accurate comparison in terms of wave amplitude. Akin to a simple test procedure provided by Waldschmidt and Taflove for point sources on a FDTD grid [135], the effective current dipole moment for the line source can be obtained through scaling the numerical and analytical results for magnetic field distributions from the exact same source in free-space: the latter is known analytically [24, 131]:

$$H_y^{\mathrm{FS}} = -I_l \frac{\omega \varepsilon_0}{4} H_0^{(1)}(k_o \rho) \tag{C.10}$$

with $H_0^{(1)}$ being the Hankel function of the first kind and $I_l$ being the sought complex amplitude of the source due to an unit current dipole moment. The FDTD simulation for the source in free-space was performed for a fine mesh ($\sim \lambda_0^{min}/100$) to ensure convergence [135]; the simulation results for the layered media were normalized with the obtained dipole coefficients for accurate comparison.

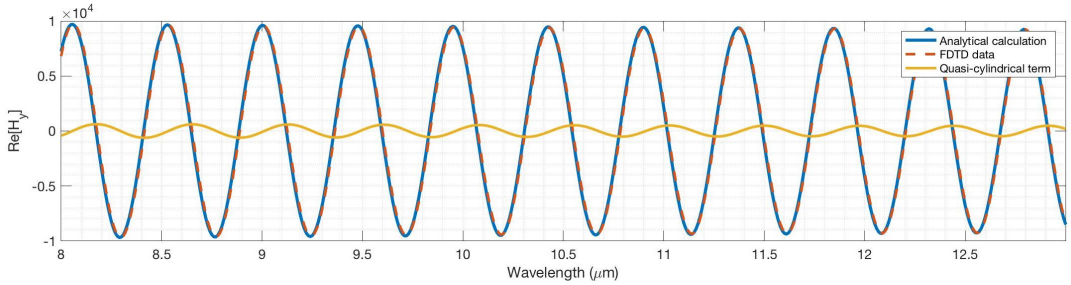


(a) $\lambda_0 = 500\ nm$

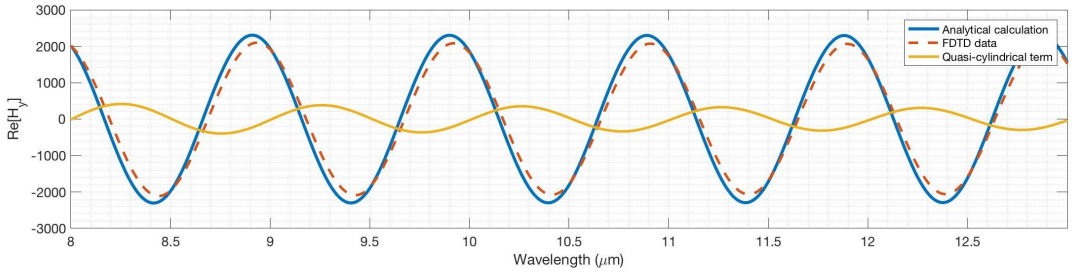


(b) $\lambda_0 = 1000\ nm$

Figure C.2: Real parts of the magnetic field distribution ($H_y$) induced by a magnetic line source on a metallo-dielectric interface

The real part of the computed and simulated magnetic field distributions are provided on Figs. C.2a and C.2b for two reference wavelengths of 500 and 1000 nms. The difference between analytical and FDTD results is interpreted as the QCW [86]. It should be noted that this component constitutes a larger portion of the surface field for increasing wavelengths [88] and thus may act as a source of estimation error at GPOF analysis.

Since SPP complex amplitudes and wavevectors are now analytically known, the GPOF results from the FDTD data can be accurately assessed. The magnitude of the SPP field at the sampling point ($x = 8\ \mu m$) is plotted on Fig. C.3, where the subfigures ($a$) and ($b$) describe the actual results and the absolute error, respectively. It can be seen that deviations from the analytical results are much more apparent for larger wavelengths, exceeding approximately 10% of the analytical result after 900 nm.

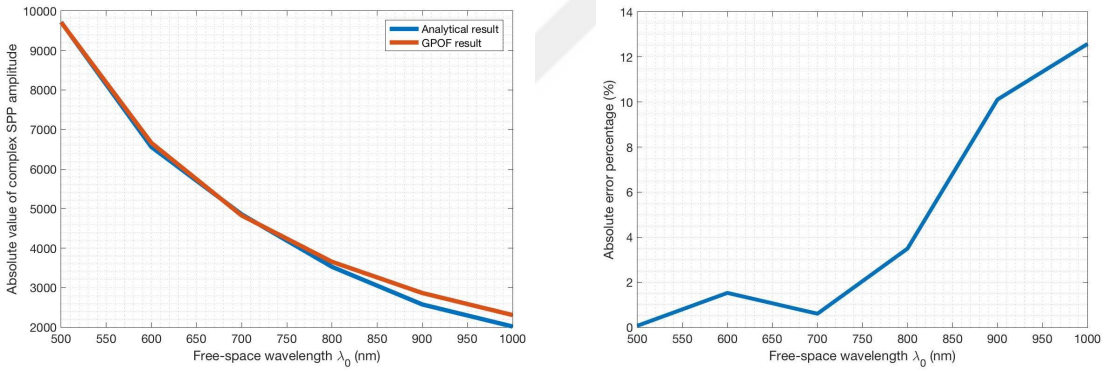


(a) Comparison of wave magnitudes

(b) Absolute magnitude error percentage

Figure C.3: Complex SPP magnitudes, as predicted by analytical method and GPOF analysis of FDTD data

Another figure of merit for GPOF analysis is the accurate estimation of the SPP wavevector or propagation constant. While the approximation of this constant is not necessary for our case, it is essential for cases in which the dispersion relation is not analytically known, i.e. three-dimensional dielectric or plasmonic waveguides. The comparison of results from the analytical formula and GPOF analysis is given on Fig. C.4 for real ($a$) and imaginary ($b$) parts of the wavevectors. As seen on these

subfigures, the dominant real part of the wavevector, which pertains to oscillation, is almost flawlessly approximated for all frequencies. In contrast, the approximate results deviate significantly from the analytical ones for the imaginary part, which is related with the damping. For free-space wavelengths from 800 to 1000 nms, the sign of negative imaginary parts represent gain, which is unphysical and invalid for our case. The erroneous GPOF results for complex SPPs can be attributed to the order of magnitude differences between the real and imaginary parts of the propagation constant: accordingly, the weight of the imaginary part is lost during the GPOF subroutine.

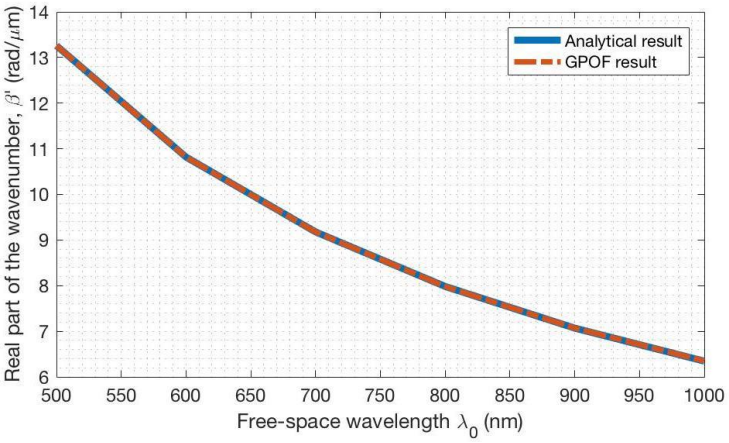


(a) Real part of the SPP wavevector, $\beta'_{\mathrm{SPP}}$

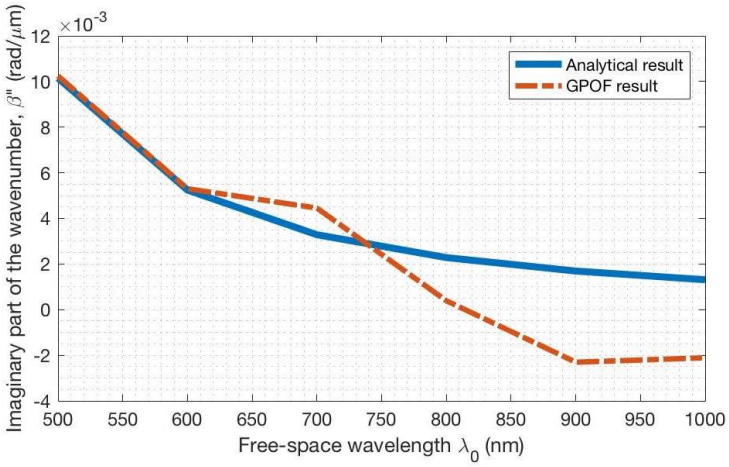


(b) Imaginary part of the SPP wavevector, $\beta''_{\mathrm{SPP}}$

Figure C.4: Real and imaginary parts of the SPP wavevector, as obtained by analytical calculations and GPOF analysis of the FDTD data

# Appendix D

# VECTORIAL MODE-MATCHING APPROACH FOR FIELD TRANSMISSION INTO A PLASMONIC CAVITY

Mode-matching approach for the reflection from a MIM plasmonic cavity can be applied for the reversed problem: excitation of the cavity by an inbound plane wave. The explicit expression for a normally-incident plane wave was derived by Chandran et al. [45] In this subsection, this method is briefly reviewed and extended to include incident plane waves with arbitrary angle of incidence. The schemes for SPP excitation via normally- and obliquely- incident plane waves are provided on Figs. D.1.a and D.1.b, respectively.

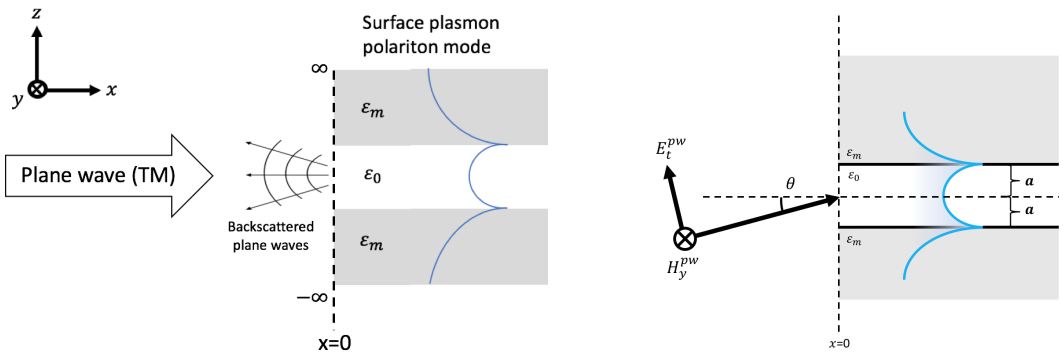


(a) Normal incidence

(b) Oblique incidence with an impacting angle of $\theta$

Figure D.1: Scheme of plane wave backscattering from and SPP transmission into a MIM cavity

As in the case of the derivation of reflection coefficient, the boundary conditions will be enforced at the interface between the free-space and MIM waveguide, where the incident field is assumed to only excite the dominant symmetric mode in the waveguide. At this interface, located at $x = 0$ on Fig. D.1.b, the transverse electric

fields can be decomposed into the incident ($E_z^{\text{pw}}$), backscattered ($E_z^{\text{sca}}$) and excited fields ($E_z^{\text{SPP}}$) as

$$\underbrace{E_z^{\text{pw}}}_{e^{ik_\theta z}} + E_z^{\text{sca}} = tE_z^{\text{SPP}} \tag{D.1}$$

where $k_\theta = k_0 cos(\theta)$ is the transverse wavevector of the incident plane wave in $z$-axis. Through the Fourier transform of the identity above, the angular spectra of the backscattered fields at Fig. D.1a, $g(k_z)$, can be written as

$$\begin{aligned} g(k_z) &= FT\{E_z^{\text{sca}}\} \\ &= FT\{tE_z^{\text{SPP}} - e^{ik_\theta z}\} \\ &= \frac{t}{2\pi} I(k_z) - \delta(k_z - k_\theta) \end{aligned} \tag{D.2}$$

where $I(k_z)/(2\pi)$ represents the Fourier transform of $E_z^{\text{SPP}}$, as in Eq. (3.20). Applying the Poynting flux conservation as in the reflection case to the discontinuity, we obtain:

$$\begin{gathered} \int_{-\infty}^{\infty} \left(E_z^{\text{pw}} + E_z^{\text{sca}}\right)\left(H_y^{\text{pw}} + H_y^{\text{sca}}\right)^* dz = tt^* \int_{-\infty}^{\infty} E_z^{\text{SPP}} H_y^{\text{SPP}^*} dz \\ \int_{-\infty}^{\infty} \underbrace{\left(e^{ik_i z} + E_z^{\text{sca}}\right)}_{tE_z^{\text{SPP}}} \left(\frac{-k_0^2 e^{ik_i z}}{\omega\mu_0\sqrt{k_0^2 - k_\theta^2}} + H_y^{\text{sca}}\right)^* dz = tt^* \int_{-\infty}^{\infty} E_z^{\text{SPP}} H_y^{\text{SPP}^*} dz \\ \int_{-\infty}^{\infty} E_z^{\text{SPP}} \left(\frac{-k_0^2 e^{ik_i z}}{\omega\mu_0\sqrt{k_0^2 - k_\theta^2}} + H_y^{\text{sca}}\right)^* dz = t^* \int_{-\infty}^{\infty} E_z^{\text{SPP}} H_y^{\text{SPP}^*} dz \end{gathered} \tag{D.3}$$

The integration of the SPP field and the magnetic field on the left-handside can be handled analytically through representing the expression in terms of $I(k_z)$:

$$\begin{aligned} \int_{-\infty}^{\infty} E_z^{\text{SPP}} \left(\frac{-k_0^2 e^{ik_\theta z}}{\omega\mu_0\sqrt{k_0^2 - k_\theta^2}}\right)^* dz &= \frac{-k_0^2}{\omega\mu_0(\sqrt{k_0^2 - k_\theta^2})^*} \int_{-\infty}^{\infty} E_z^{\text{SPP}} e^{-ik_\theta^* z} dz \\ &= \frac{-k_0^2}{\omega\mu_0(\sqrt{k_0^2 - k_\theta^2})^*} I(k_i^*) \end{aligned} \tag{D.4}$$

For the remainder of the left-handside, Parseval's theorem can be exploited as in the case for reflection coefficient. Algebraic manipulation of the resulting terms would yield the explicit expression for transmission:

$$t(k_\theta) = \left[ \frac{\frac{-2k_0^2}{\omega\mu_0(\sqrt{k_0^2 - k_\theta^2})^*} I(k_\theta^*)}{\int_{-\infty}^{\infty} E_z^{\text{SPP}} H_y^{\text{SPP}^*} dz - \frac{k_0^2}{2\pi\omega\mu_0} \int_{-\infty}^{\infty} \frac{|I_1(k_z)|^2 k_0^2}{(\sqrt{k_0^2 - k_z^2})^*} dk_z} \right]^* \tag{D.5}$$

# BIBLIOGRAPHY

[1] K. Michalski and J. Mosig, "The Sommerfeld half-space problem revisited: from radio frequencies and Zenneck waves to visible light and Fano modes," *Journal of Electromagnetic Waves and Applications*, vol. 30, no. 1, pp. 1–42, 2016.

[2] R. Wood, "XLII. On a remarkable case of uneven distribution of light in a diffraction grating spectrum," *The London, Edinburgh, and Dublin Philosophical Magazine and Journal of Science*, vol. 4, no. 21, pp. 396–402, 1902.

[3] U. Fano, "The theory of anomalous diffraction gratings and of quasi-stationary waves on metallic surfaces (Sommerfeld's waves)," *J. Opt. Soc. Am.*, vol. 31, no. 3, pp. 213–222, Mar 1941.

[4] R. H. Ritchie, "Plasma losses by fast electrons in thin films," *Phys. Rev.*, vol. 106, pp. 874–881, Jun 1957.

[5] R. H. Ritchie, E. T. Arakawa, J. J. Cowan, and R. N. Hamm, "Surface-plasmon resonance effect in grating diffraction," *Phys. Rev. Lett.*, vol. 21, pp. 1530–1533, Nov 1968.

[6] E. N. Economou, "Surface plasmons in thin films," *Phys. Rev.*, vol. 182, pp. 539–554, Jun 1969.

[7] E. Kretschmann and H. Raether, "Notizen: Radiative decay of non radiative surface plasmons excited by light:," *Zeitschrift für Naturforschung A*, vol. 23, no. 12, pp. 2135–2136, 1968.

[8] A. Otto, "Excitation of nonradiative surface plasma waves in silver by the

method of frustrated total reflection," *Appl. Opt.*, vol. 216, pp. 398–410, Aug 1968.

[9] S. A. Maier, M. L. Brongersma, P. G. Kik, S. Meltzer, A. A. G. Requicha, and H. A. Atwater, "Plasmonics—a route to nanoscale optical devices," *Advanced Materials*, vol. 13, no. 19, pp. 1501–1505, 2001.

[10] J. Homola, S. S. Yee, and G. Gauglitz, "Surface plasmon resonance sensors: review," *Sensors and Actuators B: Chemical*, vol. 54, no. 1, pp. 3–15, 1999.

[11] E. Özbay, "Plasmonics: Merging photonics and electronics at nanoscale dimensions," *Science*, vol. 311, no. 5758, pp. 189–193, 2006.

[12] H. A. Atwater and A. Polman, "Plasmonics for improved photovoltaic devices," *Nature Materials*, vol. 9, no. 3, pp. 205–213, Mar 2010.

[13] N. Fang, H. Lee, C. Sun, and X. Zhang, "Sub-diffraction-limited optical imaging with a silver superlens," *Science*, vol. 308, no. 5721, pp. 534–537, 2005.

[14] D. J. Bergman and M. I. Stockman, "Surface plasmon amplification by stimulated emission of radiation: Quantum generation of coherent surface plasmons in nanosystems," *Phys. Rev. Lett.*, vol. 90, p. 027402, Jan 2003.

[15] B. Gallinet, J. Butet, and O. J. F. Martin, "Numerical methods for nanophotonics: standard problems and future challenges," *Laser & Photonics Reviews*, vol. 9, no. 6, pp. 577–603, 2015.

[16] A. Oliner, "Historical perspectives on microwave field theory," *IEEE Transactions on Microwave Theory and Techniques*, vol. 32, no. 9, pp. 1022–1045, 1984.

[17] N. Kinayman and M. I. Aksun, *Modern Microwave Circuits*. Artech House, 2005.

[18] G. Veronis and S. Fan, "Bends and splitters in metal-dielectric-metal subwavelength plasmonic waveguides," *Applied Physics Letters*, vol. 87, no. 13, p. 131102, 2005.

[19] S. Kocabaş, G. Veronis, D. A. B. Miller, and S. Fan, "Transmission line and equivalent circuit models for plasmonic waveguide components," *IEEE Journal of Selected Topics in Quantum Electronics*, vol. 14, no. 6, pp. 1462–1472, 2008.

[20] D.-S. Ly-Gagnon, S. E. Kocabas, and D. A. B. Miller, "Characteristic impedance model for plasmonic metal slot waveguides," *IEEE Journal of Selected Topics in Quantum Electronics*, vol. 14, no. 6, pp. 1473–1478, 2008.

[21] M. Staffaroni, J. Conway, S. Vedantam, J. Tang, and E. Yablonovitch, "Circuit analysis in metal-optics," *Photonics and Nanostructures - Fundamentals and Applications*, vol. 10, no. 1, pp. 166–176, 2012.

[22] S. Maier, *Plasmonics: Fundamentals and Applications*. Springer, 2007.

[23] H. Fearn, D. F. V. James, and P. W. Milonni, "Microscopic approach to reflection, transmission, and the Ewald–Oseen extinction theorem," *American Journal of Physics*, vol. 64, no. 8, pp. 986–995, 1996.

[24] W. C. Chew, *Waves and Fields in Inhomogenous Media*. Wiley-IEEE Press, 1999.

[25] L. A. Weller-Brophy and D. G. Hall, "Analysis of waveguide gratings: application of Rouard's method," *J. Opt. Soc. Am. A*, vol. 2, no. 6, pp. 863–871, Jun 1985.

[26] P. Lecaruyer, E. Maillart, M. Canva, and J. Rolland, "Generalization of the Rouard method to an absorbing thin-film stack and application to surface plasmon resonance," *Appl. Opt.*, vol. 45, no. 33, pp. 8419–8423, Nov 2006.

[27] P. B. Johnson and R. W. Christy, "Optical constants of the noble metals," *Phys. Rev. B*, vol. 6, pp. 4370–4379, Dec 1972.

[28] T. P. M. L. Genzel and U. Kreibig, "Dielectric function and plasma resonances of small metal particles," *Zeitschrift für Physik B Condensed Matter*, vol. 21, p. 339–346, 1975.

[29] P. Drude, "Zur Elektronentheorie der Metalle," *Annalen der Physik*, vol. 306, no. 3, pp. 566–613, 1900.

[30] R. E. Hummel, *Electronic Properties of Materials*. Springer, 2000.

[31] S. Babar and J. H. Weaver, "Optical constants of Cu, Ag, and Au revisited," *Appl. Opt.*, vol. 54, no. 3, pp. 477–481, Jan 2015.

[32] A. D. Rakić, A. B. Djurišić, J. M. Elazar, and M. L. Majewski, "Optical properties of metallic films for vertical-cavity optoelectronic devices," *Appl. Opt.*, vol. 37, no. 22, pp. 5271–5283, Aug 1998.

[33] P. G. Etchegoin, E. C. Le Ru, and M. Meyer, "An analytic model for the optical properties of gold," *The Journal of Chemical Physics*, vol. 125, no. 16, p. 164705, 2006.

[34] A. Vial, T. Laroche, M. Dridi, and L. L. Cunff, "A new model of dispersion for metals leading to a more accurate modeling of plasmonic structures using the FDTD method," *Applied Physics A*, vol. 103, pp. 849–853, Jun 2011.

[35] R. Brendel and D. Bormann, "An infrared dielectric function model for amorphous solids," *Journal of Applied Physics*, vol. 71, no. 1, pp. 1–6, 1992.

[36] J. Orosco and C. F. M. Coimbra, "On a causal dispersion model for the optical properties of metals," *Appl. Opt.*, vol. 57, no. 19, pp. 5333–5347, Jul 2018.

[37] R. E. Collin, *Field Theory of Guided Waves*. Wiley-IEEE Press, 1990.

[38] J. N. Gollub, D. R. Smith, D. C. Vier, T. Perram, and J. J. Mock, "Experimental characterization of magnetic surface plasmons on metamaterials with negative permeability," *Phys. Rev. B*, vol. 71, p. 195402, May 2005.

[39] M. G. Blaber, M. D. Arnold, and M. J. Ford, "Search for the ideal plasmonic nanoshell: The effects of surface scattering and alternatives to gold and silver," *The Journal of Physical Chemistry C*, vol. 113, no. 8, pp. 3041–3045, 2009.

[40] H. S. Tetikol, "Dispersion engineering of surface plasmon polaritons," Ph.D. dissertation, Koç University, 2020.

[41] A. Archambault, T. V. Teperik, F. Marquier, and J. J. Greffet, "Surface plasmon Fourier optics," *Phys. Rev. B*, vol. 79, p. 195414, May 2009.

[42] R. W. Alexander, G. S. Kovener, and R. J. Bell, "Dispersion curves for surface electromagnetic waves with damping," *Phys. Rev. Lett.*, vol. 32, pp. 154–157, Jan 1974.

[43] J. A. Dionne, L. A. Sweatlock, H. A. Atwater, and A. Polman, "Planar metal plasmon waveguides: frequency-dependent dispersion, propagation, localization, and loss beyond the free electron model," *Phys. Rev. B*, vol. 72, p. 075405, Aug 2005.

[44] ——, "Plasmon slot waveguides: Towards chip-scale propagation with subwavelength-scale localization," *Phys. Rev. B*, vol. 73, p. 035407, Jan 2006.

[45] A. Chandran, E. S. Barnard, J. S. White, and M. L. Brongersma, "Metal-dielectric-metal surface plasmon-polariton resonators," *Phys. Rev. B*, vol. 85, p. 085416, Feb 2012.

[46] R. Zia, J. A. Schuller, A. Chandran, and M. L. Brongersma, "Plasmonics: the next chip-scale technology," *Materials Today*, vol. 9, no. 7, pp. 20–27, 2006.

[47] S. Kocabaş, G. Veronis, D. A. B. Miller, and S. Fan, "Modal analysis and coupling in metal-insulator-metal waveguides," *Phys. Rev. B*, vol. 79, p. 035120, Jan 2009.

[48] A. P. Vinogradov, A. V. Dorofeenko, A. A. Pukhov, and A. A. Lisyansky, "Exciting surface plasmon polaritons in the Kretschmann configuration by a light beam," *Phys. Rev. B*, vol. 97, p. 235407, Jun 2018.

[49] G. Rosenblatt, B. Simkhovich, G. Bartal, and M. Orenstein, "Nonmodal plasmonics: Controlling the forced optical response of nanostructures," *Phys. Rev. X*, vol. 10, p. 011071, Mar 2020.

[50] M. Kaliteevski, I. Iorsh, S. Brand, R. A. Abram, J. M. Chamberlain, A. V. Kavokin, and I. A. Shelykh, "Tamm plasmon-polaritons: Possible electromagnetic states at the interface of a metal and a dielectric Bragg mirror," *Phys. Rev. B*, vol. 76, p. 165415, Oct 2007.

[51] M. E. Sasin, R. P. Seisyan, M. A. Kalitteevski, S. Brand, R. A. Abram, J. M. Chamberlain, A. Y. Egorov, A. P. Vasil'ev, V. S. Mikhrin, and A. V. Kavokin, "Tamm plasmon polaritons: Slow and spatially compact light," *Applied Physics Letters*, vol. 92, no. 25, p. 251112, 2008.

[52] N. J. Halas, S. Lal, W.-S. Chang, S. Link, and P. Nordlander, "Plasmons in strongly coupled metallic nanostructures," *Chemical Reviews*, vol. 111, no. 6, pp. 3913–3961, 2011, pMID: 21542636.

[53] J. D. Jackson, *Classical Electrodynamics*, 3rd ed. New York, NY: Wiley, 1998.

[54] W. T. Doyle, "Optical properties of a suspension of metal spheres," *Phys. Rev. B*, vol. 39, pp. 9852–9858, May 1989.

[55] A. A. Govyadinov and V. A. Markel, "From slow to superluminal propagation: Dispersive properties of surface plasmon polaritons in linear chains of metallic nanospheroids," *Phys. Rev. B*, vol. 78, p. 035403, Jul 2008.

[56] W. H. Weber and G. W. Ford, "Propagation of optical excitations by dipolar interactions in metal nanoparticle chains," *Phys. Rev. B*, vol. 70, p. 125429, Sep 2004.

[57] L. Novotny, B. Hecht, and D. W. Pohl, "Interference of locally excited surface plasmons," *Journal of Applied Physics*, vol. 81, no. 4, pp. 1798–1806, 1997.

[58] M. L. Brongersma, J. W. Hartman, and H. A. Atwater, "Electromagnetic energy transfer and switching in nanoparticle chain arrays below the diffraction limit," *Phys. Rev. B*, vol. 62, pp. R16 356–R16 359, Dec 2000.

[59] A. Koenderink and A. Polman, "Complex response and polariton-like dispersion splitting in periodic metal nanoparticle chains," *Phys. Rev. B*, vol. 74, p. 033402, Jul 2006.

[60] B. T. Draine and P. J. Flatau, "Discrete-dipole approximation for scattering calculations," *J. Opt. Soc. Am. A*, vol. 11, no. 4, pp. 1491–1499, Apr 1994.

[61] S. Steshenko and F. Capolino, "Single dipole approximation for modeling collections of nanoscatterers," in *Theory and Phenomena of Metamaterials*, ser. 5, F. Capolino, Ed. Boca Raton, FL: CRC Press, 2009, vol. 4, ch. 8, pp. 8.1–8.17.

[62] S. Y. Park and D. Stroud, "Surface-plasmon dispersion relations in chains of metallic nanoparticles: An exact quasistatic calculation," *Phys. Rev. B*, vol. 69, p. 125418, Mar 2004.

[63] A. Alù and N. Engheta, "Theory of linear chains of metamaterial/plasmonic particles as subdiffraction optical nanotransmission lines," *Phys. Rev. B*, vol. 74, p. 205436, Nov 2006. [Online]. Available: https://link.aps.org/doi/10.1103/PhysRevB.74.205436

[64] N. Kinsey, M. Ferrera, V. M. Shalaev, and A. Boltasseva, "Examining nanophotonics for integrated hybrid systems: a review of plasmonic inter-

connects and modulators using traditional and alternative materials," *J. Opt. Soc. Am. B*, vol. 32, no. 1, pp. 121–142, Jan 2015.

[65] V. B. Zon, "Reflection, refraction, and transformation into photons of surface plasmons on a metal wedge," *J. Opt. Soc. Am. B*, vol. 24, no. 8, pp. 1960–1967, Aug 2007.

[66] M. Yan and M. Qiu, "Guided plasmon polariton at 2D metal corners," *J. Opt. Soc. Am. B*, vol. 24, no. 9, pp. 2333–2342, Sep 2007.

[67] C. Bouwkamp, "A note on singularities occurring at sharp edges in electromagnetic diffraction theory," *Physica*, vol. 12, no. 7, pp. 467–474, 1946.

[68] J. Meixner, "The behavior of electromagnetic fields at edges," *IEEE Transactions on Antennas and Propagation*, vol. 20, no. 4, pp. 442–446, 1972.

[69] I. A. Kotelnikov, V. V. Gerasimov, and B. A. Knyazev, "Diffraction of a surface wave on a conducting rectangular wedge," *Phys. Rev. A*, vol. 87, p. 023828, Feb 2013.

[70] N. K. Uzunoglu, C. N. Capsalis, and I. Tigelis, "Scattering from an abruptly terminated single-mode-fiber waveguide," *J. Opt. Soc. Am. A*, vol. 4, no. 11, pp. 2150–2157, Nov 1987.

[71] I. Tigelis, N. Uzunoglu, and C. Capsalis, "Diffraction from an abruptly terminated single mode fiber waveguide," *Journal of Electromagnetic Waves and Applications*, vol. 5, no. 12, pp. 1393–1418, 1991.

[72] H. Liu and P. Lalanne, "Microscopic theory of the extraordinary optical transmission," *Nature*, vol. 452, no. 7188, pp. 728–731, Apr 2008.

[73] P. Lalanne, J. P. Hugonin, and J. C. Rodier, "Theory of surface plasmon generation at nanoslit apertures," *Phys. Rev. Lett.*, vol. 95, p. 263902, Dec 2005.

[74] ——, "Approximate model for surface-plasmon generation at slit apertures," *J. Opt. Soc. Am. A*, vol. 23, no. 7, pp. 1608–1615, Jul 2006.

[75] I. Chremmos, "Magnetic field integral equation analysis of surface plasmon scattering by rectangular dielectric channel discontinuities," *J. Opt. Soc. Am. A*, vol. 27, no. 1, pp. 85–94, Jan 2010.

[76] E. Moreno, D. Erni, C. Hafner, and R. Vahldieck, "Multiple multipole method with automatic multipole setting applied to the simulation of surface plasmons in metallic nanostructures," *J. Opt. Soc. Am. A*, vol. 19, no. 1, pp. 101–111, Jan 2002.

[77] G. Brucoli and L. Martín-Moreno, "Comparative study of surface plasmon scattering by shallow ridges and grooves," *Phys. Rev. B*, vol. 83, p. 045422, Jan 2011.

[78] ——, "Effect of defect depth on surface plasmon scattering by subwavelength surface defects," *Phys. Rev. B*, vol. 83, p. 075433, Feb 2011.

[79] Lumerical, Inc., "Lumerical FDTD Solutions (2020a)." [Online]. Available: https://www.lumerical.com/

[80] K. Yee, "Numerical solution of initial boundary value problems involving Maxwell's equations in isotropic media," *IEEE Transactions on Antennas and Propagation*, vol. 14, no. 3, pp. 302–307, 1966.

[81] A. Taflove and S. C. Hagness, *Computational Electrodynamics: the Finite-Difference Time-Domain Method*, 3rd ed. Norwood: Artech House, 2005.

[82] L. Chrostowski and M. Hochberg, *Silicon Photonics Design: From Devices to Systems*. Cambridge University Press, 2015.

[83] Z. Zhu and T. G. Brown, "Full-vectorial finite-difference analysis of microstructured optical fibers," *Opt. Express*, vol. 10, no. 17, pp. 853–864, Aug 2002.

[84] Y. Hua and T. Sarkar, "Generalized pencil-of-function method for extracting poles of an EM system from its transient response," *IEEE Transactions on Antennas and Propagation*, vol. 37, no. 2, pp. 229–234, 1989.

[85] A. W. Snyder and J. Love, *Optical Waveguide Theory*. Springer, 1983.

[86] P. Lalanne and J. P. Hugonin, "Interaction between optical nano-objects at metallo-dielectric interfaces," *Nature Physics*, vol. 2, no. 8, pp. 551–556, Aug 2006.

[87] W. Dai and C. M. Soukoulis, "Theoretical analysis of the surface wave along a metal-dielectric interface," *Phys. Rev. B*, vol. 80, p. 155407, Oct 2009.

[88] A. Y. Nikitin, S. G. Rodrigo, F. J. García-Vidal, and L. Martín-Moreno, "In the diffraction shadow: Norton waves versus surface plasmon polaritons in the optical region," *New Journal of Physics*, vol. 11, no. 12, p. 123020, dec 2009.

[89] R. D. Nevels and K. A. Michalski, "On the behavior of surface plasmons at a metallo-dielectric interface," *J. Lightwave Technol.*, vol. 32, no. 19, pp. 3299–3305, Oct 2014.

[90] R. Zia, A. Chandran, and M. L. Brongersma, "Dielectric waveguide model for guided surface polaritons," *Opt. Lett.*, vol. 30, no. 12, pp. 1473–1475, Jun 2005.

[91] G. B. Hocker and W. K. Burns, "Mode dispersion in diffused channel waveguides by the effective index method," *Appl. Opt.*, vol. 16, no. 1, pp. 113–118, Jan 1977.

[92] T. Koschny, M. Kafesaki, E. N. Economou, and C. M. Soukoulis, "Effective medium theory of left-handed materials," *Phys. Rev. Lett.*, vol. 93, p. 107402, Sep 2004.

[93] G. Shvets, "Photonic approach to making a material with a negative index of refraction," *Phys. Rev. B*, vol. 67, p. 035109, Jan 2003.

[94] G. I. Stegeman, N. E. Glass, A. A. Maradudin, T. P. Shen, and R. F. Wallis, "Fresnel relations for surface polaritons at interfaces," *Opt. Lett.*, vol. 8, no. 12, pp. 626–628, Dec 1983.

[95] R. Gordon, "Vectorial method for calculating the Fresnel reflection of surface plasmon polaritons," *Phys. Rev. B*, vol. 74, p. 153417, Oct 2006.

[96] ——, "Light in a subwavelength slit in a metal: Propagation and reflection," *Phys. Rev. B*, vol. 73, p. 153405, Apr 2006.

[97] G. S. Unal and M. I. Aksun, "Bridging the gap between RF and optical patch antenna analysis via the cavity model," *Scientific Reports*, vol. 5, no. 1, p. 15941, 2015.

[98] A. V. Oppenheim and A. S. Willsky, *Signals and Systems*, 2nd ed. New Jersey: Prentice Hall,, 1997.

[99] A. Chandran, "Metal insulator multi-layer surface plasmon devices," Ph.D. dissertation, Stanford University, 2014.

[100] Z. Sharifi and R. Gordon, "Large plasmonic resonance shifts from metal loss in slits," *Plasmonics*, Aug 2021.

[101] S. V. Yuferev and N. Ida, *Surface Impedance Boundary Conditions: A Comprehensive Approach.* Taylor & Francis, 2010.

[102] R. F. Wallis and A. A. Maradudin, "Surface polariton reflection and radiation at end faces," *Appl. Phys. Lett.*, vol. 42, no. 6, pp. 863–871, Feb 1983.

[103] L. A. Mayoral-Astorga, J. A. Gaspar-Armenta, and F. Ramos-Mendieta, "Surface plasmon transmission through discontinuous conducting surfaces: Plas-

mon amplitude modulation by grazing scattered fields," *AIP Advances*, vol. 6, no. 4, p. 045316, 2016.

[104] A. Q. Jian and X. M. Zhang, "Resonant optical tunneling effect: Recent progress in modeling and applications," *IEEE Journal of Selected Topics in Quantum Electronics*, vol. 19, no. 3, pp. 9 000 310–9 000 310, 2013.

[105] I. Avrutsky, Y. Zhao, and V. Kochergin, "Surface-plasmon-assisted resonant tunneling of light through a periodically corrugated thin metal film," *Opt. Lett.*, vol. 25, no. 9, pp. 595–597, May 2000.

[106] W. C. Liu and D. P. Tsai, "Optical tunneling effect of surface plasmon polaritons and localized surface plasmon resonance," *Phys. Rev. B*, vol. 65, p. 155423, Apr 2002.

[107] S. Sidorenko and O. J. F. Martin, "Resonant tunneling of surface plasmon-polaritons," *Opt. Express*, vol. 15, no. 10, pp. 6380–6388, May 2007.

[108] J. Park, H. Kim, I. M. Lee, S. Kim, J. Jung, and B. Lee, "Resonant tunneling of surface plasmon polariton in the plasmonic nano-cavity," *Opt. Express*, vol. 16, no. 21, pp. 16 903–16 915, Oct 2008.

[109] Y. C. Lan, C. J. Chang, and P.-H. Lee, "Resonant tunneling effects on cavity-embedded metal film caused by surface-plasmon excitation," *Opt. Lett.*, vol. 34, no. 1, pp. 25–27, Jan 2009.

[110] R. Esteban, A. Z. P. Zhang, P. Nordlander, F. J. García-Vidal, A. G. Borisov, and J. Aizpurua, "A classical treatment of optical tunneling in plasmonic gaps: extending the quantum corrected model to practical situations," *Faraday Discuss.*, vol. 178, pp. 151–183, 2015.

[111] V. V. Gerasimov, B. A. Knyazev, A. K. Nikitin, and G. N. Zhizhin, "Experimental investigations into capability of terahertz surface plasmons to bridge

macroscopic air gaps," *Opt. Express*, vol. 23, no. 26, pp. 33 448–33 459, Dec 2015.

[112] S. I. Bozhevolnyi, "Effective-index modeling of channel plasmon polaritons," *Opt. Express*, vol. 14, no. 20, pp. 9467–9476, Oct 2006.

[113] L. D. Landau and E. M. Lifshitz, *Electrodynamics of Continuous Media*. Pergamon Press, 1960.

[114] M. Kuttge, F. J. G. de Abajo, and A. Polman, "How grooves reflect and confine surface plasmon polaritons," *Opt. Express*, vol. 17, no. 12, pp. 10 385–10 392, Jun 2009.

[115] J. S. Q. Liu, J. S. White, S. Fan, and M. L. Brongersma, "Side-coupled cavity model for surface plasmon-polariton transmission across a groove," *Opt. Express*, vol. 17, no. 20, pp. 17 837–17 848, Sep 2009.

[116] H. Jamid and S. Al-Bader, "Reflection and transmission of surface plasmon mode at a step discontinuity," *IEEE Photonics Technology Letters*, vol. 9, no. 2, pp. 220–222, 1997.

[117] ——, "Diffraction of surface plasmon-polaritons in an abruptly terminated dielectric-metal interface," *IEEE Photonics Technology Letters*, vol. 7, no. 3, pp. 321–323, 1995.

[118] B. Puygranier, P. Dawson, Y. Lacroute, and J.-P. Goudonnet, "Surface plasmon polariton propagation across a gentle silver step," *Surface Science*, vol. 490, no. 1, pp. 85–98, 2001.

[119] N. Yamamoto and T. Suzuki, "Conversion of surface plasmon polaritons to light by a surface step," *Applied Physics Letters*, vol. 93, no. 9, p. 093114, 2008.

[120] B. Wang and P. Lalanne, "Surface plasmon polaritons locally excited on the ridges of metallic gratings," *J. Opt. Soc. Am. A*, vol. 27, no. 6, pp. 1432–1441, Jun 2010.

[121] S. Zhang, H. Liu, and G. Mu, "Electromagnetic enhancement by a periodic array of nanogrooves in a metallic substrate," *J. Opt. Soc. Am. A*, vol. 28, no. 5, pp. 879–886, May 2011.

[122] A. Dhawan, M. Canva, and T. Vo-Dinh, "Narrow groove plasmonic nanogratings for surface plasmon resonance sensing," *Opt. Express*, vol. 19, no. 2, pp. 787–813, Jan 2011.

[123] K. Ozawa and N. Yamamoto, "Ridge reflection of surface plasmon-polaritons in a one-dimensional plasmonic cavity," *Phys. Rev. B*, vol. 100, p. 075406, Aug 2019.

[124] J. Ritter and F. Amdt, "Efficient FDTD/matrix-pencil method for the full-wave scattering parameter analysis of waveguiding structures," *IEEE Transactions on Microwave Theory and Techniques*, vol. 44, no. 12, pp. 2450–2456, 1996.

[125] A. Bhattacharyya, "Effects of ground plane and dielectric truncations on the efficiency of a printed structure," *IEEE Transactions on Antennas and Propagation*, vol. 39, no. 3, pp. 303–308, 1991.

[126] V. Volski and G. Vandenbosch, "Diffraction of a surface wave at the truncation of a dielectric structure," *IEEE Transactions on Antennas and Propagation*, vol. 50, no. 12, pp. 1779–1785, 2002.

[127] D. A. Hill and J. R. Wait, "Excitation of the Zenneck surface wave by a vertical aperture," *Radio Science*, vol. 13, no. 6, pp. 969–977, 1978.

[128] J. B. Keller, "Geometrical theory of diffraction," *J. Opt. Soc. Am.*, vol. 52, no. 2, pp. 116–130, Feb 1962.

[129] B. Gustavsen and A. Semlyen, "Rational approximation of frequency domain responses by vector fitting," *IEEE Transactions on Power Delivery*, vol. 14, no. 3, pp. 1052–1061, 1999.

[130] F. Kahnert, "Numerical methods in electromagnetic scattering theory," *Journal of Quantitative Spectroscopy and Radiative Transfer*, vol. 79-80, pp. 775–824, 2003.

[131] C. Balanis, *Advanced Engineering Electromagnetics*. Wiley, 2012.

[132] J. B. Keller and F. C. Karal, "Surface wave excitation and propagation," *Journal of Applied Physics*, vol. 31, no. 6, pp. 1039–1046, 1960.

[133] M. Paulus, P. Gay-Balmaz, and O. J. F. Martin, "Accurate and efficient computation of the Green's tensor for stratified media," *Phys. Rev. E*, vol. 62, pp. 5797–5807, Oct 2000.

[134] M. Aksun, "A robust approach for the derivation of closed-form Green's functions," *IEEE Transactions on Microwave Theory and Techniques*, vol. 44, no. 5, pp. 651–658, 1996.

[135] G. Waldschmidt and A. Taflove, "The determination of the effective radius of a filamentary source in the FDTD mesh," *IEEE Microwave and Guided Wave Letters*, vol. 10, no. 6, pp. 217–219, 2000.